AN EXPLORATION OF DEFECT-BASED SINGLE PHOTON SOURCES: ZINC OXIDE AND HEXAGONAL BORON NITRIDE

A Dissertation

Presented to the Faculty of the Graduate School

of Cornell University

In Partial Fulfillment of the Requirements for the Degree of

Doctor of Philosophy

by

Nicholas Ryan Jungwirth

December 2018

AN EXPLORATION OF DEFECT-BASED SINGLE PHOTON SOURCES: ZINC OXIDE AND HEXAGONAL BORON NITRIDE

Nicholas Ryan Jungwirth, Ph.D.

Cornell University 2018

Isolated point defects in wide bandgap semiconductors are single photon sources with applications in quantum optics, precision sensing, and quantum information processing technologies. Although the nitrogen-vacancy center in diamond has historically garnered the most attention, efforts to discover novel single photon sources have uncovered candidates in SiC, GaN, WSe_2, WS_2, ZnO, and hexagonal boron nitride (h-BN). In this thesis we focus our attention on single photon emission from defect in ZnO and h-BN.

In the case of ZnO, the single-photon emission is in the range of 560 – 720 nm and typically exhibits two broad spectral peaks separated by ~150 meV. We observe discrete jumps in the fluorescence intensity between a bright state and a dark state and identify two varieties of dark state. Polarization measurements reveal the presence of a single absorption and emission dipole aligned parallel to one another. Point group theory indicates that the optical transitions investigated involve orbital singlets.

In the case of h-BN, the single-photon emission typically includes a sharp zero-phonon line (ZPL) with a phonon sideband red-shifted by ~165 meV. The ZPL energy varies strongly from defect-to-defect and is distributed

across an energy range in excess of 500 meV. We study the temperature-dependent linewidth, spectral energy shift, and intensity for two different ZPLs centered at 575 nm and 682 nm. These results are well described by a lattice vibration model that considers piezoelectric coupling to in-plane acoustic phonons. Lastly, we investigate the polarization selection rules and compare our findings with the predictions of the Huang-Rhys model. Our survey reveals that a two-level Huang-Rhys model succeeds at describing excitations mediated by the creation of one in-plane optical phonon but fails at describing excitations that require the creation of multiple phonons. We propose that direct excitations requiring the creation of multiple phonons are inefficient due to the low Huang-Rhys factors in h-BN and that these ZPLs are instead excited indirectly via an intermediate electronic state. This hypothesis is corroborated by polarization measurements of an individual ZPL excited with two distinct wavelengths that indicate a single ZPL may be excited by multiple mechanisms.

BIOGRAPHICAL SKETCH

My friend once asked me, “If you were to write an autobiography, what would its first chapter be titled?” “Vanity”, I promptly responded. The type of person who writes an autobiography, I reasoned, must either be very full of themselves or have accomplished something meaningful. My flippant quip is now met with the reality of writing the biographical sketch you see here, a miniature autobiography of sorts. While the brevity of this sketch does not justify a chapter title, the thesis that follows must constitute a meaningful contribution to physics. But first, let me tell you a bit about myself.

I was born on November 2, 1988 in Phoenix, Arizona to Bryan and Amy Jungwirth. My only sibling, Alexandra Jungwirth, was born on July 15, 1991. As a youth, I primarily enjoyed video games and sports, with baseball being my forte. Though I always excelled in mathematics, I never took my education too seriously until high school, when I joined the International Baccalaureate Program at North Canyon High School. Following my parents’ advice, I initially avoided physics on the grounds that “physics is tough.” It wasn’t until my junior year that my chemistry teacher, Barbara Rosenberg, noticed my penchant for science and encouraged me to enroll in physics. It is interesting to consider how strongly our teachers can influence the people we become.

After graduating High School, I accepted the President’s Scholarship at Arizona State University (ASU). ASU had the advantage of being close to all of my friends, while also having the Barrett Honors College and a strong

engineering program. After my first year, I realized I enjoyed my physics class far more than my introductory engineering course. That summer I joined the research group of my physics professor, Jeff Drucker, and officially declared myself a physics major. Jeff prepared me for graduate level research, and I thoroughly enjoyed the three years I spent in his lab. In 2011, I graduated Summa Cum Laude from ASU with B.S. degrees in Physics and Mathematics.

Having been accepted into several graduate schools, I ultimately decided to accept a graduate fellowship at Cornell University in Ithaca, New York. I was simultaneously excited to start a new research project and unsure what I wanted that project to be. I met with professors in physics, mathematics, engineering, economics, and even biology to find the ideal project. In the end, I decided to work with a new professor in Applied Physics, Greg Fuchs. Greg had many ideas and was eager to get the experimental ball rolling. With his help, I designed and built the confocal microscope used in this thesis. There are many anecdotes that could be included here, but suffice it to say that it has been an amazing seven years. My next adventure will be as a post doc at NIST in Boulder, Colorado.

For my parents: Amy and Bryan.

ACKNOWLEDGMENTS

First, I would like to give a special thanks to my special committee: Greg Fuchs, Kyle Shen, and Erich Mueller. In particular, I wish to acknowledge Greg for his unwavering support and enthusiasm throughout my PhD. Greg has always been available to offer his expertise and feedback, while also allowing me the freedom to pursue my own research interests. I am truly indebted to him for everything he has done for me.

I also wish to thank my lab mates and friends at Cornell: Brian Calderon, Evan MacQuarrie, Jason Bartell, Tanay Gosavi, Hung-Shen Chang, Jack Jiang, Yun-Yi Pai, Nikhil Mathur, Nikola Protic, Isaiah Gray, Albert Park, Krishnan Chander, Joel Weiss, Tomas Rojo, Kevin O'Keefe, and Ismail El Baggari. To Brian: Thanks for your friendship and initiating our study of hBN. To Evan and Jason: It was great building up the lab with you. Good luck going forward. To Hung, Jack, Pai, Nikola, and Nikhil: Thanks for your sincere interest in the single-defect project. Working alongside all of you was a blast.

I would like to thank my parents for supporting me throughout my PhD. Thank you for all your financial and emotional assistance. I couldn't have done it without you. As my mom would jest, "*We* did it."

Finally, I would like to give a huge thanks to all my Ithaca friends: Alison McCann, Alex Stick, Christine McMeekin, Micah Beam-Miller, Alison Byers, Toby Girard, Bob Pettit, Alex Adams, Tony Petri, Jeremy Veverka, Rich Bernstein, Rob Blackmore, Jessica Shipley, and Susan Barber. Its almost impossible for me to think of Ithaca without thinking of you all.

TABLE OF CONTENTS

LIST OF FIGURES

LIST OF TABLES

CHAPTER 1

INTRODUCTION

A diamond is just a chunk of coal that did really well under pressure.

- Henry Kissinger

1.1 Point Defects and the Ensemble Average

The bulk properties of an ideal crystal are determined by its constituent atoms and its lattice configuration. Consider, for example, the sixth element on the periodic table: carbon. When carbon's orbitals sp^2 hybridize graphite may be formed, an opaque semimetal. However, if the same carbon atoms sp^3 hybridize then diamond may be formed. Unlike graphite, diamond is an electrical insulator and is transparent at optical wavelengths. Incidentally, seemingly small changes in crystal configuration can produce vast differences in bulk properties.

Real crystals differ from their ideal analogs due to the presence of imperfections, or defects. These defects include vacancies (empty lattice sites), substitutions (a foreign atom at a lattice site), interstitials (atoms not localized at a lattice site), antisites (an atom at the lattice site of a different element) and defect complexes (combinations thereof in close proximity to one another). Returning to our diamond example, more than 500 defect types exist and each may introduce unique attributes to the host material [5–7]. For

instance, diamonds containing nitrogen impurities may appear yellow or green, depending on concentration, and also possess slight birefringence and a reduced thermal conductivity. Alternatively, diamonds containing boron may appear blue and exhibit p-type conductivity. In practice the optical, electrical, thermal, and magnetic characteristics of a crystal are largely determined by the synergistic effect of its defects. The corollary to this observation is that a crystal's properties may be tuned for particular applications by intentionally introducing or removing defects via electron irradiation, ion implantation, doping, annealing treatments, and combinations thereof. A thorough knowledge of defects is therefore vital for understanding and tweaking the properties of a crystal.

Experimental investigations of crystalline defects have historically been "ensemble" in nature, meaning many defects are simultaneously probed and the cumulative response is measured. For example, consider a simple photoluminescence experiment where a diamond is illuminated and the emission spectrum of the fluorescence is measured [8]. In this scenario the recorded spectrum is the weighted sum, or ensemble average, of the individual emission spectra from each defect in the sample. To infer the emission spectrum of a particular defect species, one often attempts to correlate changes in the measured emission spectrum with changes in sample preparation that are known to introduce or remove defects of that type. While experiments of this sort are essential for understanding defects, they lack the ability to resolve defect-to-defect variation and single-defect dynamics. This

situation is illustrated in Figure 1.1, where the spatial and temporal variations of a particular defect type are “washed out” by the ensemble average. This issue is exacerbated in experiments that investigate many distinct defect types simultaneously, making it difficult to definitively associate a particular bulk property with a particular defect species.

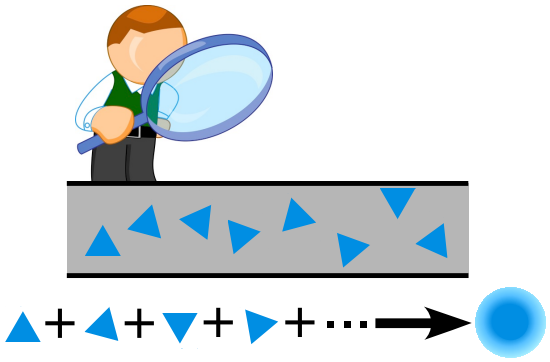

Figure 1.1: Defect-to-defect variations and single-defect dynamics are hidden in an ensemble measurement.

1.2 Beyond the Ensemble Average

The limitations of the ensemble average can be overcome by borrowing techniques from the field of single-molecule microscopy [9]. A typical approach utilizes a confocal microscope [10] to tightly focus a laser onto the crystal of interest. If the defect density in the sample is such that only one optically active defect, or color center, is contained in the confocal volume of the microscope, then a single defect may be investigated. In this case the observed properties and temporal dynamics may be unambiguously assigned to the defect being studied. Because the data is straightforward to interpret in

this sense, single-defect experiments may also be readily compared with theoretical predictions.

Interestingly, the single-molecule approach to defect studies has paved the way towards applications far more exciting than tuning the opacity or hue of a diamond. The nitrogen-vacancy (NV) center in diamond, a defect complex composed of a substitutional nitrogen atom adjacent to a lattice vacancy, was the first defect species to be optically isolated and to exhibit single-photon emission [11,12]. The NV center is a spin-1 system whose spin state may be initialized, manipulated, and measured at room temperature, making it a promising qubit candidate for quantum information processing applications [13,14]. The NV center has also proven to be a precision magnetometer, [15,16], thermometer [17,18], and electrometer [19]. These applications only scratch the surface of the range of applications of NV centers [13].

1.3 Beyond the NV Center

The NV center was first optically isolated in 1997 by Gruber *et* al [11] and single photon emission was NV centers was first observed in 2000 by Kurtsiefer *et al* [12]. A decade later, in 2010, Weber *et al* [20] noted that while the NV center had proven to be very robust, “no systematic effort has been made to identify other deep centers that might behave similarly.” The benefits of exploring alternative defect systems are twofold. Firstly, unexplored single-

defect systems may exhibit properties that are complementary to NV centers, thus opening up new single-defect applications. Secondly, as a practical concern, diamond is not a technologically mature host material, which limits the scalability and scope of diamond-based devices. Discovering NV-like defects in a more engineerable and cost-effective material may permit certain applications to be realized that would be unfeasible otherwise.

This thesis constitutes just one of several systematic efforts that have subsequently emerged to discover defect-based single photon sources beyond the NV center. At the time of writing (2018), new defects have been optically isolated in diamond [21–23], SiC [24–29], ZnO [1,2,30–33], GaN [34], WSe_2 [35–37], WS_2 [38], and hexagonal boron nitride (h-BN) [3,4,39–59]. ZnO and h-BN are the focus of this work, which is organized as follows: In Chapter 2, the two-photon correlation is introduced and the experimental subtleties of its interpretation are discussed. Chapter 3 describes microscope retardance and outlines our approach to compensate for these effects in order to perform polarization measurements. In Chapter 4, we investigate defect-to-defect variations and single-defect photodynamics of isolated point defects in ZnO. In Chapter 5, we apply polarization spectroscopy to ZnO defects and find that the investigated electronic transitions are between orbital singlets. In Chapter 6, we investigate the homogenous ZPL linewidth broadening of single defects in h-BN. We develop a lattice vibration model that suggests the broadening we observe is governed by in-plane acoustic phonons. Finally, in Chapter 7 we investigate the relationship between the absorption and

emission dipole for individual h-BN defects and compare our findings with the predictions of the Huang-Rhys model.

CHAPTER 2

SINGLE PHOTON EMISSION:

THE TWO-PHOTON CORRELATION FUNCTION

2.1 Introduction

The standard technique for determining the nature of an optical field is by measuring time-intensity correlations between a series of photodetectors [60]. In the simplest scenario we have a single detector recording the optical intensity as a function of time. This first order correlation function, $g^{(1)}(\tau)$, is adequate for determining the trajectory of the fluorescence intensity, or brightness, of a light source, but to date is inadequate for distinguishing a quantum light source from a classical or semi-classical one. Incidentally, higher order correlations must be measured to verify the quantum nature of a field/source.

Glauber [60] recognized in 1963 that a quantum field is distinguished from a classical field by an anticorrelation, or antibunching, in the second-order correlation function, $g^{(2)}(\tau)$. An anticorrelation in $g^{(2)}(\tau)$ occurs whenever the variance of the photon number $(\Delta N)^2$ is less than the average photon number $\langle N \rangle$. This inequality clearly holds for a field containing a single photon, whereby $(\Delta N)^2 = 0$ and $\langle N \rangle = 1$. In 1974 Stoler [61] suggested an experimental approach to observing antibunching and in 1976 Carmichael and Walls predicted that the fluorescence from a driven two-level atom would

exhibit antibunching. Finally, in 1977, Kimble *et al* [62] observed antibunching for the first time from the resonant excitation of sodium atoms.

In the 40 years since the first observation of antibunching, the two-photon correlation function has become an integral aspect of any investigation of single photon emitters. As such, there is an extensive literature outlining its rigorous mathematical definition and demonstrating its experimental utility [9,60,63–66]. In this Chapter we construct $g^2(\tau)$ using an alternative method than is commonly used. Our approach is intuitive and is readily adapted to accommodate the realities of the laboratory.

2.2 Mathematical Construction

Consider a light source S and a photodetector D. We assume momentarily that D is ideal in the sense that it detects every photon from S and precisely records each photon's arrival time τ_i. In this sense we are not yet distinguishing photon emission events from photon detection events. Note that we have made no assumptions about S, meaning the τ_i may be degenerate. We define

$$W = \{\tau_i\}_{1 \le i \le N}, \tag{2.1}$$

where N is the total number of photons detected. From W we may calculate the instantaneous fluorescence intensity, $r(t)$, as well as the time-averaged fluorescence intensity

$$R = \langle r(t) \rangle = \frac{N}{T}, \tag{2.2}$$

where $T = \tau_N - \tau_1$ is the total collection time. Moreover, we may construct the set of delay times between distinct photons

$$\Delta = \{\tau_i - \tau_j : i \neq j\}. \tag{2.3}$$

We define $g^{(2)}(\tau)$ as the normalized histogram of the elements of Δ. It is typical to normalize $g^{(2)}(\tau)$ such that $g^{(2)}(\tau) = 1$ for uncorrelated light. This convention is convenient because it allows the photon statistics of a light source to be directly compared with the Poisson distribution. For example, if a photon is detected at time $t = 0$ then the instantaneous "count rate" at time $t = \tau$ is simply $r(\tau) = Rg^{(2)}(\tau)$. For large τ correlations vanish and $g^{(2)}(\tau) = 1$. For this reason, any region where $g^{(2)}(\tau) > 1$ is referred to as bunching and any region where $g^{(2)}(\tau) < 1$ is referred to as antibunching. Antibunching has no classical analog and is the smoking gun for quantum light. We discuss antibunching in *Section 2.4* and bunching in *Chapter 4*.

Suppose we construct our histogram of Δ using a bin width of δ. For uncorrelated light, each $\tau_i \in W$ will contribute an average of $N\delta/T$ counts to each histogram bin. Because there are N elements in W, each contributing $N\delta/T$ counts to each histogram bin, the proper normalization factor to obtain $g^{(2)}(\tau)$ is $\gamma = N^2\delta/T$. In the laboratory, the fluorescence intensity R is monitored and the relevant normalization factor is

$$\gamma = TR^2\delta. \tag{2.4}$$

2.3 Measuring $g^{(2)}(\tau)$ Experimentally

In *Chapters 4-7* we present time correlated single photon counting (TCSPC) measurements collected experimentally using a Becker & Hickl TCSPC module (SPC-130). Here we outline this measurement and highlight what distinguishes it from the ideal case considered in *Section 2.1*. Consider a light source S and two single-photon detectors D_1 and D_2. Once D_1 detects a photon it sends an electrical pulse to the TCSPC module that triggers a timer to start. Subsequently, once D_2 detects a photon it sends an electrical pulse to the TCSPC module that triggers the timer to stop. Thus the ith start-stop cycle directly measures the ith delay time τ_i between successive detection events at D_1 and D_2. Note that this measurement requires two detectors because each detector experiences a "dead time" of τ_D~100 ns once it absorbs a photon, making it impossible to probe sub-τ_D correlations with a single detector. The experimentally measured $g_M^{(2)}(\tau)$ is obtained from the histogram of $\{\tau_i\}$. In a typical experiment >50,000 delay times, or photon pairs, are recorded to produce $g_M^{(2)}(\tau)$.

Here we consider how to normalize the experimental histogram of $\{\tau_i\}$ and address how well $g_M^{(2)}(\tau)$ approximates $g^{(2)}(\tau)$. Suppose the average photon count rates at D_1 and D_2 are R_1 and R_2, respectively. Moreover, suppose the total collection time is T and we construct our histogram with a bin width of δ. Over the course of the experiment the timer will be triggered

$R_1 T$ times. In the uncorrelated regime, D_2 will detect $R_2 \delta$ photons per bin on average. Thus the appropriate normalization factor is

$$\Gamma = R_1 R_2 T \delta. \tag{2.5}$$

Note that although the experiment outlined here is quite different than that considered in *Section 2.2,* the normalization factor in Equation 2.5 is almost identical to that in Equation 2.4. For instance, given an identical photon stream W (Equation 2.1), the set Δ in Equation 2.3 has $N(N-1)$ elements whereas the experimentally measured set $\{\tau_i\} \subset \Delta$ has at most $N/2$ elements. In the real experiment delay times are "lost" because the real experiment only measures the delay times between *successive* detection events as opposed to the delay times between *all* detection events. This realization spurs the question: In what sense does the measured $g_M^{(2)}(\tau)$ approximate the true $g^{(2)}(\tau)$?

Suppose a photon is detected at D_1 at time $t = 0$. Then the instantaneous "count rate" at D_2 at time t is given by

$$r_2(t) = R_2 g^{(2)}(t). \tag{2.6}$$

Thus on average each time the TCSPC timer is triggered by a detection event at D_1 there will be $\int_0^\tau R_2 g^{(2)}(t) dt$ detection events at D_2 in the time window $(0, \tau)$. These detection events at D_2 render it impossible to measure delay times in excess of τ for these particular clock cycles. To address the significance of this effect we calculate the fraction of clock cycles, for a particular τ, that are unaffected. From the Poisson distribution the probability

of detecting zero photons at D_2 in the time range $(t, t+dt)$ is given by $\exp\left[-R_2 g^{(2)}(t)dt\right]$. Therefore the probability of detecting zero photons in the time range $(0, \tau)$ is $\lim_{dt\to 0}\prod_{j=0}^{\frac{\tau}{dt}}\exp\left[-R_2 g^{(2)}(jdt)dt\right] = \exp\left[-R_2\int_0^\tau g^{(2)}(t)dt\right]$. This factor represents the fraction of "lost" data at τ is increased:

$$g_M^{(2)}(\tau) = g^{(2)}(\tau)\exp\left[-R_2\int_0^\tau g^{(2)}(t)dt\right] \qquad (2.7)$$

For simplicity let us assume that $g^{(2)}(\tau) = 1$. In this case $g_M^{(2)}(\tau)/g^{(2)}(\tau) = e^{-R_2\tau}$. Evidently as τ or R_2 approaches zero $g_M^{(2)}(\tau)$ is indistinguishable from $g^{(2)}(\tau)$. In Table 2.1 we display $g_M^{(2)}(\tau)/g^{(2)}(\tau)$ for various combinations of τ and R_2 for uncorrelated light. In the experiments of *Chapters 4-7* typical values of these parameters are $1\ kHz < R_2 < 500\ kHz$ and $1\ ns < \tau < 200\ ns$. It is worth noting that for antibunched light this effect is reduced and for bunched light this effect is enhanced. To probe correlations of $\tau > \mu s$, which can be important, one often utilizes alternative approaches which are beyond the scope of this Chapter.

	τ~1 ns	τ~10 ns	τ~100 ns	τ~1 μs	τ~10 μs
R_2~1 kHz	0.999999	0.99999	0.9999	0.999	0.99
R_2~10 kHz	0.99999	0.9999	0.999	0.99	0.905
R_2~100 kHz	0.9999	0.999	0.99	0.905	0.367
R_2~1 MHz	0.999	0.99	0.905	0.367	10^{-5}
R_2~10 MHz	0.99	0.905	0.367	10^{-5}	~0

Table 2.1: Values of $g_M^{(2)}(\tau)/g^{(2)}(\tau)$ for uncorrelated light for various delay times τ and count rates R_2.

2.4 Quantum Emission

Consider a simple two-level model of a single quantum emitter with ground state $|1\rangle$ and excited state $|2\rangle$. We model this system via a rate model:

$$\frac{d}{dt}\begin{pmatrix} P_1 \\ P_2 \end{pmatrix} = \begin{pmatrix} -r_{12} & r_{21} \\ r_{12} & -r_{21} \end{pmatrix}\begin{pmatrix} P_1 \\ P_2 \end{pmatrix}. \tag{2.8}$$

Here r_{ij} is the transition rate from $|i\rangle \rightarrow |j\rangle$ and P_i is the probability of the quantum emitter being in state $|i\rangle$. If we detect a photon at time $t = 0$ at detector D_1 then the wave function necessarily collapses to the ground state: $P_1(t = 0) = 1$ and $P_2(t = 0) = 0$. The time evolution for $t \geq 0$ is given by

$$\begin{pmatrix} P_1(t) \\ P_2(t) \end{pmatrix} = \begin{pmatrix} A \\ B \end{pmatrix} + \begin{pmatrix} B \\ -B \end{pmatrix} e^{-\gamma t}, \tag{2.9}$$

where $A = r_{21}/\gamma$, $B = r_{12}/\gamma$, and $\gamma = r_{12} + r_{21}$. Because the instantaneous count rate is proportional to P_2 we obtain $g^{(2)}(\tau)$ for our hypothetical quantum emitter:

$$g^{(2)}(\tau) = 1 - \exp(-\gamma\tau). \tag{2.10}$$

Note that $1 > g^{(2)}(0) = 0$. This "antibunching dip" has no classical analog and is a unique feature of quantum emission. It results from the fact that once a photon has been emitted the system must be re-excited before another photon may be emitted. In *Section 2.5* we consider the effect of quantum and classical experimental non-idealities that serve to raise $g^{(2)}(0)$ above its theoretical value of zero for a perfect single photon source.

2.5 Interpreting $g^{(2)}(0)$

Consider an experiment probing N independent single-photon sources $\{Q_i\}$ with average fluorescence intensities q_i and a classical uncorrelated light source C with fluorescence intensity c. Note that in practice the source C contains uncorrelated contributions from background fluorescence, room lights, and detector dark counts. Here we calculate the expected value of $g_M^{(2)}(0) = g^{(2)}(0)$ using the start-stop methodology introduced in *Section 2.3*. To do this we first recognize that each timer cycle may be initiated by any of our $N+1$ sources and may likewise be terminated by any of these $N+1$ sources. Consequently we may partition $\{\tau_i\}$ into $M = (N+1)^2$ separate sets and regard $g_M^{(2)}(\tau)$ as the weighted superposition of the histograms from each of these M sets. Here we are only interested in the value $g^{(2)}(0)$ and therefore need only consider histograms that yield $g^{(2)}(0) = 1$. These come in two varieties: when the start or stop was triggered by the classical source and when the start and stop were triggered by distinct quantum sources. The final result is

$$g^{(2)}(0) = \frac{c^2}{R^2} + 2\sum_{i=1}^{N-1}\sum_{j=i+1}^{N}\left[\frac{q_i q_j}{R^2}\right] + 2\sum_{i=1}^{N}\frac{c q_i}{R^2}, \qquad (2.11)$$

where $R = \sum_{i=1}^{N} q_i + c$ is the total fluorescence intensity. We now consider two experimentally relevant examples.

First consider an experiment with two quantum light sources and no classical background. In this case Equation 2.11 becomes:

$$g^{(2)}(0) = \frac{2q_1q_2}{(q_1+q_2)^2}. \quad (2.12)$$

This expression is bounded by $g^{(2)}(0) = 0.5$ in the case that $q_1 = q_2$. This is the origin of the convention in the literature [67] that any experimental measurement of $g_M^{(2)}(0) < 0.5$ corresponds to single photon emission from an individual single photon source. It should be noted, however, from Equation 2.12 that $g_M^{(2)}(0) \leq 0.5$ for any combination of q_1 and q_2. That is, the inequality holds *whenever* two single photon sources are simultaneously probed and care should be executed when interpreting the depth of an antibunching dip.

Secondly consider an experiment with one quantum light source and a classical background. In this case Equation 2.11 becomes:

$$g^{(2)}(0) = \frac{2q_1c}{(q_1+c)^2} + \frac{c^2}{(q_1+c)^2}. \quad (2.13)$$

In contrast to Equation 2.12 this expression is bounded by $g^{(2)}(0) = 1$ in the case that $q_1 \ll c$. In the event that $q_1 = c$ Equation 2.13 yields $g^{(2)}(0) = 0.75$. As expected, the effect of a classical light source on the depth of an antibunching dip is more pronounced than that from the introduction of a second single photon source.

CHAPTER 3

POLARIZATION MEASUREMENTS:

COMPENSATING MICROSCOPE RETARDANCE

3.1 Introduction

Defects in crystals almost universally absorb and emit light with a particular polarization preferentially. The details of these preferred polarization state are related to the defect's point group, symmetry axis, and coupling to the crystal's band structure. These considerations are discussed in *Chapter 5*. The purpose of this Chapter is to outline the subtleties of experimentally measuring these preferred polarization states. In particular, we shall outline the effect of retardances introduced by the microscope. We will discuss measuring these retardances and compensating for them. The problem of calibrating the polarization state of the exciting and collected light is discussed in *Chapter 7.*

A typical absorption measurement is shown in Figure 3.1a. In this case a desired polarization state P_A of exciting light is created at the point A by the combination of a monochromatic laser and a polarization generator. In the experiments of *Chapter 5*-*7*, the generator consists of a linear polarizer followed by a rotatable half wave plate that creates an arbitrary linearly polarized state. The exciting light then encounters optical elements of the confocal microscope. These optical elements include, but are not limited to, mirrors, lenses, beam splitters, and optical filters. Each of these elements

may introduce a wavelength-dependent retardance to the exciting light that corrupts the purity of its state. These retardances may collectively be modeled by a matrix $M(\lambda)$, such that the polarization state at B becomes:

$$P_B = M(\lambda)P_A. \tag{3.1}$$

In *Section 3.3* we outline our approach for compensating for this detrimental effect by instead generating the polarization state $M^{-1}(\lambda)P_A$ at the point A, where λ is the wavelength of the exciting light.

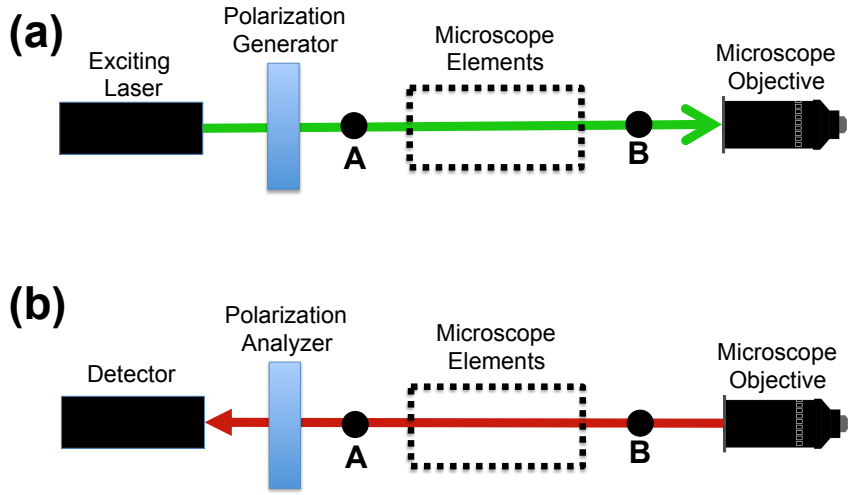

Figure 3.1: Typical polarization setup for absorption (a) and emission (b) measurements.

Similarly, a typical measurement of the polarization state of the emitted light is shown in Figure 3.1b. In this case, light is collected by the microscope and has a true polarization $P_B(\lambda)$ at the point B. Note that in this case the polarization state of the light may vary with the emission wavelength. The microscope elements again introduce wavelength-dependent retardances to the collected light:

$$P_A(\lambda) = W(\lambda)P_B(\lambda). \tag{3.2}$$

In *Section 3.3* we also outline an approach for offsetting this detrimental effect by introducing a compensating optic at the point A. This compensating optic will be selected to introduce the appropriate retardance, $W^{-1}(\lambda)$, at the wavelength(s) of interest.

3.2 Calibrating the Compensator

To measure the retardance of an optical element, or to introduce an arbitrary retardance, one typically uses a variable compensator. In this thesis we use a Soleil-Babinet compensator, available from Thorlabs as part number SBC-VIS. The compensator must first be calibrated at the wavelength of interest (excitation laser wavelength for absorption measurements and a test laser wavelength for emission measurements). Below we have reproduced, with slight modifications, the procedure for calibrating the compensator, adapted from the Thorlabs user manual available at: https://www.thorlabs.com.

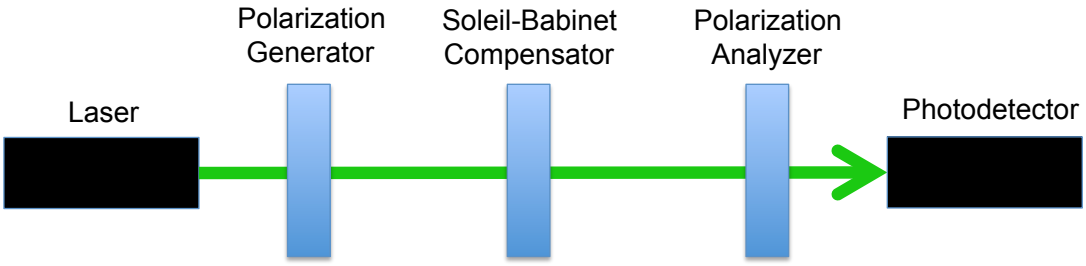

Figure 3.2: Setup for Calibration Procedure

1. Set up the crossed polarizer configuration as shown in Figure 3.2.
2. With the compensator removed from the setup, rotate the analyzer so that the intensity transmitted to the photodetector (not single-photon detector, but rather a power meter) is minimized. At this point the polarizers are crossed. If the calibration laser is polarized, it may be necessary to first rotate the generator so that the generator does not block the laser.
3. Insert the compensator in between the two polarizers. Adjust the tip/tilt adjustment so that the compensator is perpendicular to the optical beam. This is best done by observing the back reflection from the compensator to the test laser and adjusting the compensator so that the reflected spot is close to the laser output aperture.
4. At this point there should be some light transmitted into the photodetector. Loosen the rotation locking thumb screw and rotate the compensator until the transmitted spot is extinguished. Tighten the thumb screw. At this point the fast axis of the compensator is aligned with one of the transmission axes of the two polarizers.
5. With the rotation dial locked in place, rotate the compensator to the next $45°$ detent stop. There should be some light transmitted to the photodetector unless the compensator happens to be at exactly one full wave of retardance.
6. Adjust the micrometer until the spot is extinguished. This is the first of two null to be used as a full wave reference.

7. Press the ZERO/ABS button on the micrometer to reset the display to 00.000.
8. Continue adjusting the micrometer so that the laser transmits through both polarizers again. Continue adjusting in this direction until the spot extinguished. This is the second null.
9. Record the micrometer reading at this position. The distance indicated on the micrometer, X_{CAL}, corresponds to the calibration distance equal to one full wave of retardance at the test laser wavelength.

3.3 Correcting Path Retardance

In *Section 3.1* we introduced how path retardances uniquely affect both the exciting and collected light. Sometimes a suitable solution for compensating the exciting (collected) light is to place an available wave plate at the point A in the relevant configuration of Figure 3.1 and orient it to maximize the extinction ratio at the microscope objective (detector). Here we introduce a more systematic approach that directly measures the retardance of the optical elements at a particular test wavelength. Once the retardance of the microscope is measured at a particular test wavelength, it may be compensated by placing a compensating optic with the same retardance at the point A. For emission measurements the compensation is optimized at a singular wavelength and a wavelength-dependent calibration must in general be carried out (*Chapter 7*). The procedure below is adapted form the Thorlabs

user manual (https://www.thorlabs.com) and outlines how to measure the retardance of an arbitrary "Device Under Test" (DUT), which in our case is the collection of microscope elements in Figure 3.1.

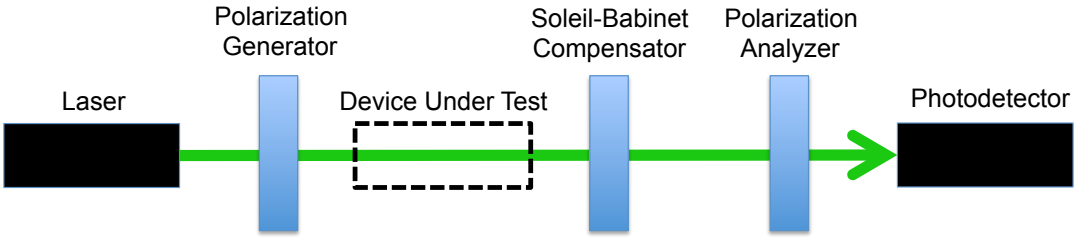

Figure 3.3: Arrangement of compensator to measure retardance of DUT.

1. Set up the crossed polarizer and DUT as shown in Figure 3.3. Make sure the polarizers are cross-polarized. Note that the laser may be the exciting laser or, for collection measurements, a test laser at the wavelength of interest.
2. With the compensator removed, the light intensity at the photodetector will likely be nonzero. Jointly rotate both polarizers, keeping them cross-polarized, until the intensity transmitted to the photodetector is minimized.
3. Insert the compensator perpendicular to the optical path such that its fast axis is aligned with the polarization generator.
4. Rotate the polarization generator and the polarization analyzer by $45°$. Also rotate the compensator to $45°$. Note that here we effectively rotate the light polarization instead of the DUT, because in practice we cannot rotate the entire confocal microscope.

5. Adjust the micrometer on the compensator until the light transmitted to the photodetector is a minimum. Record the micrometer reading at this point as X_{SBC}.
6. The retardance of the microscope at the test wavelength can now be calculated from the equation $N_{DUT} = 1.0 - X_{SBC}/X_{CAL}$, where N_{DUT} is the retardance of the microscope and X_{CAL} is taken from the calibration in *Section 3.2*.

CHAPTER 4

A SINGLE-MOLECULE APPROACH TO ZNO DEFECT STUDIES: SINGLE PHOTONS AND SINGLE DEFECTS [1]

4.1 Chapter Abstract

Investigations that probe defects one at a time offer a unique opportunity to observe properties and dynamics that are washed out of ensemble measurements. Here we present confocal fluorescence measurements of individual defects in ZnO nanoparticles and sputtered films that are excited with sub-bandgap energy light. Photon correlation measurements yield both antibunching and bunching, indicative of single-photon emission from isolated defects that possess a metastable shelving state. The single-photon emission is in the range ~560 – 720 nm and typically exhibits two broad spectral peaks separated by ~150 meV. The excited state lifetimes range from 1 – 13 ns, consistent with the finite-size and surface effects of nanoparticles and small grains. We also observe discrete jumps in the fluorescence intensity between a bright state and a dark state. The dwell times in each state are exponentially distributed and the average dwell time in the bright (dark) state does (may) depend on the power of the exciting laser. Taken together, our measurements demonstrate the utility of a single-molecule approach to semiconductor defect studies and highlight ZnO as a potential host material for single-defect based applications.

4.2 Introduction and Background

4.2.1 Motivation

ZnO is a material of choice for a wide range of applications in optoelectronics [68–70] due to its piezoelectricity, wide bandgap (~3.3 eV), and large exciton binding energy. In particular, polycrystalline ZnO films are proving useful in photovoltaic applications as transparent conductors [71–78]. Because defects often play a pivotal role in determining the bulk electrical, optical, and magnetic properties of materials, the identification and function of defects in ZnO remains the subject of intense study [79–89]. For ZnO to have its anticipated impact, long-standing questions regarding the defects, for example their role in unintentional n-type conductivity [79,83,84], must be resolved.

Prior ZnO defect studies have examined photoluminescence [90–102], electron paramagnetic resonance [87,93,95,103–107], and magnetic resonance [87,94,98,105] of defect *ensembles*. Such measurements integrate over many instances of a particular defect species and are consequently unable to observe defect-to-defect variability and single-defect dynamics. Minor differences in the emission spectrum of individual defects, which result from sample inhomogeneities, may produce an ensemble spectrum that appears broadened or structureless. Ensemble measurements also risk

convolving signal from defects of different structural origin, making it difficult to assign a particular bulk property to a particular defect species.

In this work we evade the ensemble average by studying individual ZnO defects, one at a time, using single-molecule microscopy techniques [9,10,66,108–113]. We observe excited state lifetimes ranging from 1 - 13 ns. We also observe discrete jumps in the fluorescence intensity between a bright state and a dark state. The dwell times in the bright (dark) state are exponentially distributed with an average dwell time that does (may) depend on laser power. Our results are unobtainable by ensemble methods and demonstrate that single-molecule microscopy techniques are a useful tool for probing properties that are hidden in more conventional studies.

This work is also motivated by the potential application of defects in quantum information technology [20,114–117] and precision sensing [15,16,18,118]. Single defects in wide bandgap semiconductors constitute a spatially localized quantum system that may be individually addressed. The nitrogen-vacancy (NV) center in diamond, a point defect that consists of a substitutional nitrogen atom adjacent to a lattice vacancy, is one example. NV centers possess a spin triplet ground and excited state and a metastable singlet state, all of which are contained inside the diamond bandgap [13,119]. The spin state of individual NV centers may be initialized, measured, and controlled at room temperature [14], making them promising qubit candidates. Although NV centers have proven to be a valuable spin system for fundamental investigations of quantum information science, the

diamond host material is one constraint to the scalability of NV-based applications. Single-crystal diamond substrates are small, expensive, and have minimal epitaxial compatibility with other materials. Moreover, standard nanophotonic fabrication techniques are not easily extended to diamond substrates. These limitations are less pertinent for a material like ZnO, which is inexpensive, abundant, and has well-developed fabrication and growth techniques [120,121]. These practical considerations have spurred a search for NV-like defects in more conventional wide bandgap semiconductors [20] most notably ZnO [30] and SiC [25,122,123]. In the case of ZnO, Morfa *et al*. [30] recently reported antibunching, bunching, and spectral measurements from ZnO defects that they ascribed to a Zn vacancy. Despite this promising start, a more thorough understanding of ZnO single-defect properties, including photodynamics and coupling with the local environment, is required before ZnO defects can be seriously regarded as a candidate semiconductor defect-based qubit.

4.2.2 Isolating Single Defects

The bandgap energy, E_G, of a semiconductor corresponds to the theoretical minimum photon energy that may be absorbed by that material. In real materials this absorption threshold is typically reduced by point defects, such as a lattice vacancy, that introduce spatially localized states inside the bandgap [124–126]. In this work (Figure 4.1a), we excite defect fluorescence

by focusing sub-E_G green light (2.3 eV) onto ZnO (E_G = 3.3 eV) using a numerical aperture 0.7 microscope objective. Green light is a convenient excitation source because it is compatible with both diamond NV centers and the single defects in ZnO examined here. In general, any excitation source with sub-E_G photon energy could be suitable for investigations of single defects provided it excites only a single emitter within the confocal volume. Here, the green light selectively excites single defect states because these 2.3 eV photons do not possess sufficient energy to excite carriers across the ZnO bandgap and because the defects we study are dilute. The subsequent fluorescence, which is red-shifted from its absorption energy due to phonon coupling, is detected using either a single-photon sensitive avalanche photodiode (APD) or a spectrometer. This approach is sufficiently sensitive to measure in the single-defect limit.

To ensure we study defects one at a time, we measure the second-order correlation function, $g^{(2)}(\tau)$, of the emitted photons. For stationary processes this function is given by [65]

$$g^{(2)}(\tau) = \frac{p_e(\tau|0)}{p_e^{st}}, \tag{4.1}$$

where $p_e(\tau|0)$ is the conditional probability of emitting a photon at time $t = \tau$ supposing a photon was emitted at time $t = 0$ and $p_e^{st} = p_e(\pm\infty|0)$ is the steady state probability of emitting a photon. Because a defect returns to its ground state when emitting a photon, the limiting behavior for a single defect is $p_e(0|0) = 0$. Thus, an isolated defect has $g^{(2)}(0) = 0$ and $g^{(2)}(\pm\infty) = 1$. The

dip at $\tau = 0$, known as an antibunching dip, is the signature of single-photon emission; it results from the fact that once a quantum system emits a photon, it cannot emit a second until it has been re-excited and subsequently re-relaxes to the ground state.

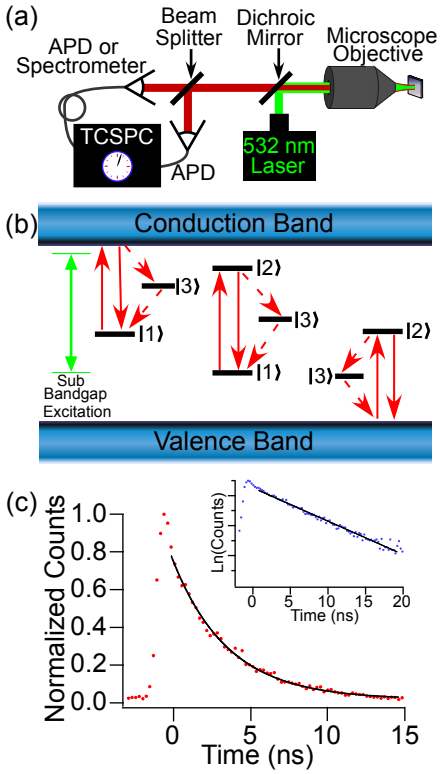

Figure 4.1: (a) Schematic of confocal microscope used to probe single defects. Sub-bandgap energy green light excites local defect states and the subsequent emission is detected by an APD sensitive to single photons or by a spectrometer. A time correlated single photon counting (TCSPC) module enables measurement of $g^{(2)}(\tau)$ for verification that a single defect is being studied. (b) Three models of defect levels consistent with the antibunching/bunching measurements we present. Each model admits a ground state $|1\rangle$, an excited state $|2\rangle$, and a metastable state $|3\rangle$. The allowed transitions are illustrated as arrows and the dashed arrows correspond to non-radiative decay pathways. In the middle model, all defect states are contained inside the bandgap and thus none of the transitions couple distinct defect charge states. In the left (right) model, the excited state $|2\rangle$ is above (below) the conduction (valence) band minimum (maximum) and thus the $|1\rangle \rightarrow |2\rangle$ excitation involves an ionization of the defect. (c) Lifetime measurement of defect 1 using a pulsed laser. The inset is the same data on a log scale and serves to verify that the decay is a pure exponential.

Figure 4.1a illustrates how $g^{(2)}(\tau)$ is measured using a Hanbury Brown and Twiss setup. The fluorescence passes through a 50/50 beam splitter and is detected by one of two APDs. The delay between successive photon detection events at each APD is computed by a time correlated single photon counting (TCSPC) module. The normalized distribution of these delay times is equivalent to $g^{(2)}(\tau)$ in the limit that τ is much smaller than the average time between detection events [12]. Figure 4.2 shows several representative $g^{(2)}(\tau)$ curves produced using this method. Note that $g^{(2)}(\pm\infty) = 1$ as expected but $g^{(2)}(0) \neq 0$. Experimental non-idealities including detector dark counts, background counts, detector jitter, and finite histogram bin width prevent most experimental antibunching dips from reaching their theoretical minimum value of zero. Because two identical single-photon emitters within the detection volume of the microscope theoretically yield $g^{(2)}(0) = 0.5$ [67], dips extending below 0.5 are typically regarded as verification that only one quantum emitter is being studied. However, defect-to-defect variations in fluorescence intensity and the existence of blinking effects (discussed later) allow small ensembles of defects to produce antibunching dips extending below 0.5. We note that all data presented in this work exhibit antibunching dips extending below 0.4.

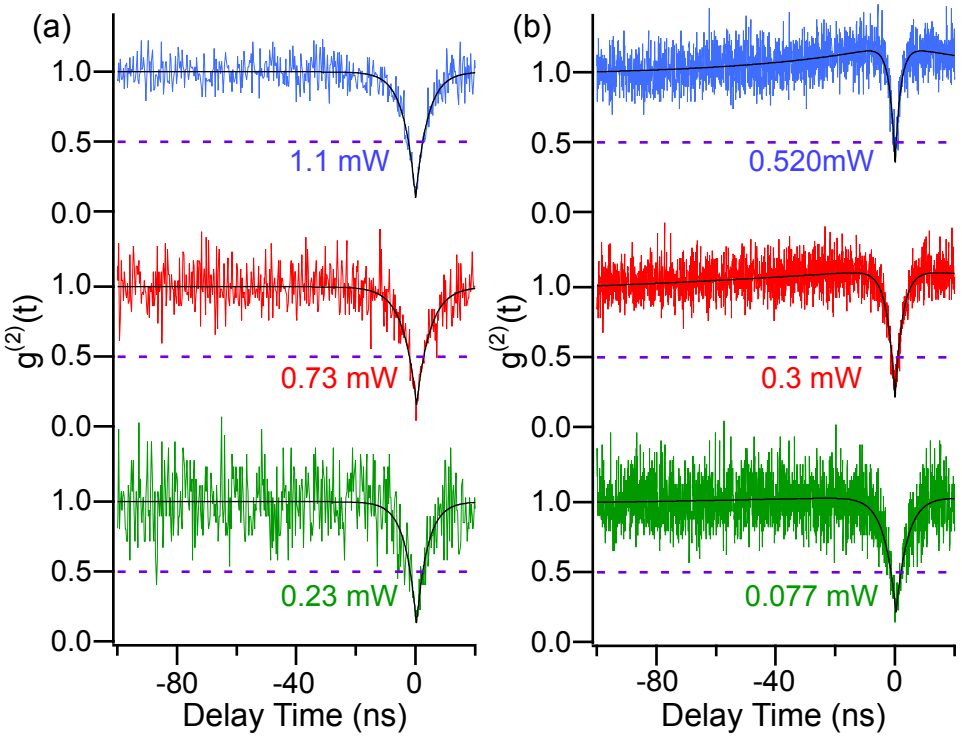

Figure 4.2: Representative $g^{(2)}(\tau)$ curves for defect 1 (a) and defect 2 (b) acquired for several different laser powers. In each curve the antibunching dip at $\tau = 0$ extends below the dashed line at 0.5, verifying that a single defect is being studied. Note in (b) that as laser power is increased the antibunching dip sharpens and bunching $\left(g^{(2)}(\tau) > 1\right)$ becomes evident, verifying at least 3 defect states exist.

4.2.3 Rate Model

It is useful to associate a ground state $|1\rangle$, an excited state $|2\rangle$, and a metastable shelving state $|3\rangle$ with a given defect. These states are not necessarily single-electron states and they may possess spin degrees of freedom. Three possible state configurations are illustrated in Figure 4.1b. In one case (Figure 4.1b, middle) the states are completely contained inside the

bandgap; we shall refer to this as an “internal transitions”. In separate scenarios (Figure 4.1b, left and right), some of the states are positioned in either the conduction or valence band; we shall refer to these as “band transitions”. In all three configurations, a defect in the ground state $|1\rangle$ may absorb a photon of sufficient energy and enter the excited state $|2\rangle$. The excited state offers two decay pathways: a relaxation directly to the ground state or a non-radiative intersystem crossing via the metastable state to the ground state. Photon emission may accompany the direct $|2\rangle \rightarrow |1\rangle$ relaxation with a likelihood known as the quantum efficiency. Neglecting coherences, a rate model describes state population evolution [64]:

$$\frac{d}{dt}\begin{pmatrix} P_{|1\rangle} \\ P_{|2\rangle} \\ P_{|3\rangle} \end{pmatrix} = \begin{pmatrix} -r_{12} & r_{21} & r_{31} \\ r_{12} & -r_{21} - r_{23} & 0 \\ 0 & r_{23} & -r_{31} \end{pmatrix}\begin{pmatrix} P_{|1\rangle} \\ P_{|2\rangle} \\ P_{|3\rangle} \end{pmatrix}. \tag{4.2}$$

Here $P_{|i\rangle}$ is the probability of occupation of state $|i\rangle$ and r_{ij} is the transition rate from state $|i\rangle$ to state $|j\rangle$. Note that while the transition rates may vary during the course of an experiment due to local fluctuations, for this analysis we ignore the time dependence of the transition rates.

Equation 4.2 may be used to model the second-order correlation function, $g^{(2)}(\tau)$, introduced earlier (Equation 4.1). Because the probability of emitting a photon is proportional to $P_{|2\rangle}$, and an emission event is accompanied by a relaxation to the ground state, $p_e(\tau|0)$ is proportional to $P_{|2\rangle}(\tau)$ with initial condition $\left(P_{|1\rangle}, P_{|2\rangle}, P_{|3\rangle}\right)(t = 0) = (1,0,0)$ [64]. We find that in the absence of background counts

$$g^{(2)}(\tau) = 1 + Ae^{\lambda_1|\tau|} - (1+A)e^{\lambda_2|\tau|}, \quad (4.3)$$

where A is determined by the transition rates and λ_1, λ_2 are the nonzero eigenvalues of the rate matrix appearing in Equation 4.2. Note that because Equation 4.3 is bi-exponential, photon bunching is possible. Photon bunching, evident in the uppermost curve of Figure 4.2b, occurs when $g^{(2)}(\tau) > 1$. Bunching is absent in 2-state systems because such systems only permit mono-exponential solutions for $P_{|2\rangle}(\tau)$. Thus, the observation of photon bunching confirms that the system being studied has at least three states.

The transition rates appearing in Equation 4.2 and illustrated in Figure 4.1b characterize the defect's optical dynamics. They determine the defect's fluorescence intensity and provide insight into its oscillator strength. The excited state lifetime, which is defined as $\tau_{|2\rangle} = (r_{21} + r_{23})^{-1}$, is of particular importance and may be determined directly using a 532 nm pulsed excitation and time-correlated photon counting. A representative measurement for a single defect is shown in Figure 4.1c. The solid line represents an exponential fit to the data. The inset, which displays the same data on a log scale, verifies that the decay is indeed a pure exponential and is characterized by a single time constant, $\tau_{|2\rangle}$.

4.2.4 Photodynamics

Single-molecule microscopy requires temporal averaging because of the comparably low photon signal that is detected from one defect (~30

kCounts/s). Consequently, properties that vary over a timescale shorter than a measurement will remain hidden. Some temporal variations may be monitored in real time, however, by observing the fluorescence intensity, or photon emission rate, under continuous excitation. In principle, a defect's fluorescence intensity is completely determined by the transition rates and follows a Poisson distribution. However, single-photon sources, including the ZnO defects investigated here, rarely exhibit stable Poissonian emission. Instabilities in fluorescence intensity resulting from spectral diffusion [127–129], changes in the local environment [129,130], photobleaching [129,131], and the presence of a long-lived metastable state [130,132–134] have been reported, and sophisticated models have been developed to address these issues [9,63–65,135–137]. Although fluorescence intensity instabilities have been viewed negatively in the context of single-photon sources, they may potentially be exploited to understand the system under study or as sensing channel [138]. For example, a defect's fluorescence intensity may serve as a sensitive environmental probe of its nanoscopic environment. Alternatively, a defect's fluorescence intensity may potentially be controlled via magnetic fields, electric fields, or stress.

Here we examine blinking, whereby the fluorescence intensity exhibits discrete jumps between a bright state and a dark state. Blinking is a common feature of isolated quantum systems [139,140] and has been reported in many systems including quantum dots [141–144], single molecules [129,130,132,134,145–149], nanocrystals [131,150], defects in

SiC [25], and diamond NV centers [138,151,152]. The mechanism(s) responsible for blinking may be investigated by constructing the distribution of dwell times spent in the bright state, τ_{BS}, and the dark state, τ_{DS}, for several laser powers or temperatures. Previous investigations have separately reported a power law [130,131,141,144,147] and exponential [133,138,142,148] distribution for blinking dwell times in quantum dots, nanocrystals, single molecules, and single defects. Because a quantum system emits no photons while trapped in a metastable state, a long-lived metastable state ($\tau_{|3\rangle} > \mu s$) is a commonly cited cause for blinking [129,133,134,145,148]. In this case one expects the dwell times in each state to be exponentially distributed and the average dwell times, $\langle \tau_{BS/DS} \rangle$, to obey [129]

$$\frac{1}{\langle \tau_{BS} \rangle} = \frac{r_{12} r_{23}}{r_{21} + r_{23}}, \tag{4.4}$$

$$\frac{1}{\langle \tau_{DS} \rangle} = r_{31}, \tag{4.5}$$

where it is assumed that $r_{12} \ll r_{21} + r_{23}$. Alternatively, jumps from a bright state to a dark state could result from the emergence of non-radiative $|2\rangle \rightarrow |1\rangle$ decay channels that serve to reduce $\tau_{|2\rangle}$ and quench the fluorescence intensity by reducing the quantum efficiency [131,153–155]. Because in this scenario the fluorescence intensity is quenched but not extinguished, the emitter is always optically active, and one expects single-photon emission in both the bright state and the dark state (in contrast to blinking caused by a long-lived metastable state, which only exhibits

antibunching in the bright state). As a third possibility, blinking may result from either a thermal- or photo- induced ionization that couples two distinct charge states of distinguishable fluorescence intensity [152]. Note that we have not presented an exhaustive or mutually exclusive list of blinking mechanisms and separate mechanisms may coexist.

4.3 Experiment

4.3.1 Sample Details

We investigated nanoparticle (NP) ZnO and sputtered ZnO films. We emphasize these sample types largely due to their technological significance as transparent conducting electrodes and piezoelectric transducers [71–78,156–166]. The NPs were suspended in methanol prior to being drop-cast onto a fused silica substrate. We investigated two separate ZnO NP types. Both varieties are commercially available from Sigma-Aldrich as product numbers 677450 (Type I) and 204951 (Type II). We observe a lower density and fluorescence intensity of defects in Type II as compared with Type I. Additionally, we observed antibunching in each type but did not observe $g^{(2)}(0) < 0.5$ in Type II NPs. Thus all presented results are from Type I NPs. X-ray diffraction (XRD) measurements indicate that the NPs are wurtzite structure and an inductively coupled plasma analysis reveals that the investigated NPs possess 1.8% Al by weight. Figure 4.3 is a transmission electron microscope (TEM) image of the NPs. The NPs preferentially

coalesce, range in size from ~10 nm to more than 200 nm, and exhibit a variety of shapes.

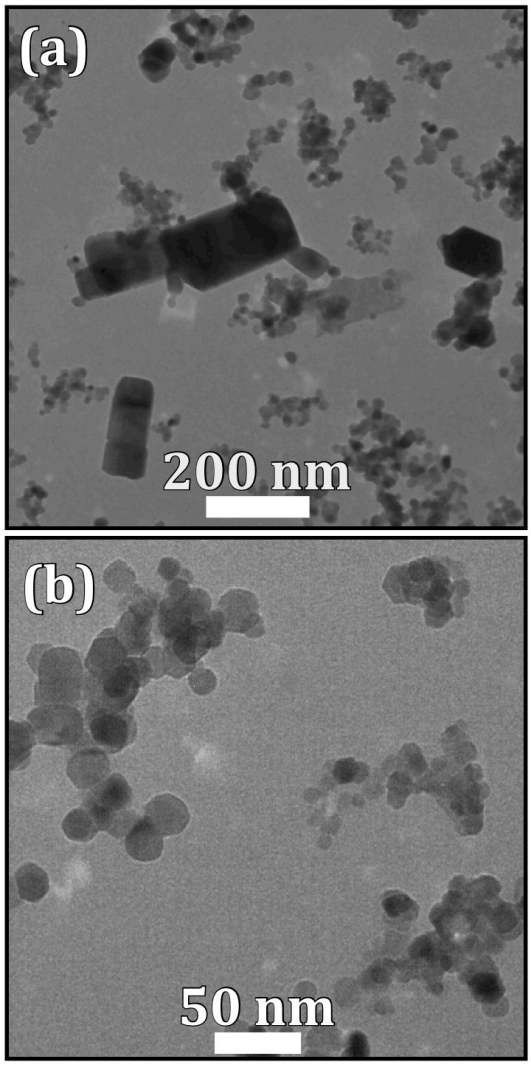

Figure 4.3: (a) Wide area transmission electron microscope (TEM) image of the investigated ZnO NPs. NPs larger than 200 nm are evident alongside clusters of smaller NPs in the range 10 – 30 nm. (b) Magnified TEM image of four NP clusters.

ZnO films were grown on fused silica substrates by reactive DC sputtering. The sputter chamber was pumped to a base pressure of $5 \cdot 10^{-7}$ Torr. Subsequently Ar and O were introduced into the chamber with

partial pressures of 4 mTorr and 1 mTorr, respectively. The film thickness was monitored using a quartz crystal monitor that was calibrated using a contact profilmeter. XRD measurements indicate that our sputtered films are wurtzite, polycrystalline with a mean grain size of 50 nm, and are ⟨002⟩ orientated.

All presented data (NPs and sputtered films) are from samples annealed at 500° C in air for 30 minutes. We also studied unannealed samples, but we were unable to isolate any single defects prior to annealing. The fused silica substrates used for both sputtered film growth and NP drop-casting were chosen for their low background fluorescence intensity and absence of native single-photon emitters.

The emission spectrum of individual ZnO defects were investigated and several of these spectra are shown in Figure 4.4. Each spectrum has been normalized and the dashed line at ~580 nm denotes the cutoff of a long-wave pass filter edge. Ten of the 16 spectra we investigated are well characterized by two Gaussian-distributed peaks separated by roughly 150 meV. Each of these spectral peaks originates from the same defect, not from another nearby defect or from background emission. The results are included in Table 4.1. We found the location of the low (high) energy peak to be in the range of 1.82 – 1.97 eV (1.91-2.08 eV). These findings are consistent with prior work [30], although we note that our results are of a higher energy than those reported previously. We did not observe a room-temperature zero phonon line, which is consistent with the strong defect-phonon coupling present in the spectral emission [167].

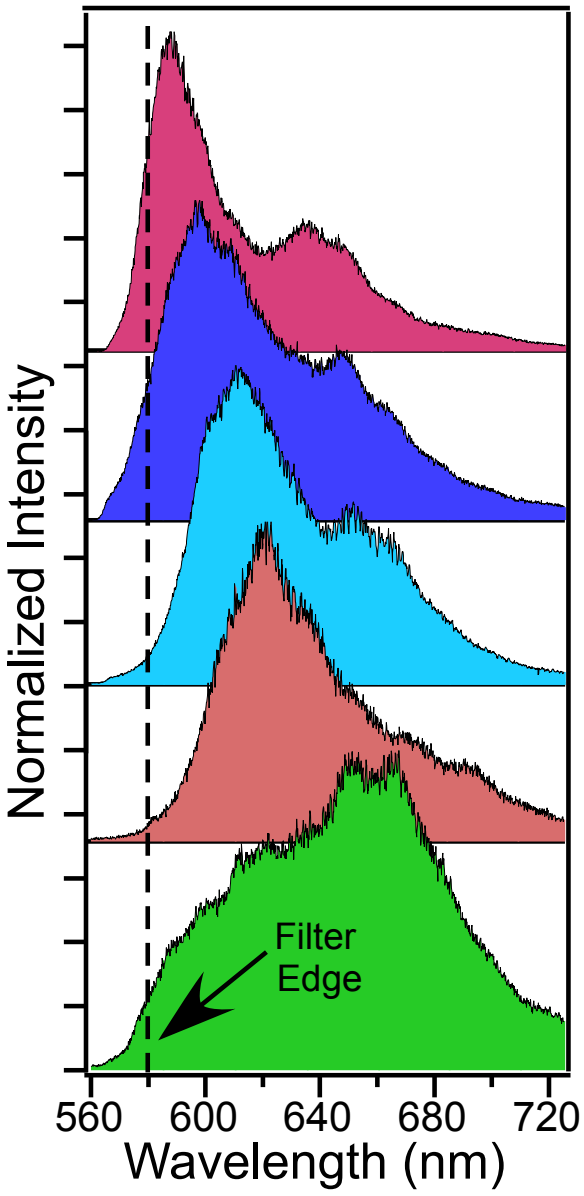

Figure 4.4: Normalized emission spectra for 5 of the 19 individual defects investigated. The emission is plotted in the range ~ 560 - 720 nm and is typically characterized by two broad peaks that may be fit by Gaussian functions. Each spectrum arises exclusively from a single defect and not two or more. The dashed line at ~ 580 nm denotes the cutoff of a long-wave pass filter edge

Defect	Sample	$\tau_{\|2\rangle}$ (ns)	$\tau_{\|3\rangle}$ (ns)	Spectral Peak Locations (eV)	Spectral Peak Separation (meV)	Fluorescence Intensity
1	NP	4.8 +/- 0.2		(1.91 , 2.04)	130	Stable
2	NP	3.2 +/- 0.1	52 +/- 5			Fluctuates
3	NP	4.53 +/- 0.03				On/Off
4	NP	2.17 +/- 0.03	280 +/- 200	(1.88 , 2.06)	180	On/Off
5	NP	1.66 +/- 0.03		(1.94 , 2.08)	340	On/Off
6	NP	1.29 +/- 0.05		(1.94, 2.07)	130	On/Off
7	NP	3.37 +/- 0.04				On/Off
8	NP	1.92 +/- 0.03	Unknown			Stable
9	NP	1.79 +/- 0.04	100 +/- 15	(1.93 , 2.08)	150	Stable
10	NP	1.66 +/- 0.04	44 +/- 2			Fluctuates
11	NP	4.6 +/- 0.2	100 +/- 20	(1.97 , 2.11)	140	Fluctuates
12	NP	3.25 +/- 0.03	221 +/- 5	(1.89 , 2.03)	140	Fluctuates
13	NP	3.6 +/- 0.3				Fluctuates
14	NP	7.3 +/-0.2		(1.89 , 2.06)	170	Fluctuates
15	20 nm SP	3.3 +/- 0.1		(1.95 , 2.08)	130	On/Off
16	71 nm SP	5.2 +/- 0.3				Fluctuates
17	71 nm SP	13.4 +/- 0.6				Fluctuates
18	71 nm SP	8.8 +/- 0.2	Unknown			Fluctuates
19	71 nm SP	6.9 +/- 0.03		(1.82 , 1.91)	90	Fluctuates

Table 4.1: Summary of the 19 single defects studied. The sample types include nanoparticle (NP) ZnO and sputtered ZnO films (SP) for which the film thicknesses have been listed in nm. All lifetimes were determined by simultaneously fitting a power series of $g^{(2)}(\tau)$ curves and all uncertainties are calculated using the chi-squared curvature matrix [168]. When bunching was evident but a reliable determination of $\tau_{|3\rangle}$ was not possible, we have listed $\tau_{|3\rangle}$ as "Unknown". For defects whose emission spectra is characterized by two broad Gaussian peaks, we have listed the midpoint of each peak in eV and have also included the peak-to-peak separation in meV. Lastly, the fluorescence intensity of each defect is characterized as "Stable", meaning well described by Poissonian statistics, "On/Off" meaning discrete blinking between two "Stable" states of distinguishable fluorescence intensity, and "Fluctuates", meaning intensity fluctuations that cannot be described as "Stable" or "On/Off".

4.3.2 Transition Rates

Although the excited state lifetime may be directly determined using pulsed excitation, that approach does not measure the metastable state lifetime

$(1/r_{31})$ and cannot decouple the direct (r_{21}) and intersystem crossing (r_{23}) pathways for leaving the excited state. These considerations motivate us to determine the transition rates by measuring $g^{(2)}(\tau)$ for several different laser powers. The excitation rate r_{12} is proportional to laser power and may therefore be readily varied over several orders of magnitude. We simultaneously fit a series of $g^{(2)}(\tau)$ (antibunching) curves, each of which was acquired from the same defect but at a different laser power, using Equation 4.3. In the fit r_{21}, r_{23}, and r_{31} are kept constant across all curves and r_{12} is constrained to increase linearly with excitation power. The best-fit for the series of curves was determined using a chi-squared minimization procedure. We emphasize that the fit is not obtained by directly modifying the eigenvalues λ_1 and λ_2. Instead, we use the analytic form of these eigenvalues and vary the transition rates as free parameters, thus enabling determination of all transition rates simultaneously.

Two examples of an antibunching power series are displayed in Figure 4.2. In each curve the antibunching dip at $\tau = 0$ extends below the dashed line located at 0.5, verifying that a single defect is being probed. The data from Figure 4.2a were acquired from the same defect for which we measured the excited state lifetime using pulsed excitation (Figure 4.1c). By fitting this antibunching power series, we determine an excited state lifetime of 4.8 ± 0.2 ns. This result is in close agreement with the pulsed excitation measurement of 4.5 ± 0.3 ns, thus corroborating the efficacy of our approach.

Several noteworthy trends are displayed in Figure 4.2b. Firstly, the sharpness of the antibunching dip increases with increasing excitation power. Additionally, photon bunching, which often emerges as excitation power is increased, is evident and confirms that the defect has at least three states. Note that though the data in Figure 4.2a show no signs of bunching, there may nonetheless still be three states present. That is, the absence of bunching in $g^{(2)}(\tau)$ neither verifies nor refutes that a third state exists.

Using the method described above we determined the transition rates for 19 individual ZnO defects. Our results are displayed in Table 4.1. We computed uncertainties in lifetime measurements by using the chi-squared curvature matrix as outlined by Bevington [168] and neglect other experimental sources of error. Of the defects presented, 14 are from NP samples and five are from sputtered samples. To our knowledge, this is the first report of single-photon emission from sputtered ZnO, which is promising for quantum applications because sputtered films are readily engineered and may be integrated for device applications. Seven of the 14 NP-based defects studied displayed signs of bunching and one of the five sputtered film defects exhibited bunching. While our analysis allows us to determine the metastable state lifetime, the best-fit is not highly sensitive to this parameter, and thus we are much less certain about the metastable lifetime compared to the excited state lifetime. In cases where bunching is apparent but not pronounced enough to enable a reliable determination of the metastable state lifetime, we have listed the metastable state lifetime as unknown. The metastable state

lifetimes reported here are in the range 40 to 300 ns which is in agreement with those reported previously [30].

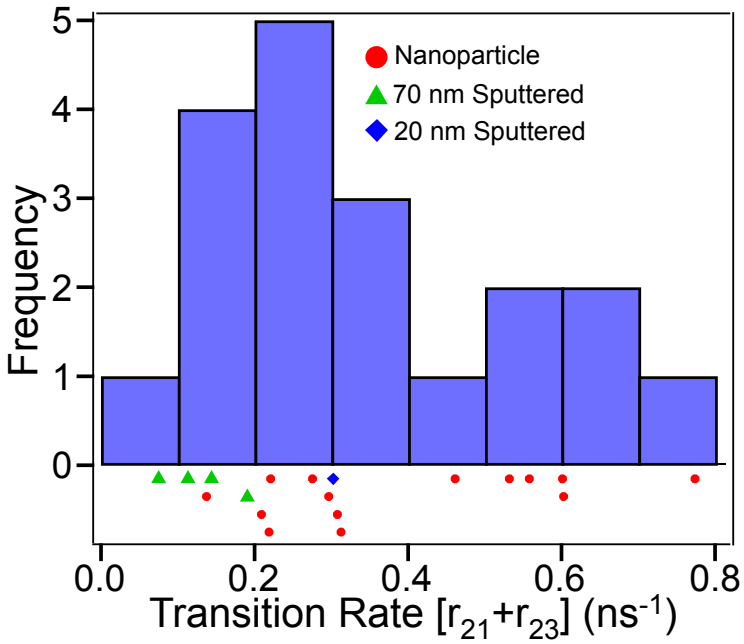

Figure 4.5: Histogram of observed transition rates ($1/\tau_{|2\rangle}$). Below the histogram bars, the transition rate for each defect studied has been represented by a marker. Note the significant overlap in rates for defects in sputtered films (triangles and diamonds) and NPs (circles). We tentatively attribute the wide spread in transition rates to variations in grain/NP size, geometry, distance to the surface, and surface chemistry rather than variations in the local carrier density.

The excited state lifetime, which we observed to range from 1.7 ns to 13 ns, exhibits much defect-to-defect variability. The variability in the rate of leaving the excited state, $1/\tau_{|2\rangle}$, is illustrated in Figure 4.5. The individual rates for each defect investigated are represented as markers situated below the histogram bars. Note that for a conduction band transition (Figure 4.1b, left) we expect $1/\tau_{|2\rangle} = n \cdot C_n$, where n is the local carrier density and C_n is the defect's electron capture coefficient. Because we have not determined the

carrier concentration in our samples, in particular the NPs, we cannot eliminate the possibility that we study a transition involving the conduction band. Thus, doping- and temperature- dependent studies are necessary to determine whether the defects studied are decoupled from the conduction band. Nonetheless, we tentatively attribute the wide spread in measured $\tau_{|2\rangle}$ to variations in NP/grain size, geometry, surface chemistry, and to differences in the defect to surface distance rather than variations in the local carrier density. It has been shown for NV centers in diamond that as the diamond host is reduced in size, non-radiative relaxation channels, which are not present in bulk diamond, emerge that serve to reduce the NV excited state lifetime [169]. Additionally, a nanodiamond's specific geometry may affect the excited state lifetime of its NV centers [170]. In fact, there is evidence that the radiative decay rates, non-radiative decay rates, and quantum efficiencies of NV centers are especially variable in nanodiamonds as large as 100 nm [171]. Because we are studying nanoparticles (~10 - 200 nm in size) and polycrystalline films (~50 nm grains), these effects may play a substantial role in governing the wide spread of $\tau_{|2\rangle}$ values that we observe.

4.3.3 Photodynamics (Blinking)

Figures 4.6a-c depict temporal variations in the fluorescence intensity of three distinct ZnO defects. In Figures 4.6 a and b (defects 3 and 4, respectively) the fluorescence intensity exhibits discrete jumps between a bright state and a

dark state. Each state is well defined and we observe Poissonian photon shot-noise statistics within each state. This situation of bright/dark blinking is contrasted by Figure 4.6c. Here the fluorescence follows a more complicated trajectory characterized by at least four levels. We have characterized the fluorescence of each defect in Table 4.1 as “stable”, meaning purely Poissonian statistics, “on/off”, meaning blinking between a bright and a dark state that each exhibit Poissonian statistics, and “fluctuates”, meaning the fluctuations in fluorescence intensity exceed the Poissonian statistical expectation. In the following analysis we focus exclusively on bright/dark blinkers, such as those seen in Figures 4.6a and b, and characterize the distribution of dwell times spent in each state before a blinking event occurs.

Blinking between a bright state and a dark state suggests a scenario whereby an individual defect is jumping between an “on” state where it emits single photons and an “off” state where it does not emit any photons at all. To test if this is indeed the case, we measured $g^{(2)}(\tau)$ separately for the bright state and the dark state by post-filtering our photon arrival times. The results of this state-selective measurement are displayed in Figures 4.6 d and e. Figure 4.6d, which was solely acquired while defect 3 was in the bright state, shows clear antibunching and confirms that the bright state corresponds to single-photon emission. Figure 4.6e, which was solely acquired while defect 3 was in the dark state, shows no evidence of antibunching and indicates that the dark state corresponds to a relatively small flux of uncorrelated background photons. Thus when defect 3 is in the dark state, it is either not

fluorescent or is fluorescent but emits into a spectral window not detectable by our setup. In either case, single-photon emission statistics are associated only with the bright state and the terms on/off and bright/dark blinking may be used interchangeably.

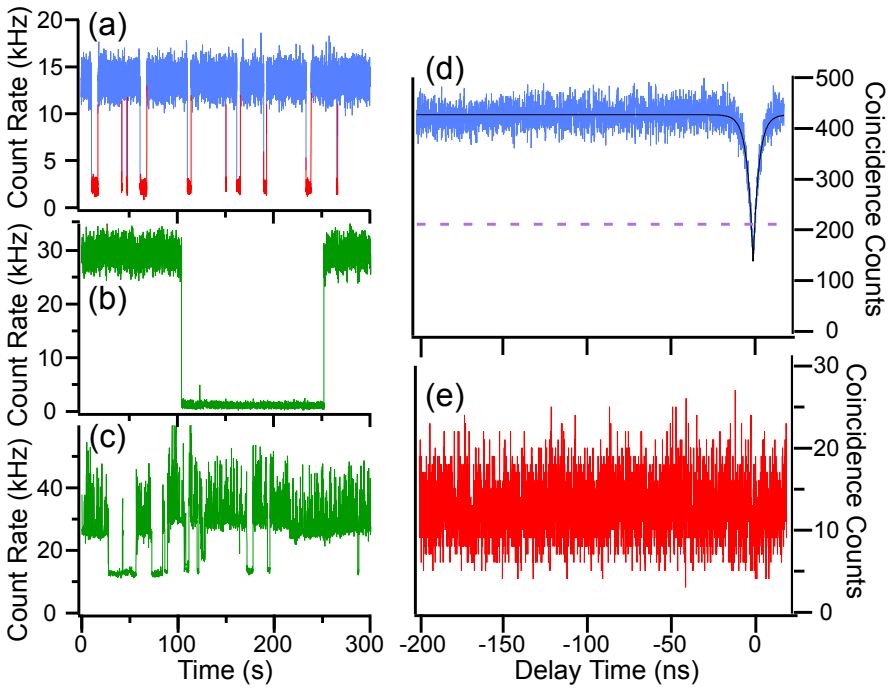

Figure 4.6: (a-c) Examples of temporal dynamics in the fluorescence intensity for three distinct defects over a time span of 300 s. Defect 3 (a) and defect 4 (b) each exhibit discrete jumps, or blinking, between a bright state and a dark state whereas the fluorescence intensity seen in (c) follows a much more complicated trajectory. For defect 3 (a), we measured $g^{(2)}(\tau)$ separately for the bright state (d) and the dark state (e). The presence of antibunching in (d) verifies that the defect is optically active and emits single photons while in the bright state. The absence of antibunching in (e) indicates that the defect is inactive, and not merely quenched, while in the dark state. Note the differences in counts between (d) and (e), indicating that the vast majority of coincidence counts are registered while the defect is in the bright state.

We investigated the distribution of dwell times for both the bright state (τ_{BS}) and dark state (τ_{DS}) of 2 separate bright/dark blinking defects. For each time bin the defect state was determined by comparing the number of photons

detected to a threshold value. This approach requires careful selection of binning times and thresholds because improper selection of these values may introduce artifacts into the measured dwell times [137,172,173]. Here we find that the dwell times in both the bright and dark states are exponentially distributed (Figures 4.7a and b, respectively) with a time constant that corresponds to the average dwell time of each state.

We measured the average rate of leaving the bright state ($\langle\tau_{BS}\rangle^{-1}$) and the dark state ($\langle\tau_{DS}\rangle^{-1}$) for defect 5 for several laser powers (Figures 4.7c and d, respectively). Figure 4.7c indicates that $\langle\tau_{BS}\rangle^{-1}$ increases as laser power is increased whereas Figure 4.7d shows no correlation between $\langle\tau_{DS}\rangle^{-1}$ and laser power. These trends are consistent with defect 5 blinking due to a long-lived metastable state ($\tau_{|3\rangle}$ ~ 50 ms) (Eqs. 4 and 5). In this scenario, each blinking event from the bright state to the dark state corresponds to the collapse of the defect's quantum state to the metastable state $\left(BS \xrightarrow{|2\rangle\rightarrow|3\rangle} DS\right)$. Alternatively, these trends are also consistent with a photo- or thermal-induced band transition that couples the excited state $|2\rangle$ to the conduction band. In such a scenario, each blinking event from the bright state to the dark state corresponds to an ionization event. Incidentally, if ionization is the mechanism, then the bright state is the energetically favorable charge state because the $BS \rightarrow DS$ transition requires optical excitation whereas the $DS \rightarrow BS$ transition does not. The data presented is insufficient to uniquely

determine the cause of blinking for defect 5. Temperature dependent blinking studies may aid in identifying the active blinking mechanism.

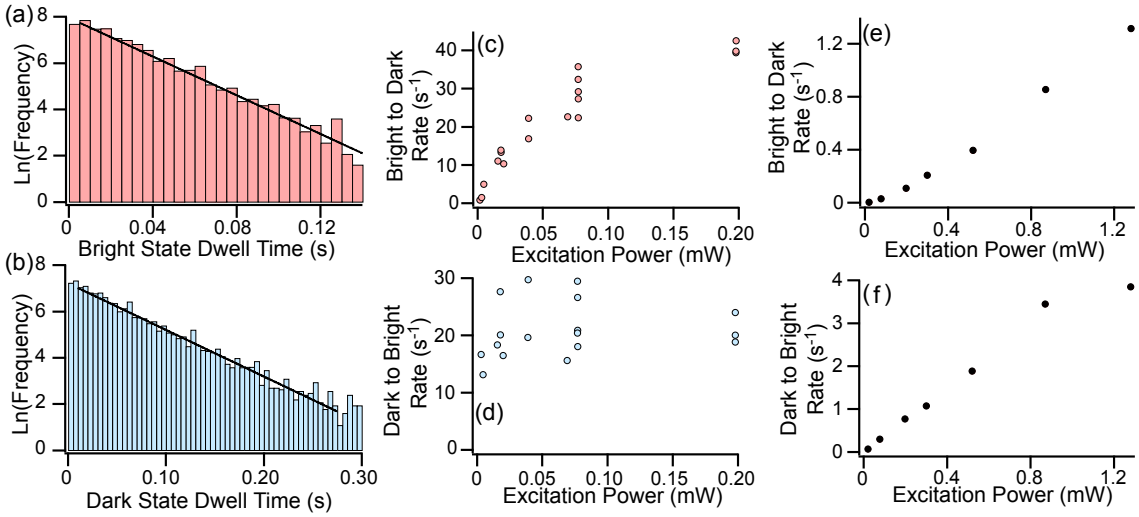

Figure 4.7: (a-b) Histogram of dwell times in the bright state (a) and dark state (b) for defect 5. Note that each distribution is purely exponential for short times and that $\langle \tau_{BS/DS} \rangle$ is on the order of milliseconds. Similar histograms were acquired for a range of laser powers and the mean transition rate $\langle \tau_{BS/DS} \rangle^{-1}$ was determined for each laser power. The results are presented for defect 5 for the bright state (c) and dark state (d). An identical analysis was performed for defect 3 and the results for the bright state and dark state are shown in (e) and (f), respectively. The dark state dwell times for defect 5 and 3 (shown in (d) and (f), respectively) exhibit qualitatively different trends that strongly suggest a different blinking mechanism is dominant for each defect.

We performed an identical dwell time analysis for defect 3, which exhibits considerably longer dwell times than defect 5. As before, the dwell times in each state are exponentially distributed and $\langle \tau_{BS} \rangle^{-1}$ increases with increasing excitation power (Figure 4.7e). However, we find that $\langle \tau_{DS} \rangle^{-1}$ also increases with increasing laser power (Figure 4.7f) for defect 3. This behavior indicates that defect 3 does not blink due to a long-lived metastable state. Additionally, because both $\langle \tau_{BS} \rangle^{-1}$ and $\langle \tau_{DS} \rangle^{-1}$ approach zero as laser power is

reduced, a purely band-assisted mechanism is unlikely. One blinking mechanism consistent with Figures 4.7e and f is a charge transfer between defect 3 and a neighboring acceptor or surface trap. In this scenario the $BS \rightarrow DS$ transition corresponds to an electron escaping the defect and becoming localized at a nearby site. The ejected electron then serves to reduce the local carrier density via Coulombic repulsion and enhance the dark state lifetime.

While the active blinking mechanisms for defect 3 and defect 5 have not been determined, their qualitative differences suggest that multiple flavors of dark state may exist [145,148,153]. If multiple dark state varieties exist, then a single defect may potentially couple to multiple types. The dark state dwell times for defect 5 (Figures 4.7b and d) are exponentially distributed with $\langle \tau_{DS} \rangle \approx 50\ ms$ for all laser powers studied. Thus observing any dwell time greater that ~10 s should be exceedingly improbable because only ~10^{-85}% of all observed dwell times are expected to be greater than 10 s. Despite this, dark state dwell times in excess of one minute were observed for defect 5. One such anomalous dwell time is denoted by the arrow in Figure 4.8a. This figure shows the fluorescence intensity of defect 5 over a time span of 500 s. Several anomalous dwell times are apparent in addition to the one that has been singled out. Note that the dense regions of the graph, such as that occurring between approximately 0 s and 150 s, are regions of rapid blinking between the bright and dark states. This is illustrated in Figure 4.8b, which displays a sub-second time window of Figure 4.8a. Evidently defect 5 is

strongly coupled to a short-lived dark state and is weakly coupled to a distinct, anomalously long-lived dark state. The anomalous dark state dwell times evident in Figure 4.8a occur too infrequently to be studied statistically. Nonetheless, the observation of such anomalous dwell times is compelling evidence that several distinct mechanisms may jointly describe the rich blinking dynamics of a single defect.

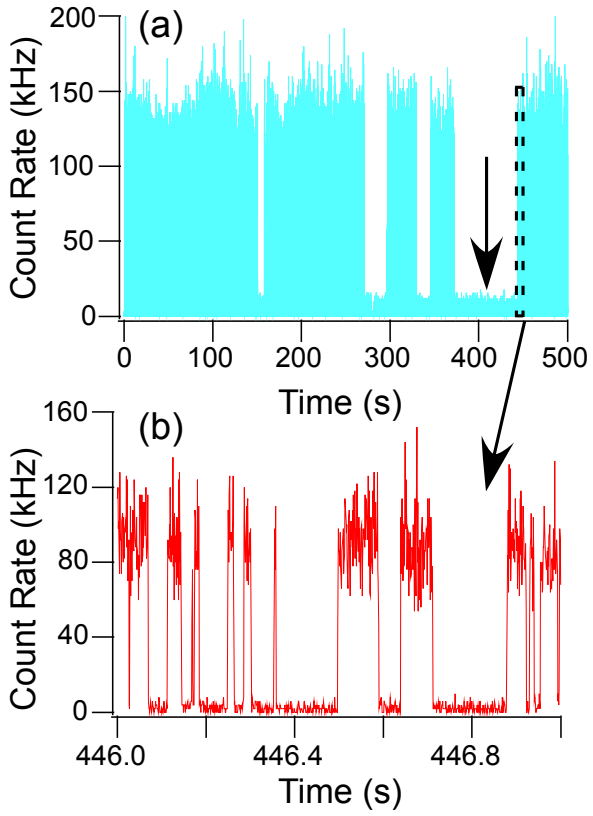

Figure 4.8: (a) The fluorescence intensity trajectory of defect 5 over a time scale of 500 s revealing anomalously long-lived dark state dwell times. The ordinary blinking of this defect is on millisecond time scales (Figures 4.6 a-d) and is illustrated in (b), which plots a sub-second time window of the fluorescence from (a). In (a) several statistically improbable anomalous dark state dwell times are evident, one of which is denoted by the solid arrow at ~ 400 s. These long-lived dark state dwell times cannot result from the same blinking mechanism that produced the exponential distribution seen in Figure 4.6d and their existence strongly suggests multiple dark state varieties may jointly couple to a particular defect.

4.4. Conclusion

We have characterized the room temperature properties and dynamics of single defects in ZnO NPs and sputtered films. The defects investigated exhibit a range of behavior with some commonalities and some differences. Similarities include absorption of 532 nm light, single-photon emission in the red, excited state lifetimes in the range ~ 1 - 13ns, and metastable state lifetimes in the range ~ 40 – 300 ns. Differences include variations in the locations of peaks in the emission spectrum, the values of the transition rates, and defect photodynamics. For defects with identical or similar structure, one may anticipate less variation in the lifetimes and emission spectra than we report here. If we study transitions involving the conduction band, then the distribution of excited state lifetimes may be explained by variations in the local carrier density. However, it has been shown for nanodiamond NV centers that the host crystal's size and geometry greatly influence the radiative decay rate, non-radiative decay rate, and quantum efficiency [169–171]. Because we are studying ZnO nanoparticles and polycrystalline grains with a range of sizes and surface geometries, similar mechanisms could explain the wide range of excited state lifetimes observed here. Additionally, variations in the local environment, such as the presence of hydrogen interstitials, have been predicted to alter the emission spectra of Zn vacancies in ZnO [174]. Thus it is possible that the defects investigated here have identical or similar structure despite the wide range of observed behavior. Recent theoretical

advancements in first-principles calculations of defect emission [175] are especially promising for understanding the defect-to-defect variability that we observe. Additionally, we note that prior theoretical work on defects in ZnO has focused on band transitions that couple distinct defect charge states [79–85]. These calculations shed light on the electrical properties of ZnO but do not address the electronic excitations of a particular defect charge state (internal transitions). If we indeed study defects with internal transitions rather than band transitions, then a thorough understanding of ZnO may require a more detailed knowledge of internal defect transitions than presently exists. Because we lack a first-principles prediction for ZnO defects matching our observations, we cannot assign a structure to the defects we study. Morfa *et al*. [30] also observed single defect fluoresce in nanoparticle derived ZnO films that they attributed to the Zn vacancy because the red emission wavelength was consistent with previous studies [87]. The fluorescence observed in this work appears at emission energies that are higher by 100 – 300 meV, which may reflect sample differences or have a distinct origin.

We also report cases of discrete blinking between a bright state, where the defect is optically active and emits single photons, and a dark state, where only a relatively small flux of background photons are incident on the detector. Whereas the rate of blinking from the bright state to the dark state increases with laser power, the rate of blinking from the dark state to the bright state may or may not increase with laser power. These two distinct dark state behaviors likely result from distinct blinking mechanisms, which is supported by statistical

evidence that a single defect may couple to multiple dark states. Future temperature dependent experiments may offer valuable clues regarding the nature of blinking in ZnO single defects.

This work illustrates the utility of a single-molecule approach to semiconductor defect studies. We focus on individual defects, thus obtaining results that are unattainable in an ensemble study. In contrast, an ensemble photoluminescence measurement of the same defects studied here would yield a weighted sum of the individual defect spectra that would be featureless except for a broad “red” photoluminescence band. Moreover, the variability in defect transition rates and the blinking dynamics would be averaged out. Our observations also suggest that the properties of single defects in ZnO are very sensitive to the local environment and that single-defect studies could be useful for understanding local variations in ZnO.

4.5 Acknowledgements

We gratefully acknowledge insightful conversations with John Lyons, Daniel Steiauf, Luke Gordon, Audrius Alkauskas, Anderson Janotti, and Chris Van de Walle from the University of California at Santa Barbara and with David Muller from Cornell University. Research support for *Chapter 4* was provided by the Cornell Center for Materials Research with funding from the NSF MRSEC program (DMR-1120296), by the National Science Foundation (DMR-1254530), and by the Department of Energy Office of Science Graduate

Fellowship Program (DOE SCGF), made possible in part by the American Recovery and Reinvestment Act of 2009, administered by ORISE-ORAU under contract no. DE-AC05-06OR23100.

CHAPTER 5

POLARIZATION SPECTROSCOPY OF DEFECT-BASED SINGLE PHOTON SOURCES IN ZNO [2]

5.1 Chapter Abstract

Point defects in wide bandgap semiconductors are promising candidates for future applications that necessitate quantum light sources. Recently, defect-based single photon sources have been observed in ZnO that are very bright and remain photoactive from 4.5 K to room temperature. Despite several investigations, the structure and electronic states of these emitters remain unknown. In this work, we establish a procedure to distinguish a Z dipole from an XY dipole when studying quantum emitters that are randomly oriented. Our cryogenic and room temperature polarization measurements collectively establish that these unidentified ZnO quantum emitters have a Z dipole. We show that the associated absorption and emission dipoles are parallel within experimental uncertainty for all 32 individuals studied. Additionally, we apply group theory and find that assuming the defect symmetry belongs to a point group relevant to the ZnO wurtzite lattice, the ground and excited states are orbital singlets. These results are a significant step in identifying the structure and electronic states of defect-based single photon sources in ZnO.

5.2 Introduction

Isolated point defects in semiconductors exhibit quantum emission similar to single quantum dots [176], molecules [177], and trapped atoms and ions [178,179]. Therefore, point defects have been identified as nanoscale solid-state single photon sources (SPSs) with prospective applications in precision sensing and quantum communication [12,20,21,180,181]. While isolated defects in diamond including the nitrogen-vacancy (NV) center and the silicon-vacancy center have garnered the most attention [12,182–187], recent efforts to find viable defect-based SPSs in conventional semiconductors [20] have uncovered promising candidates in SiC [24–26,28] and ZnO [1,30,33,188,189]. Unlike diamond and SiC, ZnO has the advantage of a direct bandgap, thus offering the possibility of incorporating point defects with optoelectronic devices. Additionally, piezoelectricity in ZnO [190–192] introduces the prospect of directly utilizing lattice strain to control the quantum state of single defects [193]. These enticing bulk properties of ZnO are complemented by a wealth of established growth methods that would facilitate fabrication of photonic devices that exploit single-defect properties [68,121,166,194–197]. Furthermore, the quantum emission from ZnO point defects can be very bright (>100 kPhotons/s) with high polarization visibility [188], which is advantageous for applications requiring high bandwidth and/or polarized single photons on demand.

Despite these attractive properties, the progress in realizing quantum photonic devices based on this platform is hampered by the absence of a detailed understanding of the defect's structure and electronic states. In our previous study, we found significant defect-to-defect variability in the excited state lifetime ($1 - 13\ ns$), emission spectrum, fluorescence intensity, and photodynamics [1], which makes identification of the defect a challenge. Moreover, despite a wealth of prior research into ZnO defect fluorescence [68,85,87,101,105,175,198,107], there is yet no correspondence between the experimental observations of quantum emitters in ZnO and the theoretically predicted behavior of candidate defect structures. Establishing the identity of ZnO quantum emitters could enable creation of high-quality SPSs in a readily engineered material and provide the framework required to address the previously observed variability. A key step is to perform experiments that shed light on the properties of the defect's electronic ground and excited state.

In this work we establish a procedure for distinguishing a "Z dipole" from an "XY dipole" in isolated quantum emitters that have unknown orientation because they reside in randomly oriented nanocrystals. Then, in concert with group theoretic considerations, we determine which electronic states could be responsible for our experimental observations. Our approach involves measuring polarization properties of absorption and emission from many isolated defects with different orientations and comparing the results with the expectations for each dipole type. Our cryogenic and room

temperature measurements reveal that, unlike the NV center in diamond [199–202], the ZnO defects we study have a Z dipole as opposed to an XY dipole. Additionally, measurements of 21 defects in nanoparticles and 11 defects in sputtered films indicate that the associated absorption and emission dipoles are parallel within experimental uncertainty. The identification of a Z dipole is interpreted in the context of point group theory, enabling us to infer the allowed properties of the defect's ground and excited state wavefunctions for several symmetries common to the ZnO wurtzite lattice. These results constitute a significant step towards identifying the structure and electronic states of SPSs in ZnO.

5.3 Results and Discussion

Our polarization measurements may be understood in terms of absorption and emission dipoles. In general, point defects in crystals are associated with an axis of symmetry $\boldsymbol{D}$ (See Figure 5.1a) that corresponds to a distinct crystallographic direction. In such systems there are two electric dipole transitions relevant to polarization: π transitions and σ transitions. For π transitions the absorption dipole $\boldsymbol{\mu}_A$ is parallel to $\boldsymbol{D}$ and the absorption amplitude is proportional to $\cos^2\theta_A$, where θ_A is the angle between $\boldsymbol{\mu}_A$ and the incident electric field $\boldsymbol{E}_{exc}$. Analogously, the fluorescence intensity detected through a linear polarizer $\boldsymbol{P}_{coll}$ is proportional to $\cos^2\theta_E$, where θ_E is the angle between $\boldsymbol{P}_{coll}$ and the emission dipole $\boldsymbol{\mu}_E$ [8]. Here we define the z axis as the

axis of the objective and, for a particular defect, the x axis as being perpendicular to $\boldsymbol{D}$ and z (see Figure 5.1a). If the emission and absorption dipoles are parallel, then in spherical coordinates, with polar angle θ and azimuthal angle ϕ, we have $\boldsymbol{\mu}_A = \boldsymbol{\mu}_E = \boldsymbol{D} = \sin\theta\,\hat{\jmath} + \cos\theta\,\hat{k}$. In linear response, the fluorescence F_π detected when $\boldsymbol{E_{exc}} = \cos\phi_{exc}\,\hat{\imath} + \sin\phi_{exc}\,\hat{\jmath}$ and $\boldsymbol{P_{coll}} = \cos\phi_{coll}\,\hat{\imath} + \sin\phi_{coll}\,\hat{\jmath}$ is then proportional to

$$F_\pi \propto (\boldsymbol{D}\cdot\boldsymbol{E_{exc}})^2(\boldsymbol{D}\cdot\boldsymbol{P_{coll}})^2 = (\sin\theta\sin\phi_{exc})^2(\sin\theta\sin\phi_{coll})^2. \qquad (5.1)$$

Equation 5.1 assumes that both the collected and exciting light propagate in the z direction and thus ignores the effect of the high NA objective, which we account for below.

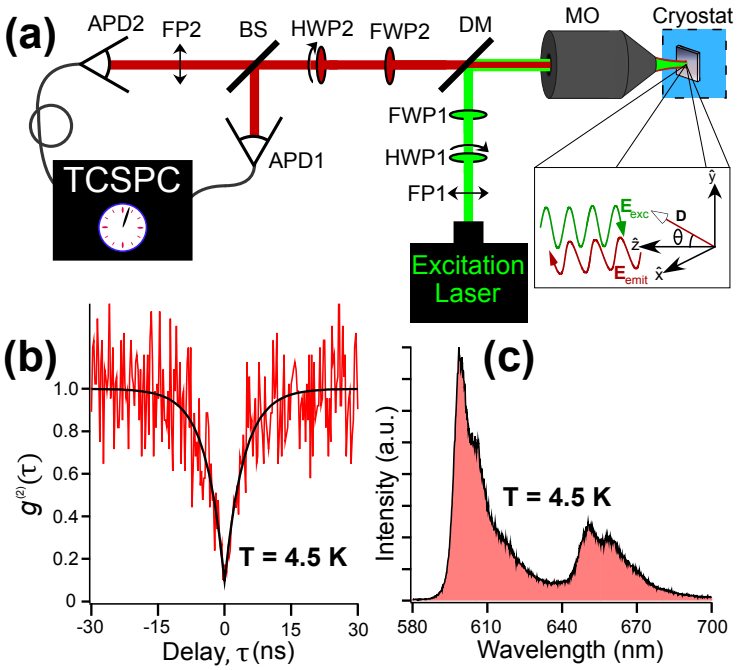

Figure 5.1: (a) Schematic of confocal microscope used to investigate polarization properties of single defects in ZnO. (b) An antibunching dip in $g^{(2)}(\tau)$ at $\tau = 0$ extending well below 0.5 verifies that a single ZnO defect is being probed. (c) The associated single-defect emission spectrum is phonon broadened and often exhibits two distinct spectral peaks. Because the antibunching dip in (b) extends to ~0.1, both spectral features in (c) emanate from the same emitter.

For σ transitions the absorption probability is proportional to $\sin^2\theta_A$, where θ_A is the angle between $\boldsymbol{D}$ and $\boldsymbol{E_{exc}}$. Similarly, the fluorescence intensity detected through a polarizer is proportional to $\sin^2\theta_E$, where θ_E is the angle between $\boldsymbol{D}$ and $\boldsymbol{P_{coll}}$ [8]. Equivalently, σ transitions may be described by two mutually perpendicular dipoles that span the plane normal to $\boldsymbol{D}$. The absorption and emission probabilities for each of these orthogonal dipoles are precisely those given above for π transitions [203]. Because σ transitions are associated with two dipoles, such transitions are referred to as having an "XY dipole". Conversely, π transitions are associated with a single dipole and are referred to as having a "Z dipole" [204].

To verify that our measurements reflect the optical properties of a single ZnO defect, and not an ensemble, we measure the two-photon correlation function, $g^{(2)}(\tau)$, of the collected photons. Figure 5.1b shows a $g^{(2)}(\tau)$ measurement with a pronounced antibunching dip at $\tau = 0$ delay. Because $g^{(2)}(0) \approx 0.1$ falls substantially below 0.5, the collected photons emanate from an isolated defect. The emission spectrum of this emitter (Figure 5.1c) is broad and is characterized by two distinct spectral peaks. A detailed analysis of photon correlation measurements and a discussion of single-defect emission spectra can be found in previous work [1].

Figure 5.2 is a representative set of polarization measurements made on a single defect in a ZnO nanoparticle. Monitoring the total fluorescence while rotating the polarization state of the exciting light ($\boldsymbol{E_{exc}}$) enables measurement of the absorption profile of a single defect (Figure 5.2a). After

fixing $\boldsymbol{E_{exc}}$ to maximize absorption, monitoring the fluorescence intensity detected through a polarization analyzer ($\boldsymbol{P_{coll}}$) enables us to measure the polarization state of the emitted photons (Figure 5.2b). Figures 5.2a and 2b both present a maximum at $\sim 90°$ and a minimum at $\sim 0°$, suggesting the absorption and emission dipoles are parallel. We also performed experiments where $\boldsymbol{E_{exc}}$ is parallel (Figure 5.2c) or perpendicular (Figure 5.2d) to $\boldsymbol{P_{coll}}$. All polarization plots can be fit using Equation 5.1 for a Z dipole, or the XY analog, with a constant background added. However, the background value that yields the best-fit substantially exceeds the background fluorescence measured experimentally. The discrepancy in the background level predicted using Equation 5.1 and that measured experimentally is explained by the loss of polarization visibility when imaging with a high NA objective. This is seen by inspecting Equation 5.1, which indicates that $F_\pi = 0$ whenever ϕ_{exc} or ϕ_{coll} is $0°$. We detect non-negligible fluorescence at $\phi_{exc} = 0°$ in Figure 5.2a and at $\phi_{coll} = 0°$ in Figure 5.2b. These photons that are not predicted by Equation 5.1 come from two sources: unpolarized background fluorescence and polarized defect fluorescence whose polarization is obfuscated by the high NA objective [205].

Following the method proposed by Fourkas [205], we developed an analytical model for Z and XY dipoles that accounts for our high NA objective. We simultaneously fit all plots in Figure 5.2 using our model by introducing the 3-dimensional defect orientation and collection path extinction ratio as free parameters. The nearly negligible background fluorescence, which is difficult

to precisely measure, is not included as a free parameter. The resulting best-fits assuming a Z and XY dipole are shown as the solid and dashed lines in Figure 5.2, respectively. The Z dipole best-fit occurs for a collection path extinction ratio of 20, which is consistent with previous calibration measurements (see *Section 5.5*). Conversely, the XY dipole model best-fit occurs for an unphysical collection path extinction ratio of $\sim 10^8$. Moreover, while the Z dipole model fits all plots adequately, the XY dipole model fails to fit Figure 5.2d as well as the Z dipole model does.

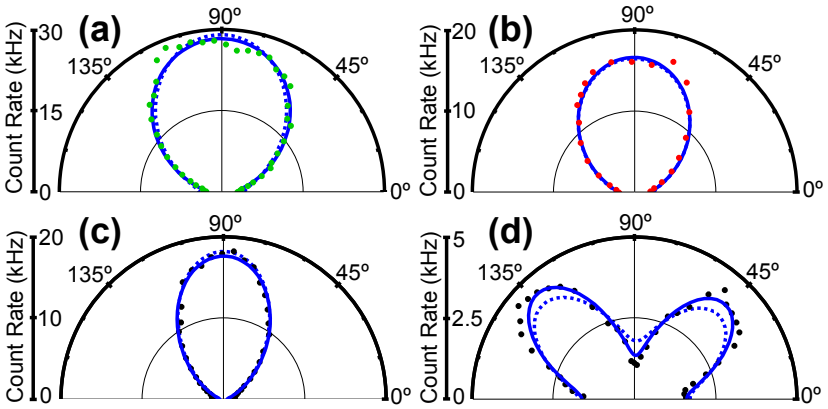

Figure 5.2: Representative set of polarization measurements acquired for single defects in this work. The absorption (a) and emission (b) graphs are aligned, suggesting the absorption and emission dipoles are parallel. The smaller count rate in (b) compared with (a) results from differences in collection efficiency for the two paths. Plots (c) and (d) corresponds to the polarization of the exciting light and the collected light being parallel and perpendicular, respectively. In each plot, the best-fits assuming a Z and XY dipole are represented by solid and dashed lines, respectively. The polarization basis in these plots has been defined so that the excitation maximum points along the y-axis.

Figure 5.2 makes a strong case for SPSs in ZnO having a Z dipole but does not eliminate the XY dipole possibility. To strengthen the Z dipole argument, we acquired polarization measurements for 21 defects in randomly

oriented nanoparticles, which allowed us to sample various orientations of the defect symmetry axis $\boldsymbol{D}(\theta, \phi)$. Every such measurement was qualitatively similar to those shown in Figure 5.2.

Here we explain why the plots in Figure 5.2, that are representative of all investigated defects, support a Z dipole. Because single photon counting experiments are shot noise limited, dim emitters can be difficult to identify over the background fluorescence. Therefore, the defect orientations that produce the greatest photon yield are precisely those that are most likely to be identified for study. Figure 5.3 displays what our Z and XY dipole models predict for the perpendicular measurement of Figure 5.2d for defect orientations $\{\theta, \phi\} = \{0°, 0°\}$, $\{30°, 0°\}$, $\{60°, 0°\}$, and $\{90°, 0°\}$. Each curve assumes the same intrinsic oscillator strength and is therefore proportional to the fluorescence we should observe experimentally. In Figure 5.3a, which corresponds to a Z dipole, the curves for $60° \leq \theta \leq 90°$ best resemble the representative plot of Figure 5.2d. This range of θ also corresponds to the brightest defect orientations and is therefore the most likely set of orientations to identify experimentally. In Figure 5.3b, which corresponds to an XY dipole, the plots for $60° \leq \theta \leq 90°$ are also the most similar to the experimental plot of Figure 5.2d. However, for an XY dipole, this range of θ corresponds to the dimmest defect orientations and is therefore the least likely set of orientations to be encountered experimentally. Thus only in the Z dipole model do the defect orientations that we are most likely to encounter experimentally match our observations. Analogous θ-dependent plots for the remaining

measurements of Figures 5.2a, b, and c similarly support a Z dipole over an XY dipole.

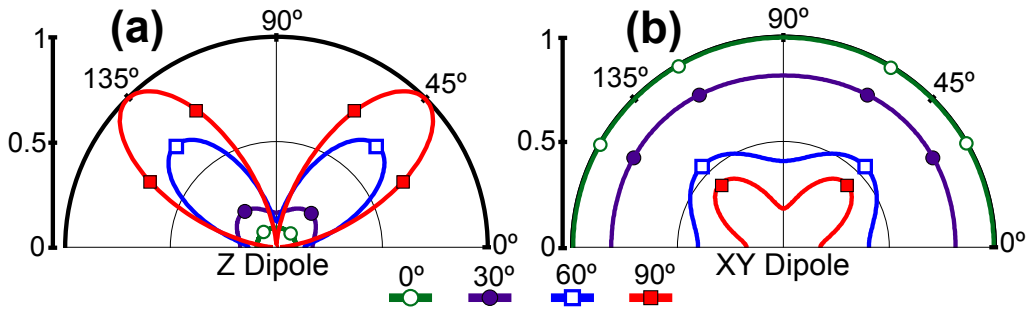

Figure 5.3: Theoretical plots for the case when the polarization of the exciting light and collected light are perpendicular for a Z dipole (a) and an XY dipole (b). Each graph has four curves that correspond to various symmetry axis orientations.

As a final verification that we study a Z dipole, we examine the distribution of polarization visibilities. The visibility is defined as $V = (I_{max} - I_{min})/(I_{max} + I_{min})$, where I_{max} and I_{min} are the maximum and minimum fluorescence intensities. The distribution of excitation and emission visibilities from defects in randomly oriented nanoparticles is shown in Figures 5.4a and b, respectively. The excitation visibilities range from 0.50 to 0.91 and have an average value of 0.78 whereas the emission visibilities range from 0.49 to 0.94 and have an average value of 0.79. Superimposed on each visibility distribution is a best-fit produced from our Z (solid line) and XY (dashed line) dipole models. These best-fits employ the same binning width as the data and incorporate a background parameter that left-shifts the theoretical distribution. The Z dipole model better fits the data than the XY model and also predicts a background that better matches that seen experimentally.

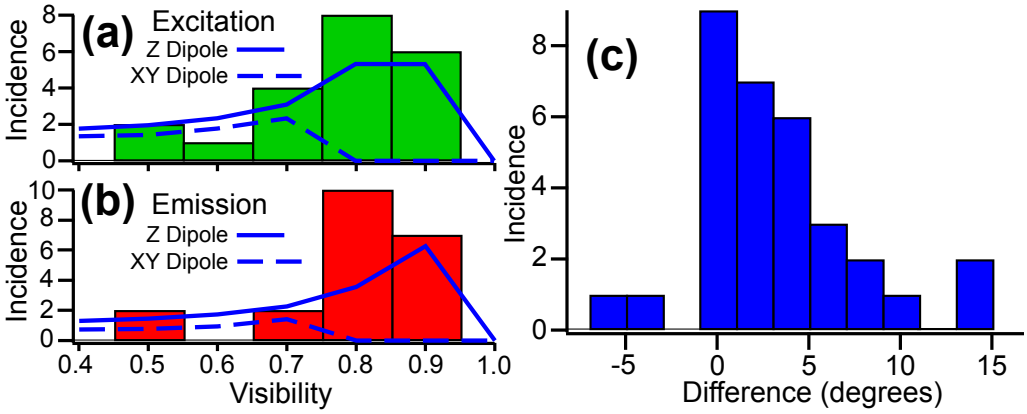

Figure 5.4: Histogram of the excitation visibility (a), emission visibility (b), and angular difference between the absorption and emission maxima (c). Superposed in (a) and (b) are best-fits resulting from our Z (solid) and XY (dashed) dipole models.

Figures 5.2-5.4 establish that the investigated defects possess a Z dipole. Typically the associated absorption and emission dipoles for point defects are nearly parallel [184,204,206,207]. An earlier report [188] found a large ($\sim 80°$) offset between the absorption and emission maxima of a quantum emitter in ZnO. Figure 5.4c shows our distribution of misalignment between the absorption and emission maxima for all defects investigated. The distribution is concentrated near $0°$ and the average misalignment is $3.2°$. We interpret this small misalignment as a systematic error in the average polarization of the collection path that results from variations in path retardance for collected photons whose wavelength differs from our 630 nm calibration wavelength. Consequently we find that the absorption and emission dipoles are parallel within experimental uncertainty.

Once a defect's dipole type (Z or XY) is known, group theoretic considerations can shed light on the ground and excited state wavefunction

properties [208]. Every point defect belongs to a point group containing the symmetry operations that leave its Hamiltonian invariant. For the ZnO wurtzite lattice, the available defect symmetry operations are the identity ($\hat{E}$), a $120°$ rotation about the c-axis ($\hat{C}_3$), and a reflection about a vertical plane ($\hat{\sigma}_v$). These operations yield three nontrivial point groups: $\boldsymbol{C_{3v}} = \{\hat{C}_3, \hat{\sigma}_v, \hat{E}\}$, $\boldsymbol{C_s} = \{\hat{\sigma}_v, \hat{E}\}$, and $\boldsymbol{C_3} = \{\hat{C}_3, \hat{E}\}$. Table 5.1 lists the allowed transitions for these point groups for each dipole type (see *Section 5.6*). If the point group of the defects we study is among these, then both the ground and excited state wavefunctions must be orbital singlets and transform as the A_1 or A_2 irreducible representation. Previous observations of photon bunching [1,30,188] revealed that SPSs in ZnO possess a metastable shelving state. Of the point groups in Table 5.1, only $\boldsymbol{C_{3v}}$ has a forbidden transition ($A_1 \leftrightarrow A_2$) that becomes a candidate for this metastable to ground state transition. Note that an orbital singlet may possess spin degrees of freedom, as is the case for the orbital singlet, spin triplet ground state of the NV center.

	$\boldsymbol{C_{3v}} = \{\hat{C}_3, \hat{\sigma}_v, \hat{E}\}$	$\boldsymbol{C_s} = \{\hat{\sigma}_v, \hat{E}\}$	$\boldsymbol{C_3} = \{\hat{C}_3, \hat{E}\}$
Z Dipole	$A_1 \leftrightarrow A_1$, $A_2 \leftrightarrow A_2$	$A_1 \leftrightarrow A_2$	$A_1 \leftrightarrow A_1$
XY Dipole	$A_1 \leftrightarrow E$, $A_2 \leftrightarrow E$	$A_1 \leftrightarrow A_1$, $A_2 \leftrightarrow A_2$	$A_1 \leftrightarrow E$

Table 5.1: Summary of allowed transitions for Z and XY dipoles for point groups relevant to ZnO. States labeled by "A" are orbital singlets and states labeled by "E" are orbital doublets. The "1" subscript indicates the state is totally symmetric and the "2" subscript indicates the state is antisymmetric with respect to $\hat{\sigma}_v$. Because transitions are symmetric, the ground and excited states in a given transition may be interchanged.

We note that our study does not rule out the unlikely possibility that the investigated defects belong to a point group not listed in Table 5.1. In such a scenario the defect would not stem solely from an impurity, vacancy, or a small combination of these. While a Z dipole is never of the $A \leftrightarrow E$ variety, it can correspond to $E \leftrightarrow E$ transitions in some high symmetry cases such as the tetragonal point group D_{4h}. Such high symmetry point groups are unlikely to be relevant for bulk or surface defects [209,210] in ZnO and therefore, most probable scenario is a transition between orbital singlets. Future polarization spectroscopy experiments that probe these defects in single crystal ZnO could eliminate these possibilities and identify the crystallographic direction of the defect's symmetry axis.

5.4 Conclusion

We investigated polarization properties of defect-based SPSs in ZnO to gain insight into their electronic states and their structural origin by discerning whether they possess a Z or XY dipole. Because particular orientations of an XY dipole resemble a Z dipole, and vice versa, experiments intended to identify a SPS's dipole type have previously been conducted in ordered crystals where the allowed orientations of the emitter are known [184,206,211,212]. Here we demonstrate that an alternative but definitive approach is to sample emitters that are randomly oriented and compare the distribution to the statistical expectation for each dipole type.

Though we apply this approach to point defects in randomly oriented nanoparticles, it could also be useful for establishing the dipole type of unknown quantum emitters like single molecules in amorphous media where the orientation is not *a priori* known. For each single defect investigated in this work, either a Z or XY dipole model could replicate the observed behavior. However, the XY model fails at predicting the distribution of observed polarization plots and visibilities, while the Z model satisfactorily matched these distributions. Consequently, our measurements and analysis indicate that the investigated defects have a Z dipole.

Across the 32 defects investigated in nanoparticles and sputtered films, we find that the absorption and emission dipoles are parallel within experimental uncertainty. This indicates that the symmetry axis of the ground state is identical to that of the excited state within the precision of our measurement. Though the defect's absolute symmetry remains unknown, we have applied group theoretic considerations to all crystallographic point groups. We find that if the defect belongs to a point group relevant to ZnO then the ground and excited states are orbital singlets. Establishing that the investigated ZnO defects possess a Z dipole and identifying their most probable electronic states constitutes an important step in pinpointing their structural origin.

5.5 Experimental

Figure 5.1a depicts the house-built confocal microscope used to perform polarization spectroscopy of isolated defects in randomly oriented ZnO nanoparticles and $\langle 001 \rangle$ oriented sputtered ZnO films (see *Section 5.6* for sample details). For absorption measurements, a fixed polarizer (FP1) followed by a rotatable half wave plate (HWP1) was used to produce an arbitrary linear polarization state of the exciting light. The exciting light is directed to a high NA (0.7) microscope objective (MO) by a dichroic mirror (DM). Between HWP1 and the MO, the exciting light inherits some ellipticity from retardances introduced by the excitation path. Using a variable compensator, we measure the net excitation path retardance at 532 nm to be ~0.21 waves. We correct for this using a fixed wave plate (FWP1) selected to give an appropriate correcting retardance. Though all data presented here are for defects excited with 532 nm light, we performed identical measurements using 473 nm light that was likewise compensated for path retardances, and found consistent results (see *Section 5.6*). Additionally, we note that our measurements were performed at temperatures ranging from 4.5 K to room temperature and we see consistent polarization behavior across the defects studied for all operating temperatures. We also detect no rotation of a single defect's dipole orientation as temperature is changed (see *Section 5.6*).

The exciting light may be scanned over the sample in search of isolated defects. A defect with symmetry axis $\boldsymbol{D}$ may absorb the exciting light and emit

polarized single photons into the focal cone of the objective. These collected photons range from 560 - 720 nm and each inherits a wavelength dependent retardance in the collection path. At 630 nm the collection path retardance is ~0.28 waves. This is compensated by FWP2 and the polarization state may be rotated by achromatic HWP2. Each collected photon encounters a polarization insensitive 50/50 beam splitter (BS) and is directed towards an avalanche photodiode (APD) sensitive to single photons. Photons directed towards APD1 may be detected independent of their polarization whereas photons directed towards APD2 pass through FP2 with a probability determined by their polarization state. Time correlated single photon counting (TCSPC) enables measurement of $g^{(2)}(\tau)$ to verify a single defect is being probed (Figure 5.1b). The polarization state of the exciting light was calibrated by measuring 532 nm light with a polarization analyzer placed at the objective for various orientations of HWP1. The polarization state of emitted light was calibrated in a similar manner with a 630 nm source for various orientations of HWP2. Across all polarization states, the polarization extinction ratio of the emitted light is greater than 10, whereas the extinction ratio of the exciting light exceeds 1000. The diminished extinction ratio for collected light is because the single-defect emission spectrum (Figure 5.1c) extends over a broad range (~300 meV) compared to the monochromatic exciting light and exhibits defect-to-defect variation [1].

5.6 Supplementary Information

5.6.1 Sample Details

The samples consist of randomly oriented ZnO nanoparticles and $\langle 001 \rangle$ oriented sputtered ZnO films. The nanoparticles were suspended in methanol prior to being drop-cast onto a thermally oxidized silicon substrate and are commercially available from Sigma-Aldrich as product number 677450. The sputtered films were also deposited on thermally oxidized silicon and the growth parameters have been described previously [1]. All samples were annealed in air at $500° \, C$ for 30 minutes and then passivated with the e-beam resist hydrogen silsesquioxane (HSQ). The HSQ layer was motivated by a previous report [188] and phenomenologically serves to increase the photo-stability of SPSs. A control sample containing HSQ, but not ZnO, verified that the investigated SPSs originate from ZnO. We note that the ambient humidity was not monitored during sample preparation. All data was obtained for samples mounted in a Janis ST-500 cryostat capable of cooling to 4.5 K. We detect no variation in polarization properties from 4.5 K to room temperature.

5.6.2 Excitation Using 473 nm Light

The absorption band of isolated defects is often broadened by phonon coupling. In addition to using 532 nm (green) light, we also investigated using 473 nm (blue) light for excitation. We detected no difference in defect polarization or emission properties when using blue light in lieu of green light.

We did, however, observe an increase in the background fluorescence when using blue light compared to green light.

Figure 5.5 shows $g^{(2)}(\tau)$ for a ZnO defect measured using 532 nm (bottom) and 473 nm (top) light for excitation. In the bottom plot, $g^{(2)}(\tau = 0) < 0.5$ verifies that green light selectively excites a single ZnO defect. The $g^{(2)}(0)$ level for green light is consistent with the signal to background ratio estimated for this defect. When the same defect is excited solely with blue light, $g^{(2)}(0)$ rises to a level consistent with the enhanced background fluorescence produced by the blue light compared to the green light. In addition to antibunching [$g^{(2)}(0) < g^{(2)}(\infty)$], both curves exhibit photon bunching [$g^{(2)}(|\tau| \sim 10\ ns) > g^{(2)}(\infty)$], establishing that this particular defect has a metastable shelving state. We note that this defect was not used in our polarization statistics and that Figure 5.5 serves to illustrate bunching behavior and to compare green and blue excitation.

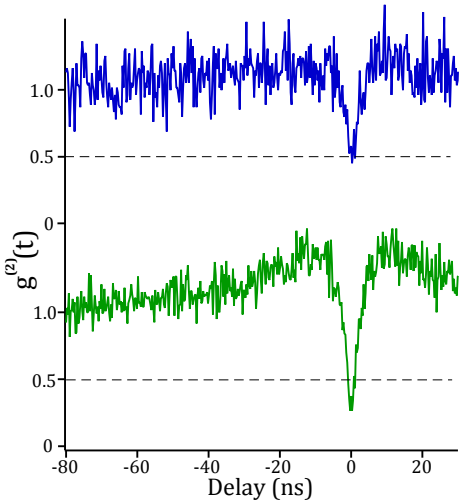

Figure 5.5: Measurement of $g^{(2)}(\tau)$ using blue (top) and green (bottom) light for excitation.

Figure 5.6 compares the normalized emission spectrum of a single defect in ZnO excited with blue and green light. This emission spectrum is from the same defect that produced Figure 5.1b and Figure 5.1c in the main text. Note that this defect did not exhibit bunching behavior and is a different defect than the defect that produced Figure 5.5. The two spectra are nearly indistinguishable, suggesting that both blue and green light excite the defect into the same excited electronic state.

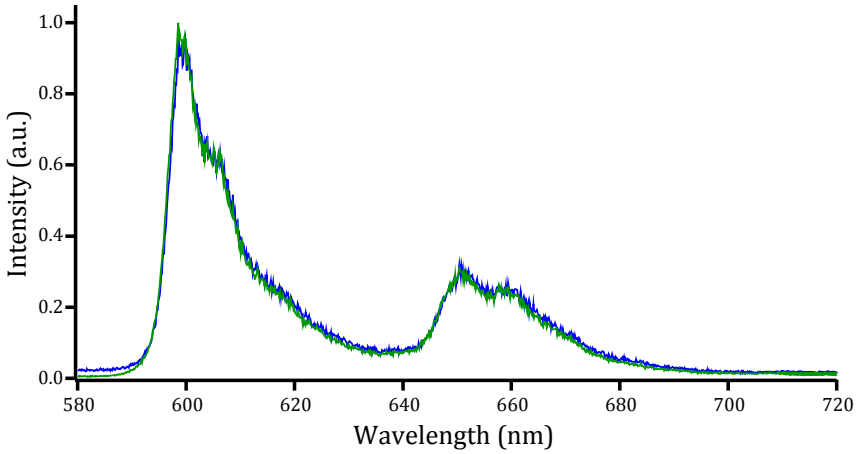

Figure 5.6: Normalized emission spectrum of a single ZnO defect excited using blue and green light. The emission spectrum is not altered by the wavelength of the exciting light.

Figure 5.7 displays a set of single-defect polarization measurements made using blue and green light for excitation. The polarization basis has been defined so that the maximum of the green absorption curve (green triangles) occurs at $90°$. The maximum of the blue absorption curve (blue diamonds) is also at $\sim 90°$, indicating that the absorption dipoles for both blue and green light are identical. Additionally, the blue absorption visibility is less than the green absorption visibility because of the relative increase in

unpolarized background signal for blue excitation compared to green excitation. Lastly, the defect emission polarization (red circles) also presents a maximum at ~90° because the absorption and emission dipoles are parallel.

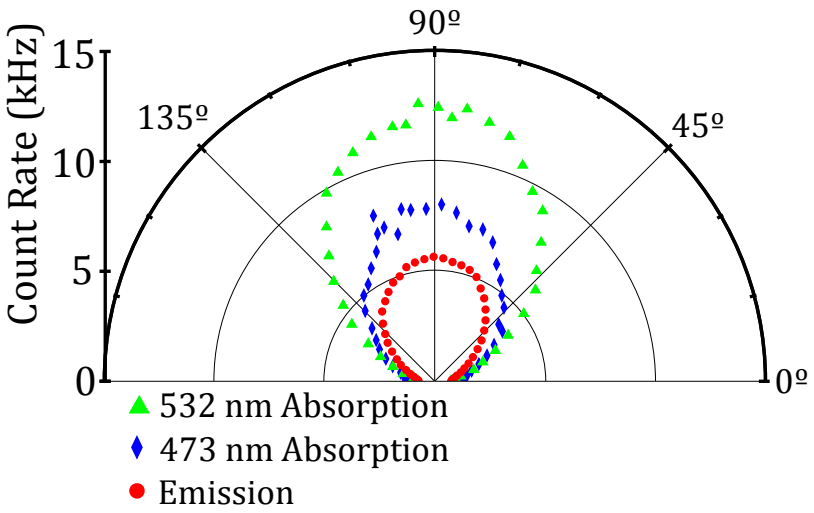

Figure 5.7: Set of polarization measurements made on a single defect using blue and green light for excitation.

5.6.3 Temperature Dependence

We measured the orientation of a single defect's absorption dipole at several temperatures between 10 and 90 K. Figure 5.8 shows the result of this experiment. No temperature dependence is evident, and the maximum variation is 1.7°, which is within our experimental uncertainty, suggesting the defect's dipole orientation remains stable as temperature is varied.

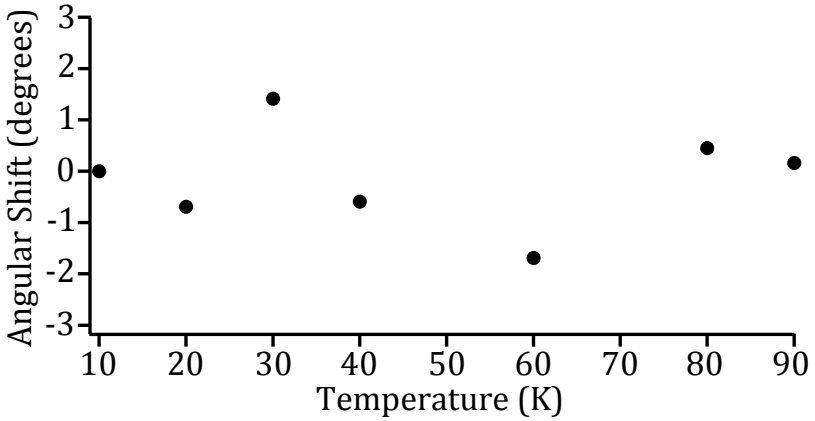

Figure 5.8: Angular shift of the absorption dipole of a single defect from 10 to 90 K. No temperature dependence is evident.

5.6.4 Point Group Theory

If a defect's point group is known then valuable information about its eigenstates and polarization selection rules may be extracted without computation. A thorough overview of group theory and its applicability to physics is available in Dresselhaus [208]. Here we quickly illustrate how we applied point group theory to our findings by considering the point group $\boldsymbol{C_{3v}}$.

Table 5.2 is the $\boldsymbol{C_{3v}}$ character table [208]. The leftmost column of Table 5.2 lists the irreducible representations (A_1, A_2, and E) associated with $\boldsymbol{C_{3v}}$. There is a one-to-one correspondence between the irreducible representations of a defect's point group and the single electron eigenstates of its Hamiltonian. The dimensionality of the representation corresponds to the eigenstate's degeneracy and the eigenstate possesses the transformation properties of its corresponding irreducible representation. The A_1 and A_2 representations are

one-dimensional whereas the E representation is two-dimensional. The "1" subscript indicates the state is totally symmetric under all operations and the "2" subscript indicates the state is antisymmetric under $\hat{\sigma}_v$. Consequently, defects with $\boldsymbol{C_{3v}}$ symmetry have two non-degenerate states and one doubly degenerate state. Spin properties arise when these single electron states are populated with electrons in accordance with the Pauli exclusion principle.

The last column of Table 5.2 indicates how the linear operators x, y, and z transform. Thus for $\boldsymbol{C_{3v}}$, the z operator transforms as the totally symmetric representation A_1 whereas x and y jointly transform as the two-dimensional E representation. Note that, contrary to our coordinate system used previously, the z direction here is aligned parallel to the defect's symmetry axis rather than parallel the axis of the microscope objective.

	$\hat{E}$	$2\hat{C}_3$	$3\hat{\sigma}_v$	Linear
A_1	1	1	1	z
A_2	1	1	-1	
E	2	-1	0	x,y

Table 5.2: Character table for the point group $\boldsymbol{C_{3v}}$.

In general, a transition between initial state $|\psi_i\rangle$ and final state $|\psi_f\rangle$ is allowed if $\langle\psi_f|\hat{O}|\psi_i\rangle \neq 0$, where $\hat{O}$ is a perturbation intended to couple $|\psi_i\rangle$ and $|\psi_f\rangle$. In the case of an electric dipole transition from the ground to excited state, $\hat{O} = \boldsymbol{\mu} \cdot \boldsymbol{E}$, where $\boldsymbol{\mu}$ is the absorption dipole and $\boldsymbol{E}$ is the electric field of the exciting light. Consequently, in the basis of the defect, light polarized along (x, y, z) may be absorbed and excite the defect if $\langle\psi_f|(x, y, z)|\psi_i\rangle \neq 0$. Group theory may be utilized to quickly determine which of these transition

probabilities necessarily vanish. If the ground state $|\psi_i\rangle$, excited state $|\psi_f\rangle$, and perturbation $\hat{O}$ transform as the irreducible representations Γ_i, Γ_f, and Γ_O, respectively, then a transition is permitted by group theory if and only if the direct product $\Gamma_i \otimes \Gamma_O \otimes \Gamma_f$ contains the totally symmetric representation.

Table 5.3 is a direct product table for $\boldsymbol{C_{3v}}$ and is useful for determining polarization selection rules of a point defect with $\boldsymbol{C_{3v}}$ symmetry. For example, z-polarized light may drive $A_1 \leftrightarrow A_1$ transitions because $A_1 \otimes \Gamma_z \otimes A_1 = A_1 \otimes A_1 \otimes A_1 = A_1 \supset A_1$. However, z-polarized light cannot drive $A_1 \leftrightarrow A_2$ transitions because $A_1 \otimes A_1 \otimes A_2 = A_2 \not\supset A_1$. Table 5.4 lists the transitions permitted by group theory for x, y, and z polarized light and can be used to determine the allowed transitions for a Z and XY dipole. To illustrate, a Z dipole is associated with $A_1 \leftrightarrow A_1$ and $A_2 \leftrightarrow A_2$ transitions because only *one* polarization state drives these transitions. Moreover, an XY dipole is associated with $A_1 \leftrightarrow E$ and $A_2 \leftrightarrow E$ transitions because precisely *two* orthogonal polarization states drive these transitions. Transitions of the $E \leftrightarrow E$ variety are permitted for x, y, and z polarized light and would therefore be associated with an XYZ dipole.

$\otimes$	A_1	A_2	E
A_1	A_1	A_2	E
A_2	A_2	A_1	E
E	E	E	$A_1 + A_2 + E$

Table 5.3: Product table for the irreducible representations associated with the point group C_{3v}.

Polarization	Allowed Transitions
x , y	$A_1 \leftrightarrow E, A_2 \leftrightarrow E, E \leftrightarrow E$
z	$A_1 \leftrightarrow A_1, A_2 \leftrightarrow A_2, E \leftrightarrow E$

Table 5.4: List of transitions that are permitted by group theory for light polarized along the x, y, and z directions.

5.7 Acknowledgements

Research support for *Chapter 5* was provided by the National Science Foundation (DMR-1254530). We acknowledge use of the Cornell NanoScale Facility, a member of the National Nanotechnology Coordinated Infrastructure (NNCI), which is supported by the National Science Foundation (Grant ECCS-15420819). Additionally, we acknowledge the Cornell Center for Materials Research Shared Facilities, which are supported through the NSF MRSEC program (DMR-1120296).

CHAPTER 6

TEMPERATURE DEPENDENCE OF WAVELENGTH SELECTABLE ZERO-PHONON EMISSION FROM SINGLE DEFECTS IN HEXAGONAL BORON NITRIDE [3]

6.1 Chapter Abstract

We investigate the distribution and temperature-dependent optical properties of sharp, zero-phonon emission from defect-based single photon sources in multilayer hexagonal boron nitride (h-BN) flakes. We observe sharp emission lines from optically active defects distributed across an energy range that exceeds 500 meV. Spectrally-resolved photon-correlation measurements verify single photon emission, even when multiple emission lines are simultaneously excited within the same h-BN flake. We also present a detailed study of the temperature-dependent linewidth, spectral energy shift, and intensity for two different zero-phonon lines centered at 575 nm and 682 nm, which reveals a nearly identical temperature dependence despite a large difference in transition energy. Our temperature-dependent results are well described by a lattice vibration model that considers piezoelectric coupling to in-plane phonons. Finally, polarization spectroscopy measurements suggest that whereas the 575 nm emission line is directly excited by 532 nm excitation, the 682 nm line is excited indirectly.

6.2 Main Text

Two-dimensional materials and associated layered solids including graphene, hexagonal boron nitride (h-BN), and transition metal dichalcogenides (TMDs) possess attractive mechanical [213,214], electrical [215,216], thermal [217,218], chemical [219,220], and optical [221,222] properties. Unlike graphene and TMDs, h-BN is a wide bandgap (~6 eV) electrical insulator, making it a key component in many van der Waals heterostructures [223–225]. This feature also makes h-BN an ideal host for optically active defect centers [1,20].

Isolated color centers in wide bandgap semiconductors are single photon sources with potential applications in quantum optics, precision sensing, and quantum information technologies [20,118,18,17,226]. Recently, ultrabright and polarized single photon emission from isolated defects in monolayer and multilayer h-BN has been reported [39,40,227]. These observations add h-BN to the growing collection of wide bandgap materials (Diamond [12,182,228,21,229–232,186], SiC [122,123,24–26,28,233], and ZnO [1,2,30–33]) that host defect-based room temperature single photon sources. Whereas isolated defects in monolayer h-BN show broad spectral emission and unreliable photostability in our measurements (see *Section 6.4*), single defects in multilayer h-BN appear to be absolutely photostable and exhibit sharp zero-phonon lines with a small Huang-Rhys factor [167,234,235]. These properties potentially make multilayer h-BN defects attractive sources

of indistinguishable single photons. At present, defect centers in both monolayer and multilayer h-BN remain poorly understood, which motivates investigation of the properties of defects within each material.

In this work we study the temperature dependence of spectrally narrow zero-phonon lines (ZPLs) from point defects in multilayer h-BN. First, we characterize the distribution and intensity of sharp spectral emission in the range ~570-740 nm at cryogenic temperatures. This survey reveals a forest of sharp spectral features across a wide range of energy. Spectrally-resolved photon-correlation measurements enable us to unambiguously identify emission lines that correspond to single photon emission from individual defects. For two of the identified lines (575 nm and 682 nm) we investigate the temperature-dependent linewidth, line shift, excited state lifetime, and intensity. Despite an energy difference of over 300 meV, both lines exhibit similar temperature-dependent line broadening and shifting. We propose a phonon-mediated mechanism that treats each emission line as a ZPL to explain the broadening we observe. Finally, we present polarization spectroscopy results that suggest while the 575 nm ZPL is excited directly through defect absorption of the 532 nm exciting light, the 682 nm ZPL is excited indirectly though cross relaxation.

We used a house-built confocal microscope to selectively excite deep defect levels in h-BN flakes (See *Section 6.3* for sample information and *Section 6.4* for microscope details). Flakes possessing optically active defects produced bright fluorescence (>400 kPhotons/s) when excited with 532 nm

light. Figure 6.1a-c displays representative fluorescence spectra of three distinct h-BN flakes at 4.5 K. These spectra reveal a multitude of sharp emission lines, some of which may correspond to the ZPL of an individual defect. In Figure 6.1d and e we display the two-photon correlation function, $g^{(2)}(\tau)$, measured on the h-BN flakes that produced the spectra in Figure 6.1a and b, respectively. For these measurements collection was limited to the shaded spectral regions using optical filters. The black curve in each plot is a best-fit to the data. The fits indicate that the antibunching dips at $\tau = 0$ in Figure 6.1d and e extend to 0.24 and 0.44, respectively (See *Section 6.4* for the effect of the instrument response function). Consequently, the sharp spectral features at 575 nm and 682 nm marked by arrows can be identified as single photon emission.

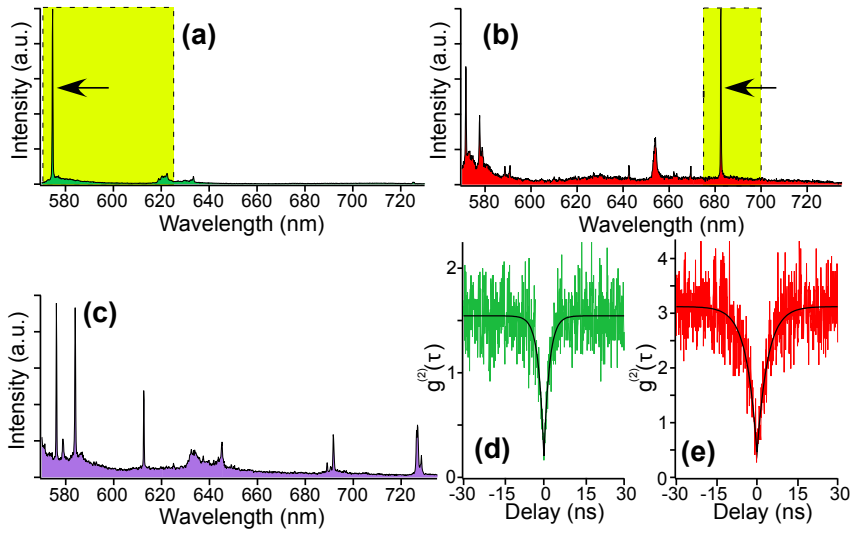

Figure 6.1: (a-c) Emission spectra from three distinct h-BN flakes revealing multiple sharp emission lines. (d) and (e) are $g^{(2)}(\tau)$ measurement of the spectra in (a) and (b), respectively, where collection was limited to the shaded regions. The antibunching dips at $\tau = 0$ verify single photon emission from the sharp zero-phonon lines in (a) and (b) marked by the arrows.

Next we consider if the arrowed emission lines in Figure 6.1a-b are zero-phonon transitions or if they are mediated by the emission of high-energy phonons. The lineshape of a phonon sideband depends on the overlap between the defect's excited-state wavefunction and all allowed vibronic modes of the defect's orbital ground state wavefunction. Therefore, the phonon density of states (DOS) influences the phonon sideband emission, such that a sharp feature in the DOS could conceivably allow for single photon emission into a sharp spectral line that is not a ZPL (See *Section 6.4*). However, we rule out this possibility for two reasons. First, the arrowed emission lines in Figure 6.1a-b are each >10x narrower than the sharpest feature in the bulk h-BN phonon (DOS), which occurs at ~165 meV [236], and thus the narrow linewidths we observe at low temperature are incompatible with phonon-sideband emission. In fact, we do observe a broad, low intensity feature in Fig. 6.1a at 623 nm that is shifted ~165 meV from the 575 nm line, which we attribute as an optical-phonon sideband. Second, as we describe in detail later, the amplitude and linewidth of these emission lines has a strong temperature dependence, which is inconsistent with emission mediated by high-energy phonons because there is no strong temperature dependence to the phonon DOS. Thus we conclude that these sharp emission lines result from zero-phonon and, as we will show later, low energy acoustic phonon processes.

The energy of a ZPL is determined primarily by the Hamiltonian describing the orbital component of the defect wavefunction. However, the

orbital excited-to-ground-state splitting may be shifted by defect-to-defect variations in the local environment such as strain or electric field from trapped charges. To investigate this variation in multilayer h-BN, we collected emission spectra similar to those shown in Figure 6.1a-c from 90 distinct h-BN flakes at 4.5 K. Because the sharpest feature in the bulk h-BN phonon DOS has a full width at half maximum (FWHM) of ~5 meV [236], we restricted our attention to spectral features with a FWHM of less than 4 meV (See *Section 6.4* for a discussion of assumptions), the majority of which are narrower than 2 meV. We recorded the peak position (E_0) and relative intensity (I_R) of each feature, where I_R is the ratio of the line intensity at E_0 to that of the background (see *Section 6.4*). Figure 6.2a is a scatter plot relating E_0 to I_R for the 340 lines we identified. We only include emission lines with $I_R > 1$ because only these lines may in principle produce $g^{(2)}(0) < 0.5$. Emission lines in h-BN can be bright ($I_R \approx 100$), even at photon energies far removed from the excitation source energy.

Figure 6.2b is a histogram of the positions of the emission lines in Figure 6.2a. A previous investigation [39] reported a ZPL with energy ~1.99 eV that was tentatively attributed to an anti-site nitrogen vacancy N_BV_N. The distribution in Figure 6.2b is statistically broader than a normal distribution (see *Section 6.4*), providing evidence that the distribution of emission lines results both from strain-induced inhomogeneous broadening of this 1.99 eV ZPL and from additional defect species [40]. Theoretical investigations of defect emission energies may place bounds on such broadening and aid in

identifying the defects under study [237]. Though we did not measure $g^{(2)}(\tau)$ for every narrow emission line, the green hexagons above the x-axis correspond to sharp emission lines that we have spectrally isolated with optical filters and measured $g^{(2)}(0) < 0.5$. Figure 6.2 suggests that h-BN flakes host multiple species of spectrally narrow, bright, and photostable defects with emission energies that are selectable over a broad range.

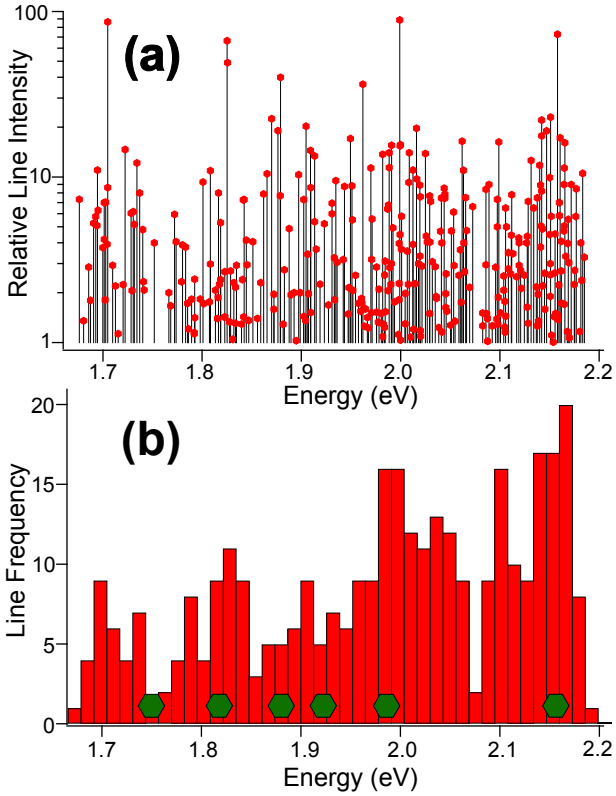

Figure 6.2: (a) Scatter plot relating energy and relative intensity of sharp emission lines from 90 distinct h-BN flakes. Individual emission lines may be bright and are densely distributed across a broad energy range. (b) The histogram of line positions from (a). The green hexagons along the x-axis denote emission lines for which we measured $g^{(2)}(0) < 0.5$ using spectrally-resolved photon correlation measurements.

The distribution of emission lines in Figure 6.2 suggest that the defects couple to local lattice strain. To better understand defect-lattice interactions,

and specifically dynamical (phonon-mediated) interactions, we investigated the temperature dependence of the two ZPLs located at 575 nm (2.16 eV) and 682 nm (1.82 eV), shown in Figure 6.1a-b. For each temperature investigated, we fit the emission spectrum to a linear combination of a background and a Lorentzian lineshape (see *Section 6.4*),

$$L(E) \propto \frac{1}{(E-E_{ZPL})^2+(\Gamma/2)^2}, \tag{6.1}$$

where E_{ZPL} is the ZPL energy, Γ is the FWHM, and $L(E)dE$ is proportional to the number of photons emitted in the energy range $(E, E+dE)$. Our results for $\Delta E_{ZPL}(T) = E_{ZPL}(T) - E_{ZPL}(4.5\ K)$ and $\Gamma(T)$ are plotted in Figure 6.3a and b, respectively. We note from Figure 6.3a that both ZPLs red shift with increasing temperature in a similar manner, despite having transition energies that differ by ~340 meV. A temperature-dependent redshift of an intradefect optical transition is common in semiconductors due to the increase in bulk lattice constant with increasing temperature. The solid line is a guide to the eye with a T^3 trend. In Figure 6.3b the FWHM broadens with temperature and is spectrometer-resolution limited below ~15 K. The inset, which is the same data plotted on a log scale, indicates a nearly exponential temperature dependence. The trends in Figure 6.3a-b differ from those reported in other defect systems [228,230,233] and from theoretical expectations for defects in a 3D solid [167]. To better understand our observations we consider both lifetime- and phonon-mediated broadening mechanisms below.

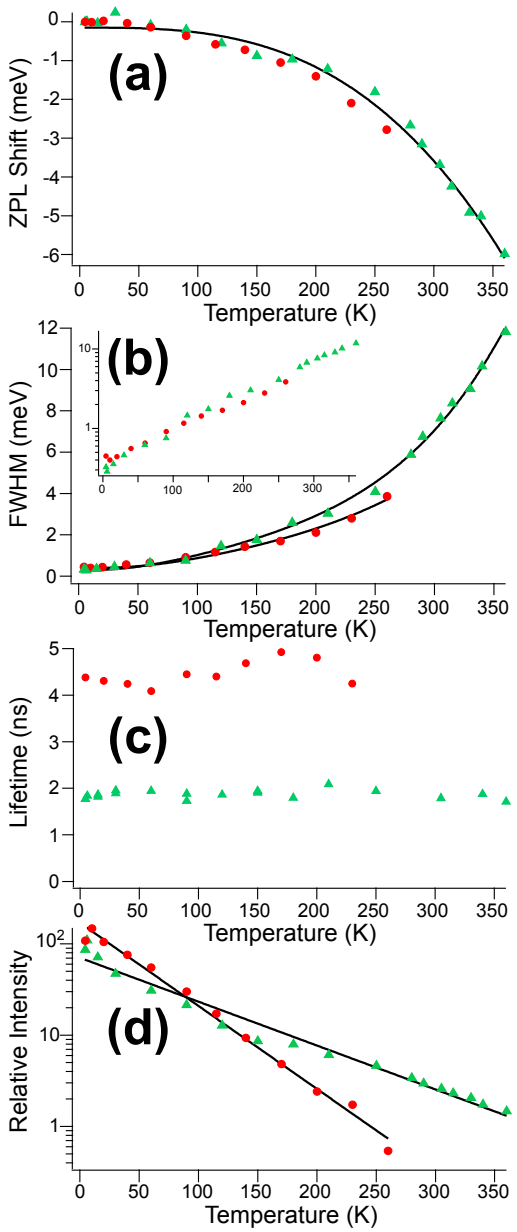

Figure 6.3: Temperature-dependent energy shift (a), linewidth (b), lifetime (c), and relative intensity (d) for two ZPLs centered at 575 nm (green triangles) and 682 nm (red circles). Each ZPL shows nearly identical behavior in (a)-(c), though the ZPL at 682 nm decreases in intensity more rapidly as temperature is increased.

First we compare the observed linewidth to the minimal, or natural, linewidth for a transition, which in the absence of phonons is given by the expression $\Gamma_{min} = \hbar/\tau$, where $\hbar$ is the reduced Planck's constant. This is the

Lorentzian linewidth that is limited by the Fourier transform of spontaneous emission, with a characteristic excited-state lifetime τ. To determine whether the broadening we observe is related to a change in the natural linewidth, we also measured the temperature-dependent excited-state lifetime for each ZPL transition using pulsed excitation (See *Section 6.4*). The results of this measurement, shown in Figure 6.3c, indicate that the lifetime is independent of temperature, and that the natural linewidths are 0.352 μeV and 0.148 μeV for the 575 nm line (ZPL1) and the 682 nm line (ZPL2), respectively. These are much narrower than the observed linewidths, which we note are not spectrometer-limited for the majority of temperatures. Therefore, we conclude that the linewidth broadening is not caused by a change in the natural linewidth, and that a different temperature-dependent process dominates the linewidth between 4.5 and 360 K.

Here we propose a phonon-mediated mechanism to explain the exponential linewidth broadening evident in Figure 6.3b. In a model with a single phonon frequency ω_0, interactions with phonons produce one-phonon and multiphonon sidebands that emerge as distinct satellite peaks [234]. In our model of h-BN defect emission, however, low-energy acoustic phonons, which are ungapped [167,236], produce an effective increased width to the zero-phonon line. The one-acoustic-phonon sideband is peaked at vanishing phonon energy due to the Bose factor governing the phonon occupation and has a width that increases approximately linearly with temperature. Photons emitted into the one-acoustic-phonon sideband are thus very close in energy

to the zero-phonon transition energy and are experimentally indistinguishable from the “true” zero-phonon line in our optical spectrometer. At the same time, the spectral weight of the true zero-phonon line diminishes with respect to the total emission according to the temperature-dependent factor

$$W = \exp[-S \coth(\hbar\omega_0/2kT)], \tag{6.2}$$

where k is Boltzmann’s constant and S is the Huang-Rhys factor [167]. Thus, the ratio of the amplitude of the one-acoustic-phonon contribution to the zero-phonon contribution of the narrow line will increase nearly exponentially with temperature, yielding an effective linewidth for the observed line that likewise increases exponentially with temperature. The solid lines in Figure 6.3b are best-fits to the data using this model with two free parameters. The best-fit assumes piezoelectric coupling between the defect and in-plane acoustic phonons (see *Section 6.4*). Incidentally, the defect predominantly couples to phonons in its particular two-dimensional h-BN sheet. The Huang-Rhys factors from the best-fits are $S = 2.1 \pm 0.7$ and $S = 3.3 \pm 2.3$ for ZPL1 and ZPL2, respectively. We note that the ZPL factor W in Equation 6.2 relates to the relative spectral weight of the ZPL [235]. Our Huang-Rhys factors correspond to 0 K ZPL factors of $W = 0.12$ and $W = 0.037$ for ZPL1 and ZPL2, respectively, consistent with the sharp, bright spectral lines experimentally observed. These values are much less than those reported previously for isolated h-BN defects [39] because our model explicitly accounts for low energy acoustic phonon processes that cannot be experimentally distinguished from zero-phonon processes by a spectrometer.

Because ZPL2 has a larger Huang-Rhys factor, we expect the amplitude of ZPL2 to decrease more rapidly with temperature than ZPL1. This expectation is verified in Figure 6.3d, which displays the temperature dependence of the relative intensity of each ZPL (see *Section 6.4*). While the relative intensity of each line decays nearly exponentially with temperature, ZPL2 decays more rapidly than does ZPL1. This observation explains why ZPL1 was studied over a broader temperature range than ZPL2.

To further examine the excitation mechanism of each ZPL, we performed polarization spectroscopy [2] on ZPL1 (Figure 6.4a) and ZPL2 (Figure 6.4b). ZPL1 possesses large absorption and emission polarization visibility with the maxima of each profile being aligned. This behavior is consistent with a single absorption and emission dipole allowing photon absorption through a phonon sideband (See *Section 6.4*). Moreover, group theoretical considerations suggest that the ground and excited state wavefunctions of ZPL1 are likely orbital singlets [2,208]. Conversely, ZPL2 shows lower polarization visibility with a ~$60°$ misalignment between the maxima of absorption and emission. These observations suggest that the electronic states coupled by the incident laser field differ from those that produce ZPL2, perhaps because ZPL2 results from cross relaxation between defects.

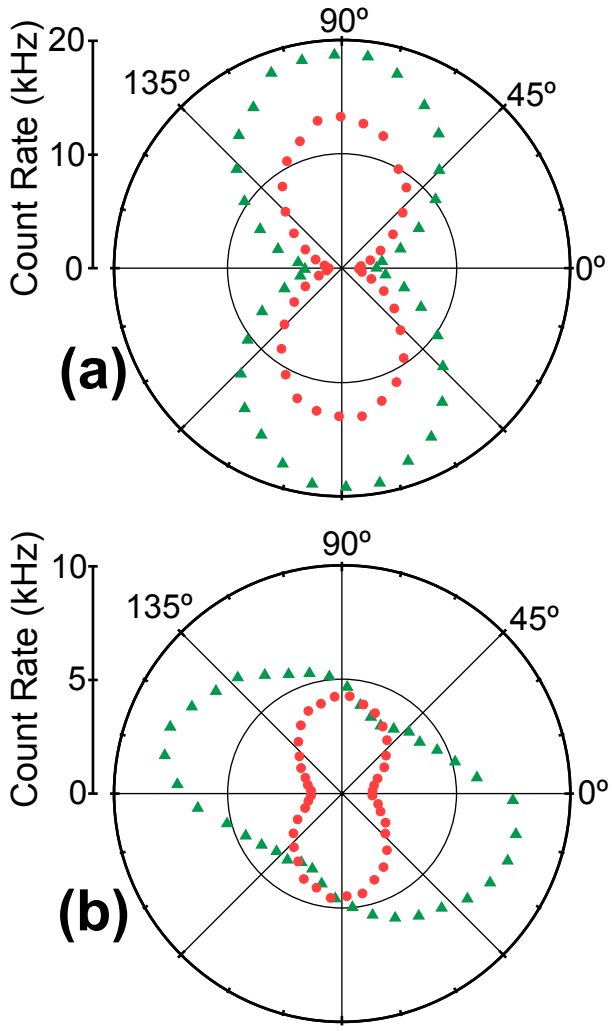

Figure 6.4: Polarization spectroscopy measurements of absorption (green triangles) and emission (red circles) for ZPLs at 575 nm (a) and 682 nm (b). The profiles in (a) are consistent with a single absorption and emission dipole aligned parallel to one another. The profiles in (b) show lower polarization visibility and the maxima of absorption and emission are misaligned by ~60°, suggesting the 682 nm line is excited indirectly.

In conclusion, we investigated the distribution and temperature dependence of sharp emission lines in h-BN to better understand the properties of native point defects. Our results, which survey a range of ~500 meV, reveal a dense, broad forest of narrow emission lines that likely result from inhomogeneous broadening of several defect species. By combining

optical filters with time correlated single photon counting, we identify six narrow lines that correspond to single photon emission from individual defect states.

For two of the identified ZPLs, we investigate the temperature dependent linewidth, energy shift, and intensity. Each ZPL exhibits similar linewidth broadening and red shifting as temperature is increased. In contrast to other defect systems in diamond [228,230] and SiC [233], the measured linewidth increases exponentially with temperature. We explain this result by invoking the nature of the in-plane one-acoustic-phonon sideband, and speculate that this feature is more pronounced for the h-BN lattice due to its van der Waals nature (softer modes). Additionally, we find that the relative intensity of each ZPL decreases exponentially with temperature. Finally we present evidence that h-BN defects may either be excited by direct phonon-mediated absorption, or indirectly by cross-relaxation.

6.3 Experimental

The investigated h-BN flakes are commercially available from Graphene Supermarket (See *Section 6.4* for sample characterization). As received the flakes are suspended in an ethanol/water solution. After drop casting $25\ \mu L$ of solution onto a thermally oxidized Si substrate, we anneal samples at $850°\ C$ for 30 minutes under continuous nitrogen flow. The ramp rate was $5°\ C/min$ and the samples were allowed to cool overnight after the annealing treatment.

All measurements were performed on samples loaded in a Janis ST-500 cryostat using a house-built confocal microscope (See *Section 6.4*). When collecting temperature dependent data, a minimum of one minute was allotted for each degree Kelvin temperature change to ensure that the sample had reached thermal equilibrium.

6.4 Supplementary Information

6.4.1 Sample Details

All data presented in the main text are from point defects in hexagonal boron nitride (h-BN) flakes purchased from Graphene Supermarket. As received, the h-BN flakes are suspended in a 50/50 ethanol/water solution. We drop cast 25 μL of solution onto a thermally oxidized silicon substrate and anneal for 30 minutes at 850°C under continuous nitrogen flow. This annealing procedure was motivated by a previous investigation [39] that tested a range of annealing temperatures and found that 850°C removed surface contaminants and yielded high defect fluorescence intensity. Aside from the drop casting and the subsequent annealing procedure the samples were not modified in any way.

To verify that the investigated flakes are truly h-BN without traces of cubic boron nitride (cBN), for instance, we performed Raman spectroscopy. Figure 6.5a is an optical micrograph of the h-BN flakes after drop casting and

annealing. The flake density here is 3x greater than for samples investigated in the main text. The flakes are clearly visible and they tend to aggregate. The boxed region in Figure 6.5a is magnified in Figure 6.5b. Spatially resolved Raman spectroscopy was performed on three locations denoted by the red, black, and blue circles. The Raman spectrum for each location is shown in Figure 6.5c. The red circle is in a region densely packed with flakes, and consequently its corresponding red Raman spectrum has a pronounced peak at the characteristic h-BN shift of ~1366 cm^{-1} (~170 meV). The black circle is in a location less dense with flakes and therefore a smaller Raman peak results. Lastly, because there are no flakes at the location of the blue dot, there is no h-BN Raman peak in the blue Raman spectrum. We did not observe any Raman peaks associated with cBN (~1055 cm^{-1} and 1305 cm^{-1}) in our survey.

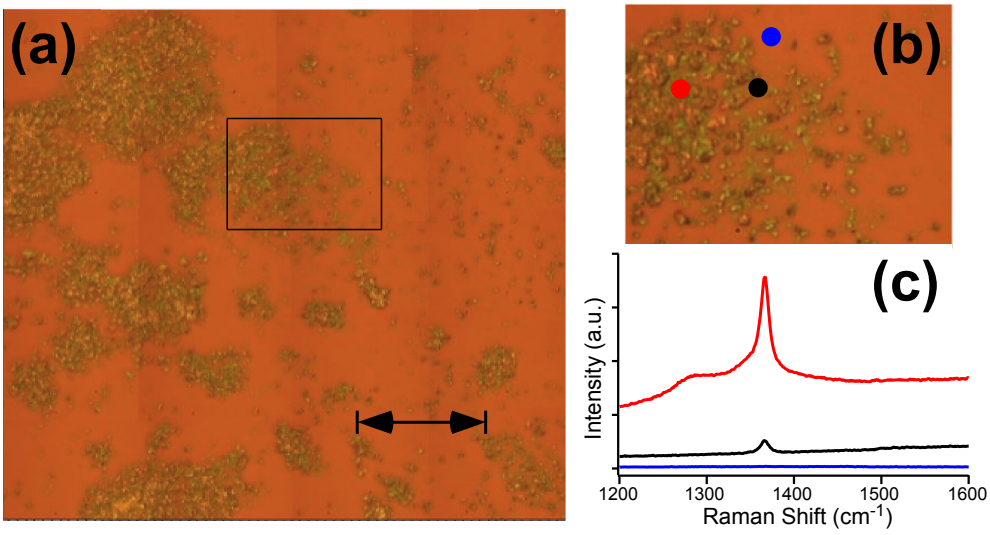

Figure 6.5: (a) Optical micrograph of h-BN flakes on a thermally oxidized Si substrate post annealing. The Scale bar is 30 μm. (b) Magnified view of the boxed region in (a). (c) Spatially resolved Raman spectra color-coordinated to the three colored circled in (b).

To further characterize our samples, we performed energy dispersive X-ray spectroscopy (EDX) of the h-BN flakes. Figure 6.6a is an electron micrograph of the flakes following drop casting and annealing. As in Figure 6.5a, the flakes are clearly visible as the brighter regions and they preferably aggregate. Figure 6.6b-e are elemental EDX maps of the boxed region for boron, nitrogen, oxygen, and carbon, respectively. As anticipated, the region corresponding to h-BN flakes shows high concentrations of boron and nitrogen whereas the region corresponding to the substrate is dominated by oxygen.

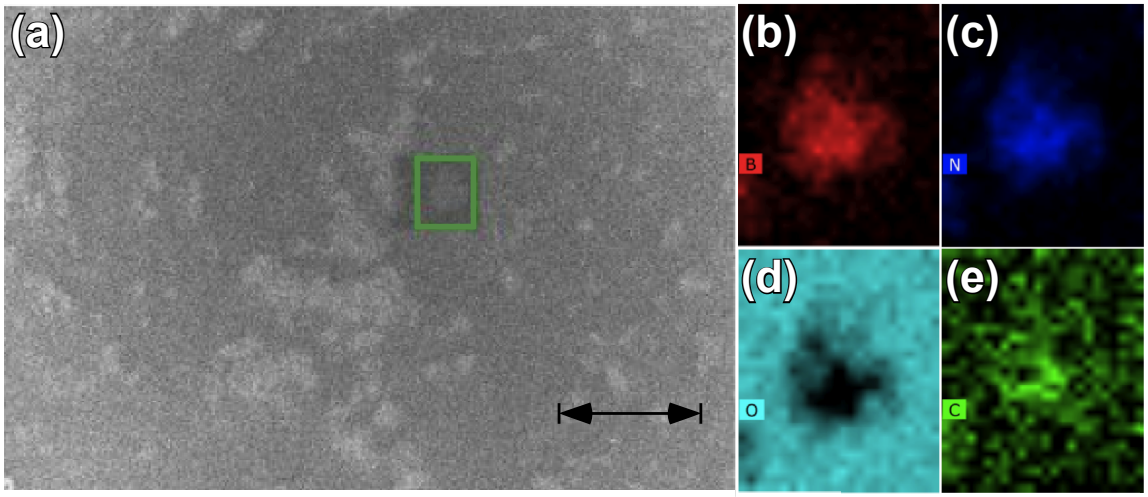

Figure 6.6: (a) Electron micrograph of h-BN flakes on a thermally oxidized Si substrate. The scale bar is 70 μm. Spatial EDX mapping for the boxed region in (a) for boron (b), nitrogen (c), oxygen (d), and carbon (e).

We also investigated defects in monolayer h-BN. These data are not in the main text but select results are presented in *Section 6.4.4* below. These h-BN monolayers were grown on Cu foil via CVD and a 1 cm x 1 cm piece was subsequently transferred to a thermally oxidized Si substrate. For the transfer, PMMA was spin coated on the h-BN side of the as grown h-BN/Cu sample.

The Cu foil was etched by dipping the sample in a Ferric Chloride solution (CE-100 from Transene Company Inc.) for 2-3 hours. Next, the PMMA/h-BN layer was placed in DI-Water and left to float for ~12 hours to remove all ionic residues that resulted from the Cu etching procedure. The PMMA/h-BN layer was then transferred to a thermally oxidized Si substrate and left to dry in air for 30-60 minutes. To remove the PMMA, the sample was submerged in acetone for ~12 hours. Finally, the h-BN monolayer was annealed in air at $500°C$ for 30 minutes.

6.4.2 Experimental Apparatus

Figure 6.7 is a schematic of the house-built confocal microscope used in this work. A continuous wave 532 nm laser was used for the excitation source in all spectral and $g^{(2)}(\tau)$ measurements. For excitation measurements, a fixed polarizer (FP1) followed by a half wave plate (HWP1) enables creation of an arbitrary polarization state of the exciting light. A fixed wave plate (FWP1) corrects for retardances introduced by the rest of the excitation path [2].

For the emitted light, a beam splitter (BS) placed between the dichroic mirror (DM) and the 0.7 NA microscope objective (MO) enables spectral measurements to be made that are minimally affected by wavelength-dependent transmission of optical elements. Photons not directed to the spectrometer encounter a Hanbury Brown and Twiss interferometer used for $g^{(2)}(\tau)$ measurements [1] and are either detected at APD1 or APD2. APD1

may be used for polarized excitation measurements and APD2 for measurements on the polarization of the emitted light. The filter wheel (FW) contains a combination of long- and short-pass filters that enable spectrally resolved time correlated single photon counting (TCSPC) measurements.

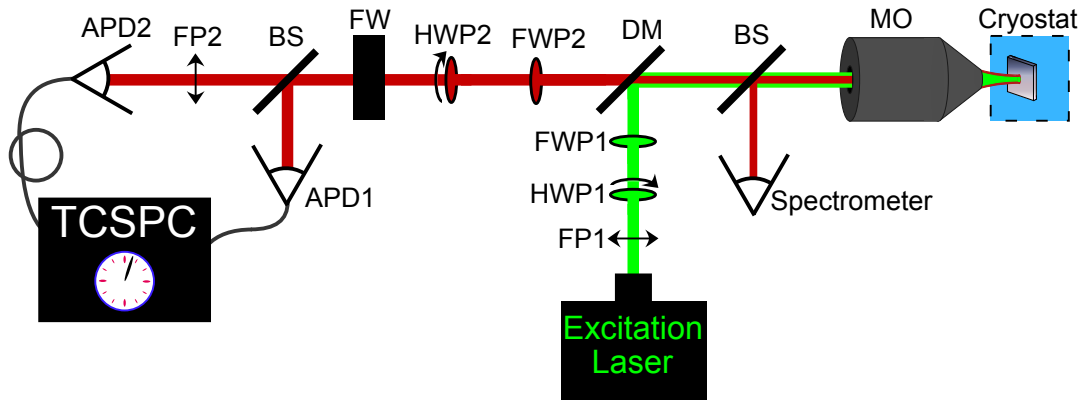

Figure 6.7: Schematic of confocal microscope used in this work.

6.4.3 Time Correlated Single Photon Counting (TCSPC)

A Becker & Hickl TCSPC module (SPC-130) was used for $g^2(\tau)$ and lifetime measurements. Figure 6.8 displays the instrument response function (IRF) of our detection setup measured using a pulsed laser with a 350 ps pulse width. A Gaussian fit to the IRF indicates a full width at half maximum (FWHM) of ~0.71 ns.

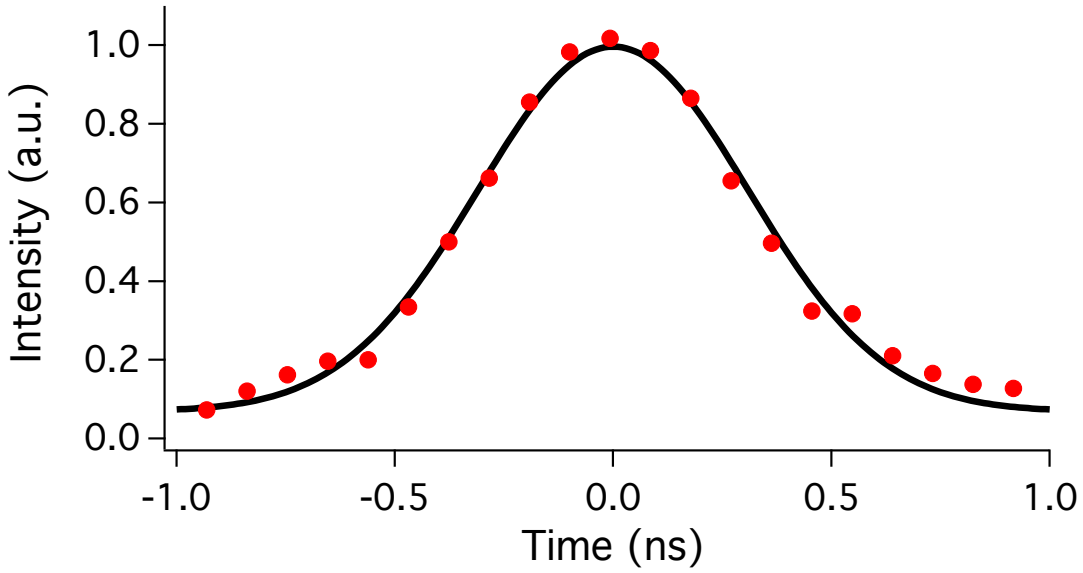

Figure 6.8: Instrument response function of our detection setup revealing a FWHM of ~0.71 ns.

For two-photon correlation measurements the raw data, $n_M(\tau)$, corresponds to the number of photon pairs detected with a relative delay time in the range $(\tau, \tau + \delta\tau)$, where $\delta\tau$ is the bin width. Because of the finite width of the IRF (Figure 6.8), $n_M(\tau)$ will deviate from the "true" number of coincidence counts, $n_T(\tau)$. The measured $n_M(\tau)$ is given by the convolution integral of $n_T(\tau)$ and the IRF,

$$n_M(\tau) = \int_{-\infty}^{\infty} \frac{1}{\sqrt{2\sigma^2\pi}} \exp\left[\frac{(\tau-\tau')^2}{2\sigma^2}\right] n_T(\tau')d\tau', \quad (6.3)$$

where σ is the standard deviation of the IRF. Because we do not directly detect a long-lived decay in $n_M(\tau)$, we utilize a two-state model for $n_T(\tau)$,

$$n_T(\tau) = n_{max} + (n_0 - n_{max}) \exp(-\lambda|\tau|), \quad (6.4)$$

where n_0, n_{max}, and λ are free parameters. We may use Equations 1 and 2 to fit the as-recorded $n_M(\tau)$. To convert $n_M(\tau)$ and $n_T(\tau)$ to the two-photon

correlation functions, $g_M^{(2)}(\tau)$ and $g_T^{(2)}(\tau)$,, we normalize by the factor $r_1 r_2 T \delta\tau$, where r_1 (r_2) is the average count rate at APD1 (APD2) and T is the total collection time. When fitting the data shown in the main text in Figure 6.1d and 6.1e using Equations 6.3 and 6.4 we find true $g_T^{(2)}(0)$ values of 0.22 and 0.42, respectively. This is only a minor correction to the values of 0.24 and 0.44 reported in the main text that result when assuming the IRF is a Dirac delta function.

Figure 6.9 shows the fluorescence intensity collected from the 575 nm ZPL and the 682 nm ZPL as a function of excitation laser power measured at the back aperture of the microscope objective. Note that these photon count rates are not background corrected and represent the total light collected in the bandwidths shown in Figure 6.1 of the main text. The 575 nm ZPL is brighter and saturates at a higher laser power than does the 682 nm ZPL. The dashed green and red lines correspond to the laser power used for the $g^{(2)}(\tau)$ measurements shown in Figure 1 of the main text.

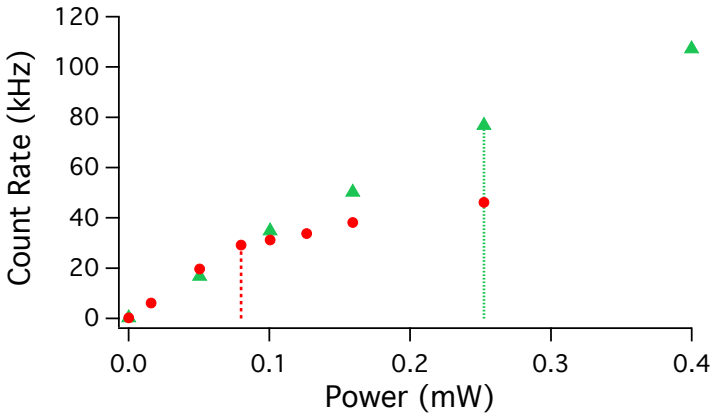

Figure 6.9: Saturation curve for the 575 nm ZPL (green triangles) and 682 nm ZPL (red circles).

For lifetime measurements the excitation source was a 532 nm pulsed laser (80 kHz repetition rate with 350 ps pulse width). Figure 6.10 displays two normalized lifetime measurements plotted on a log scale. The lifetime, τ, of each transition is determined from an exponential fit, $\exp(-t/\tau)$, to the data.

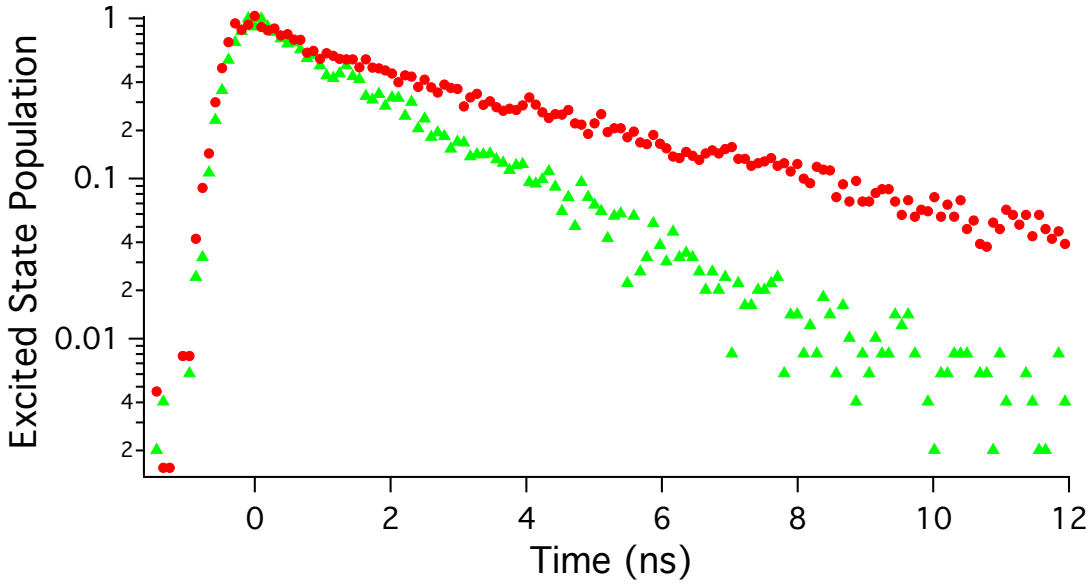

Figure 6.10: Normalized lifetime measurements acquired at 4.5 K for the 575 nm line (green triangles) and the 682 nm line (red circles).

6.4.4 Point Defects in Monolayer h-BN

In contrast to the defects in multilayer h-BN presented in the main text, isolated defects in our single layer h-BN samples exhibit unreliable photostability and broad spectral emission. Figure 6.11 displays the fluorescence intensity of an isolated defect in single layer h-BN over ~14 seconds. Though bright, this defect blinks between a bright state and a dark

state and eventually photobleaches after several minutes. Conversely, the multilayer h-BN defects discussed in the main text remained photoactive for the entire measurement duration (>24 hours for temperature dependent measurements) without bleaching.

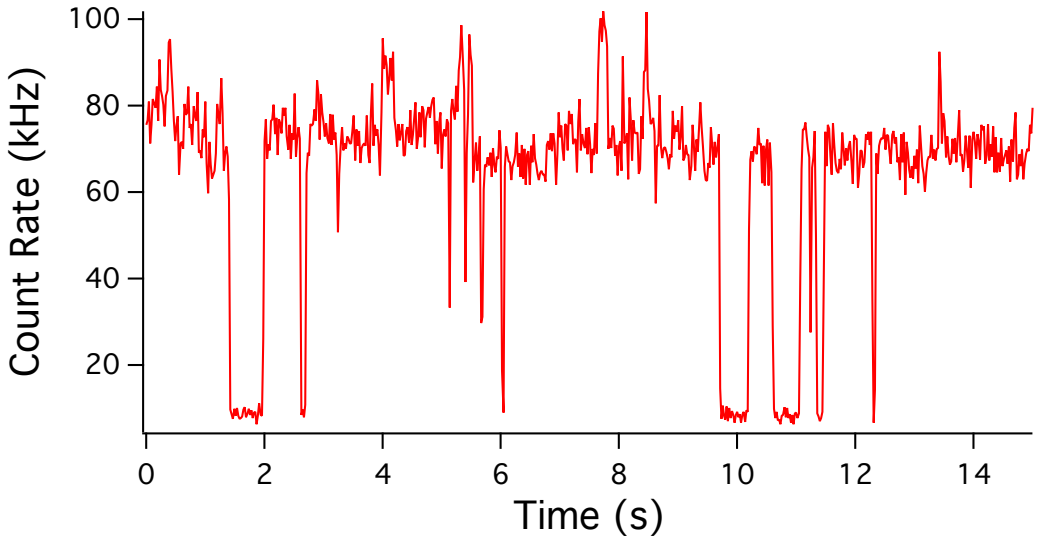

Figure 6.11: Fluorescence time trace of a single defect in monolayer h-BN.

Though defects in multilayer h-BN posses superior photostability, there is evidence that the defects may possess of the same structure. Figure 6.12 compares the emission spectra of a two distinct single defects in monolayer and multilayer h-BN. The monolayer emission is shown in red and was acquired at 80 K whereas the multilayer emission is shown in blue and was acquired at 150 K. Each spectrum has a maximum emission at ~575 nm, which facilitates direct comparison. The blue spectrum possesses a broadened zero-phonon line (ZPL) with an associated optical-phonon sideband ~165 meV to the red. This energy is close to the Raman shift

energy of ~170 meV (Figure 6.5) and also correlates well with the maxima of the h-BN phonon density of states [236]. This optical-phonon sideband is likely responsible for the absorption of 532 nm exciting light by the 575 nm ZPL. The red spectrum from monolayer h-BN does not possess a narrow linewidth ZPL. Nonetheless, it likewise has a phonon sideband peak separated by the same energy of ~165 meV. These observations suggest that each defect may have the same structure. If this is the case, then it may be possible to enhance the photostability of defects in monolayer h-BN via surface treatments.

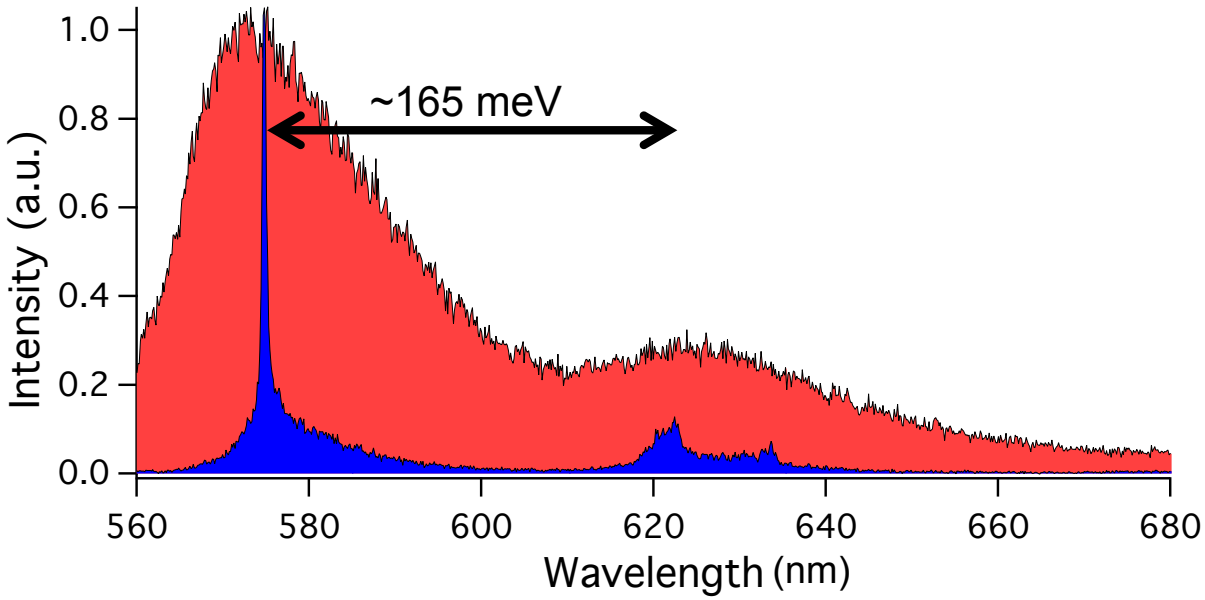

Figure 6.12: Comparison of the emission spectra of an individual defect in monolayer (red curve) and multilayer (blue curve) h-BN.

6.4.5 Phonon Sidebands

Figure 6.2b in the main text displays the distribution of emission lines with a FWHM below 4 meV at cryogenic temperatures. This cutoff was selected because phonon-sideband lineshapes are influenced by the phonon

density of states (DOS) and the sharpest feature in the bulk h-BN phonon density of states (DOS) is ~5 meV [236]. Consequently, many of the observed lines are presumably zero-phonon emission from individual defects. That said, phonon sidebands from h-BN defects may conceivably exhibit peaks sharper than 5 meV if one of two assumptions is invalid. First, we assume that the relevant modes are bulk phonon modes as opposed to local phonon modes. If local phonon modes dominate and the local phonon DOS possesses sharp peaks, then a correspondingly narrow defect emission line may be observed that is not a zero-phonon line. Secondly, we assume that the full DOS needs to be considered as opposed to the width of the phonon branch at a particular range of phonon momenta. This assumption is typically valid for localized defects where crystal momentum is not a conserved quantity.

6.4.6 Emission Spectra Fitting and Relative Intensity

Each as-acquired emission spectrum, $I_\lambda(\lambda)$, represents the emission rate of photons with wavelength λ per unit wavelength. In this work, each as-acquired emission spectrum was first converted to energy spectral density, $I_E(E)$, according to the relation $I_E(E) \propto \lambda^2 I_\lambda(\lambda)$. As stated in the main text, sharp emission lines were then fit to a linear combination of a background and a Lorentzian lineshape. The FWHM of each line was extracted directly from the FWHM of the Lorentzian fit. Figure 6.13 displays the lineshape of the 682 nm ZPL at 4.5 K (red circles). The solid black line and dashed blue line

are best-fits to the data using a Lorentzian and Gaussian lineshape, respectively. The solid black line better fits the data and justifies our use of a Lorentzian lineshape.

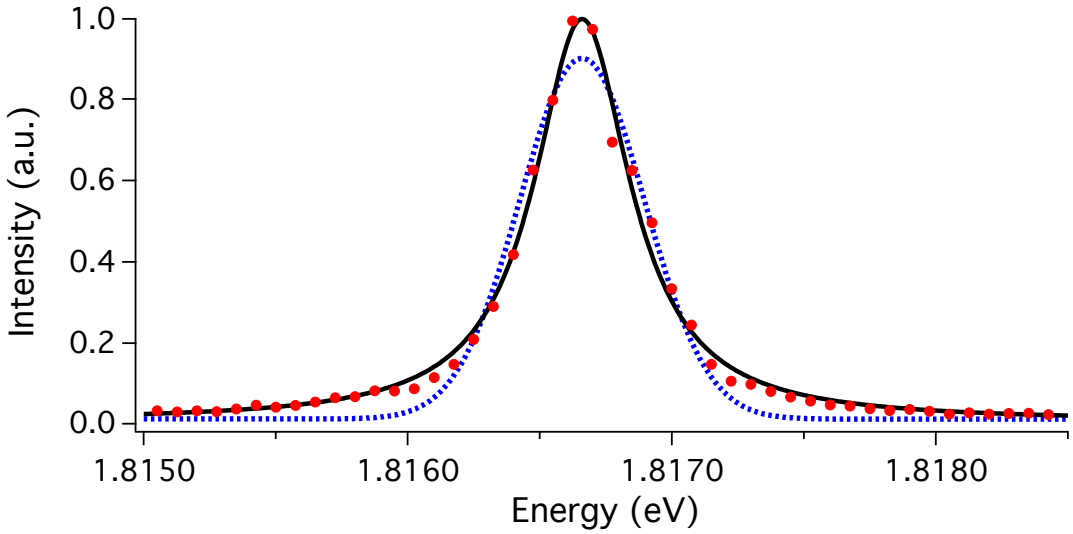

Figure 6.13: Comparison of Lorentzian (solid black line) and Gaussian (dashed blue line) best-fits to the 682 nm line.

We define the relative intensity of each line, I_R, as the ratio of the Lorentzian lineshape intensity to that of the background at E_{zpl}. Figure 6.14 illustrates the how the relative intensity is calculated. Here the blue curve is the 575 nm ZPL at 360 K and the red curve is the same data with the Lorentzian fit subtracted. The dashed line corresponds to E_{zpl} and the blue and red diamonds correspond to $I_{tot}(E_{zpl})$ and $I_{BG}(E_{zpl})$, where I_{tot} is the total signal and I_{BG} is the background signal. Note that the background signal may arise from other defects, the substrate, or from multiphonon processes of the same defect that produced the 575 nm line. In Figure 6.14 the relative intensity becomes $I_R = [I_{tot}(E_{zpl}) - I_{BG}(E_{zpl})]/I_{BG}(E_{zpl}) \approx 1.5$.

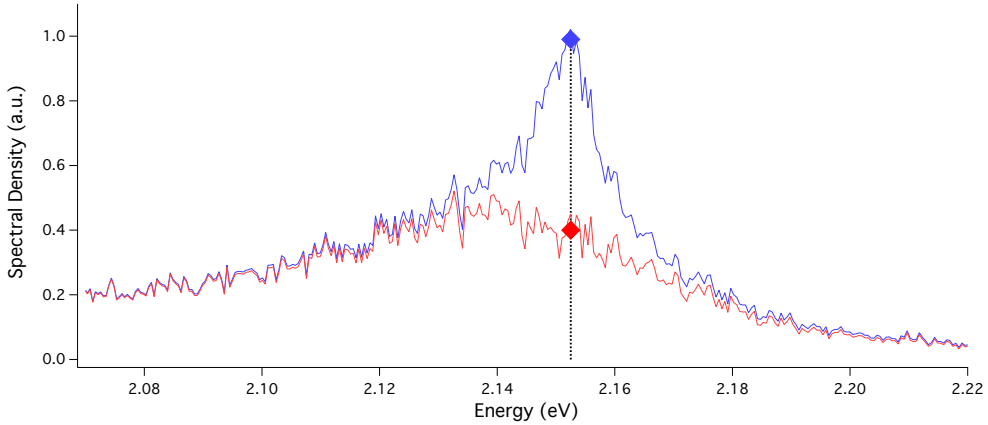

Figure 6.14: Energy spectral density of 575 nm line at 360 K before (blue) and after (red) subtraction of the Lorentzian fit.

6.4.7 Distribution of Narrow Emission Lines

When excited with 532 nm light, h-BN exhibits emission lines with a FWHM of less than 4 meV and $I_R > 1$ that are densely distributed across an energy range exceeding 500 meV (see Figure 6.2b in main text). To assess if the distribution of sharp emission lines is multimodal, perhaps owing to the presence of multiple defect species, we compute the kurtosis κ of the distribution:

$$\kappa = \frac{\mu_4}{\mu_2^2}. \tag{6.5}$$

Here μ_n is the nth moment of the distribution, defined as

$$\mu_n = \frac{1}{N}\sum_{i=1}^{N}(E_i - \mu)^n, \tag{6.6}$$

where N is the number of emission lines in the distribution, E_i is the ith line position, and μ is the average line position. When applying Equations 6.5 and

6.6 to Figure 6.2b we find $\kappa = 2.11$, which differs from the $\kappa = 3$ value expected for a normal distribution.

6.4.8 Linewidth Broadening Model and Fitting

We assume that near the zero-phonon line the spectral lineshape, $G(E)$, solely results from zero-phonon and one-phonon processes:

$$G(E) = G_{zpl}(E) + G_{opl}(E). \tag{6.7}$$

Here G_{zpl} is the true zero-phonon lineshape, G_{opl} is the lineshape that results from one-phonon processes, and E is the energy shift from the zero-phonon line energy, E_{zpl}. Here we use the method of moments to extract the FWHM from Equation 6.7. Because the second moment of a Lorentzian diverges, we use the Gaussian approximation that the FWHM, Γ, of $G(E)$ is

$$\Gamma^2 = 8\ln(2)\frac{\int E^2 G(E)dE}{\int G(E)dE}. \tag{6.8}$$

Experimentally, the measured linewidth, Γ_M, is limited by the device resolution R:

$$\Gamma_M = \sqrt{8\ln(2)\frac{\int E^2 G(E)dE}{\int G(E)dE} + R^2}. \tag{6.9}$$

In the weak coupling limit [167], G_{opl} is given by:

$$G_{opl}(E) = \frac{cg(E)f(E)}{\exp\left(\frac{E}{kT}\right)-1}. \tag{6.10}$$

Here $g(E)$ is the phonon density of states, $f(E)$ describes the defect-phonon coupling, k is Boltzmann's constant and T is the temperature. Additionally, the spectral weight of the ZPL diminishes with temperature as:

$$\int G_{zpl}(E)dE = D\exp\left(-S\mathrm{Coth}(\hbar\omega_0/2kT)\right). \tag{6.11}$$

Here S is the Huang-Rhys factor, $\hbar$ is the reduced Planck's constant, ω_0 is the phonon frequency, and D is a constant. By combining Equations 9-11, and neglecting the natural width of the ZPL, we obtain:

$$\Gamma_M = \sqrt{8\ln(2)\frac{\int E^2 G_{opl}dE}{D\exp[-S\mathrm{Coth}(\hbar\omega_0/2kT)]+\int G_{opl}(E)dE} + R^2}. \tag{6.12}$$

In the limit that low-energy phonons dominate, we have

$$\Delta E = E_{exc} - E_{zpl} = 2S\hbar\omega_0, \tag{6.13}$$

where E_{exc} is the laser excitation energy. Then Equation 12 becomes:

$$\Gamma_M = \sqrt{8\ln(2)\frac{\int E^2 G_{opl}dE}{D\exp[-S\mathrm{Coth}(\Delta E/4SkT)]+\int G_{opl}(E)dE} + R^2}. \tag{6.14}$$

Equation 10 and 14 jointly model the effective thermal broadening of the emission line by low-energy acoustic phonons. What remains to be determined are the bounds of integration, the explicit form of the phonon density of states, $g(E)$, and the defect-phonon coupling term $f(E)$.

In two dimensions with piezoelectric coupling, $g(E) \propto E$ and $f(E) \propto E^{-1}$. In such a scenario our fitting function of two free parameters A, S becomes:

$$\Gamma_M = \sqrt{8\ln(2)\frac{\int E^2 dE/\left[\exp\left(\frac{E}{kT}\right)-1\right]}{A\exp[-S\mathrm{Coth}(\Delta E/4SkT)]+\int dE/\left[\exp\left(\frac{E}{kT}\right)-1\right]} + R^2}. \tag{6.15}$$

We used Equation 6.15 to fit our experimentally measured linewidths using a χ^2 minimization procedure. In our best-fits, the integration bounds in Equation 6.15 were 0.001 meV to 200 meV. The 200 meV cutoff was chosen because this is where the h-BN phonon density of states vanishes [236]. The spectrometer resolution R was determined to range between 0.3 meV and 0.4 meV depending on the spectrometer slit width.

To test our assumption that in-plane phonons with piezoelectric coupling dominate the measured linewidth we also considered the following fitting function:

$$\Gamma_M = \sqrt{8\ln(2)\frac{\int E^{2+n}dE/\left[\exp\left(\frac{E}{kT}\right)-1\right]}{A\exp[-S\mathrm{Coth}(\Delta E/4SkT)]+\int E^{n}dE/\left[\exp\left(\frac{E}{kT}\right)-1\right]}+R^2}. \quad (6.16)$$

When fitting using Equation 6.16, we fixed n and allowed A, S to vary as free parameters. In Figure 6.15 we plot the normalized minimum χ^2 for different values of n for each ZPL investigated. This plot supports the value $n = 0$ and our assignment that the relevant phonons are in-plane with piezoelectric coupling.

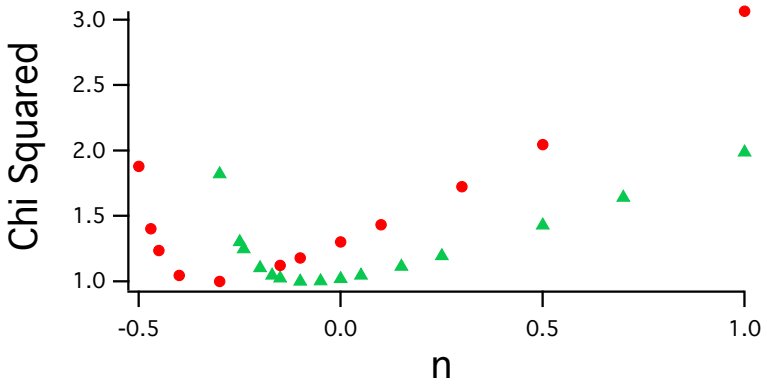

Figure 6.15: Minimum χ^2 for different values of n for the 575 nm ZPL (green triangles) and the 682 nm ZPL (red circles).

6.5 Acknowledgements

Research support for *Chapte*r 6 was provided by the National Science Foundation (DMR-1254530). We acknowledge use of the Cornell NanoScale Facility, a member of the National Nanotechnology Coordinated Infrastructure (NNCI), which is supported by the National Science Foundation (Grant ECCS-15420819). Additionally, we acknowledge the Cornell Center for Materials Research Shared Facilities, which are supported through the NSF MRSEC program (DMR-1120296). Michael E. Flatté acknowledges support from an AFOSR MURI.

CHAPTER 7

OPTICAL ABSORPTION AND EMISSION MECHANISMS OF SINGLE DEFECTS IN HEXAGONAL BORON NITRIDE [4]

7.1 Chapter Abstract

We investigate the polarization selection rules of sharp zero-phonon lines (ZPLs) from isolated defects in hexagonal boron nitride (h-BN) and compare our findings with the predictions of a Huang-Rhys model involving two electronic states. Our survey, which spans the spectral range ~550-740 nm, reveals that, in disagreement with a two-level model, the absorption and emission dipoles are often misaligned. We relate the dipole misalignment angle ($\Delta\theta$) of a ZPL to its energy shift from the excitation energy (ΔE) and find that $\Delta\theta \approx 0°$ when ΔE corresponds to an allowed h-BN phonon frequency and that $0° \leq \Delta\theta \leq 90°$ when ΔE exceeds the maximum allowed h-BN phonon frequency. Consequently, a two-level Huang-Rhys model succeeds at describing excitations mediated by the creation of one optical phonon but fails at describing excitations that require the creation of multiple phonons. We propose that direct excitations requiring the creation of multiple phonons are inefficient due to the low Huang-Rhys factors in h-BN and that these ZPLs are instead excited indirectly via an intermediate electronic state. This hypothesis is corroborated by polarization measurements of an individual ZPL excited with two distinct wavelengths that indicate a single ZPL may be excited by

multiple mechanisms. These findings provide new insight on the nature of the optical cycle of novel defect-based single photon sources in h-BN.

7.2 Main Text

Wide bandgap semiconductors host point defects, or color centers, that can feature optical and spin properties that are useful for applications in quantum optics, precision sensing, and quantum information technology [15,18,20,117,238]. Some color centers, such as the nitrogen vacancy (NV) center in diamond [12,21,182,228,231,232], are bright enough to be investigated in the single defect limit using single-molecule microscopy techniques [9,10]. While diamond is the most celebrated host material, the last several years have witnessed the discovery of defect-based single photon sources in SiC [20,24–29,123], ZnO [1,2,30–33], GaN [34], WSe_2 [35–37], WS_2 [38], and hexagonal boron nitride (h-BN) [3,39–51]. The latter three materials exist as two-dimensional monolayers and layered solids, thus offering the possibility of integrating single-photon sources with van der Waals heterostructure devices for tuning and other control. Defect emission in h-BN can be ultrabright [39], have a narrow linewidth [3], be tuned [45], and remain photostable up to 800 K [47]. These positive attributes have sparked strong interest in h-BN defects from research groups around the world [3,39–51]. Despite this surge of interest, most works have focused on characterizing the phenomenology of h-BN emission, leaving open several difficult to answer

questions regarding the fundamental nature of h-BN quantum emitters. These include the structural origin of the defect(s) responsible for single photon emission, the reason(s) for the broad distribution of zero-phonon line (ZPL) energies (E_{ZPL}), the spin properties, and the physical mechanism(s) involved in the defect's optical cycle.

In this work we address the transition mechanism(s) involved in the defect's optical cycle. We perform spectrally-resolved polarization measurements of optical absorption and emission at cryogenic temperatures and compare our findings with the predictions of a Huang-Rhys model. We find that when the energy difference between the exciting light and the ZPL is less than the maximum phonon energy in h-BN, the defect's polarization properties are well-explained by a Huang-Rhys model with two electronic states. Conversely, when this energy difference exceeds the maximum phonon energy, a Huang-Rhys model with two electronic states fails at explaining the observed behavior. These findings suggest that ZPL emission may be mediated by an intermediate electronic state. This explanation is supported by polarization measurements performed with lasers of different energies that verify a single ZPL may be excited via multiple mechanisms. These effects, which have not been observed in another defect system, arise in h-BN owing to the combination of a small Huang-Rhys factor (strong ZPL), large oscillator strength (nanosecond-scale excited state lifetime with high quantum efficiency), and presence of many coupled electronic energy levels. Our findings, which provide new insight on the optical properties and level

structure of h-BN defects, are key for designing future experiments and applications.

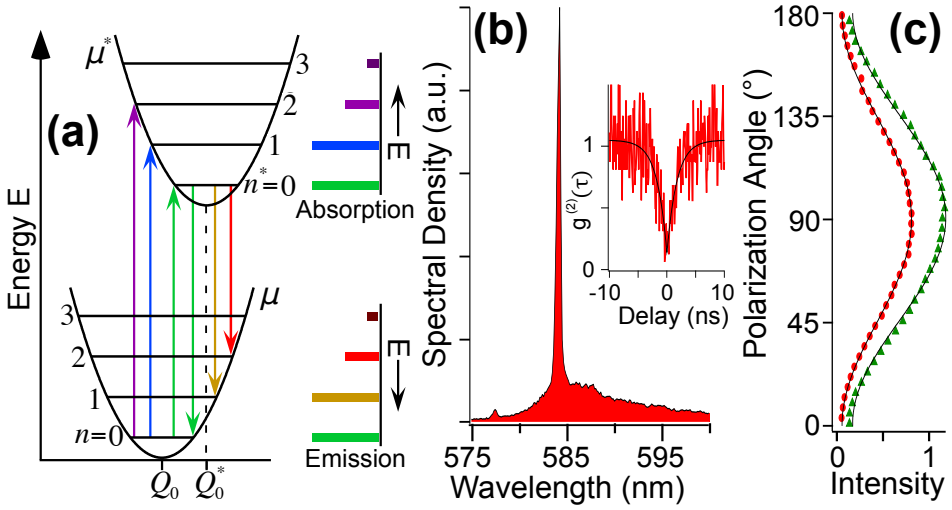

Figure 7.1: (a) Configuration coordinate diagram with $S = 1$ illustrating phonon-mediated transitions to and from an electronic ground state μ and electronic excited state μ^* at zero temperature. While in electronic ground state μ with $n = 0$ phonons, the defect may absorb an optical photon and enter state (μ^*, n^*). Following rapid thermalization to the vibronic ground state the defect may radiatively relax from state $(\mu^*, 0)$ to (μ, n) with a probability given by the Frank-Condon factor. For linear modes ($\omega = \omega^*$) the absorption and emission bands, shown on the right, are mirror reflections of one another. (b) Emission spectrum of a defect revealing a sharp ZPL at ~584 nm. This ZPL corresponds to single photon emission, as verified by the antibunching dip in $g^{(2)}(\tau)$ shown as an inset. (c) The polarization profiles for absorption (green triangles) and emission (red circles) are aligned, as predicted by the Huang-Rhys model in (a).

The fundamental mechanism governing non-resonant absorption and emission from point defects has been known for some time [234] and is illustrated in the configuration coordinate diagram shown in Figure 7.1a. In the Huang-Rhys model, a defect may undergo incoherent transitions to and from an electronic ground state (μ) and an electronic excited state (μ^*) that are mediated by lattice phonons. Note that although only one phonon frequency

ω, ω^* is depicted for each electronic state μ, μ^*, the model is readily adapted to include additional phonon modes [167,239]. In the diagram, the horizontal axis corresponds to the nuclear coordinate Q that specifies the lattice configuration and the vertical axis corresponds to the total energy of the defect-lattice system. The zero-phonon lattice configuration in the excited state, $Q_0^* = \langle \mu^* | Q | \mu^* \rangle$, differs from that of the ground state, $Q_0 = \langle \mu | Q | \mu \rangle$, because each state produces a unique electrostatic potential. Each optical cycle begins with the system in the electronic state μ and a vibronic state occupation of n phonons, with a probability governed by the Bose-Einstein distribution. Following the absorption of an optical photon, the system rapidly thermalizes and the excited state μ^* with n^* phonons is occupied. In the Frank-Condon approximation, where the fast electronic rearrangement precedes the slower lattice relaxation, the transition rate from to (μ^*, n^*) to (μ, n) is proportional to

$$|\langle \mu | \boldsymbol{r} | \mu^* \rangle|^2 \left| \int dQ \phi_{\mu,n}^*(Q) \phi_{\mu^*,n^*}(Q) \right|^2, \tag{7.1}$$

where $\phi_{\alpha,m}(Q)$ is the m-phonon lattice wave function when the defect is in electronic state α. Emission into the ZPL corresponds with $n = n^*$ transitions, where no phonons are created or annihilated. All other transitions contribute to the phonon sideband.

In Equation 7.1 the first term is the dipole matrix element of the transition. This term determines the polarization selection rules for absorption and emission and is symmetric under time reversal. Consequently, the model predicts *identical* polarization properties for absorption and emission.

Additionally, because the symmetry properties of μ and μ^* are determined by the defect's crystallographic point group, the transition dipoles are typically aligned parallel or perpendicular to distinct crystallographic directions. The second term in Equation 7.1, the Frank-Condon factor $F_n^{n^*}$, is the overlap integral between displaced harmonic oscillators. This term determines the lineshape of the absorption and emission bands. For linear modes $\omega = \omega^*$ and

$$F_n^{n^*} = e^{-S} S^{n-n^*} \left(\frac{n^*!}{n!}\right) \left(L_{n^*}^{n-n^*}(S)\right)^2, \tag{7.2}$$

where $L_{n^*}^{n-n^*}$ are the associated Laguerre polynomials and S is a measure of defect-lattice coupling called the Huang-Rhys factor. In natural units $S = \frac{1}{2} m_{eff} \omega (Q_0 - Q_0^*)^2$, where m_{eff} is the effective mass of the mode. Because Equation 7.2 is symmetric under time reversal, the absorption and emission bands of a transition are mirror reflections of one another about E_{ZPL} for linear modes. At temperature $T = 0$ there are no thermal phonons and the zero-temperature Frank-Condon factors $F_n^0 = \frac{e^{-S} S^n}{n!}$ dominate. In this limit the number of phonons created in a radiative transition is Poisson distributed about an average value of S, and the relative spectral weight of the ZPL is e^{-S}, which is the zero-temperature Debye-Waller factor.

To test the success of the Huang-Rhys model at describing the optical properties of isolated h-BN defects we performed polarization spectroscopy using a house-built confocal microscope [2] (see *Section 7.3*). Figure 7.1b is a $T = 5K$ emission spectrum of a defect that reveals the presence of a narrow

ZPL at ~584 nm. The two-photon correlation function, $g^{(2)}(\tau)$, of the collected photons (inset) possesses an antibunching dip at $\tau = 0$ extending well below 0.5, verifying that the ZPL corresponds to single photon emission from a single defect transition. To investigate the polarization properties of absorption, we rotate the polarization of the exciting light and monitor the total fluorescence intensity. The result of this absorption measurement is shown as the green triangles in Figure 7.1c. Fixing the polarization of the exciting light to maximize the fluorescence, we determine the polarization of the emitted photons using a polarization analyzer placed in the collection path of the microscope (Figure 7.1c, red circles). The solid lines are best fits using the equation

$$A + B\cos^2\left[\frac{\pi}{180}(\theta - \langle\theta\rangle)\right], \tag{7.3}$$

where $\langle\theta\rangle$ is the spectrally averaged orientation of the absorption or emission dipole. As predicted by Equation 7.1, we find that the maxima of absorption and emission are aligned for this defect. Additionally, we have shown previously that the temperature dependence of the ZPL intensity in h-BN is well-modeled by the temperature-dependent Debye-Waller factor [3]. Thus, we conclude that the Huang-Rhys model is a good description of the observed properties for the defect shown in Figure 7.1b,c.

A survey of ZPLs in h-BN reveals that, in contrast to the data shown in Figure 7.1b,c, the absorption dipole is frequently not aligned parallel to the emission dipole. To verify that the misalignment we observe is not an experimental artifact resulting from the wavelength- and polarization-

dependent retardances introduced by optical elements in the microscope, we performed spectrally resolved polarization measurements (See *Section 7.3*). For absorption we vary the polarization of the exciting light and record an emission spectrum at each angle. This measurement produces $I_{abs}(\theta, E)$, where $I_{abs}(\theta, E)\delta E$ is the number of photons collected in the energy range $(E, E + \delta E)$ when the exciting light is polarized at θ. For each energy E' we fit $I_{abs}(\theta, E')$ to Equation 7.3 to obtain $\theta_{abs}(E')$, which is the polarization angle that maximizes $I_{abs}(\theta, E)$ when $E = E'$. For the emission measurement we fix the exciting light polarization to $\theta_{abs}(E_{ZPL})$ and record an emission spectrum for a series of positions of the polarization analyzer in the collection path. In an analogous fashion to the absorption case we obtain $I_{emit}(\theta, E)$ and $\theta_{emit}(E)$ for the emitted light. We apply a calibration to $\theta_{emit}(E)$ to correct for wavelength- and polarization-dependent retardances (see *Section 7.3*) introduced by the collection path of the confocal microscope.

Figure 7.2a is a 2D image plot of $I_{emit}(\theta, E)$ for a single defect with a ZPL at 2.06 eV (603 nm) that is excited by 2.33 eV (532 nm) light. The red trace in Figure 7.2b is the unpolarized emission spectrum, $I_{emit}(E)$, obtained by vertically summing the columns in the 2D image. The one- and two-optical-phonon sidebands are evident at ~1.88 eV and ~1.7 eV, respectively, corresponding to a phonon energy of ~180 meV. The red circles in Figure 7.2c are the spectrally averaged polarization of the emitted light, $I_{emit}(\theta)$, obtained by horizontally summing the rows in the 2D image. Lastly, the red trace in Figure 7.2a corresponds to the calibrated $\theta_{emit}(E)$ and indicates that,

consistent with Equation 7.1, the polarization state of photons emitted into the ZPL is the same as for those emitted into the phonon sideband. We also measured $I_{abs}(\theta, E)$ (data not shown) and have included $\theta_{abs}(E)$ as the green trace in Figure 7.2a. This trace indicates that the ZPL and phonon sideband intensities are maximized by the same polarization angle of the exciting light. However, in disagreement with Equation 7.1, the absorption and emission dipoles are not aligned (e.g. $\Delta\theta = |\theta_{emit}(E_{ZPL}) - \theta_{abs}(E_{ZPL})| \neq 0$), suggesting that additional processes may be involved in this defect's optical cycle.

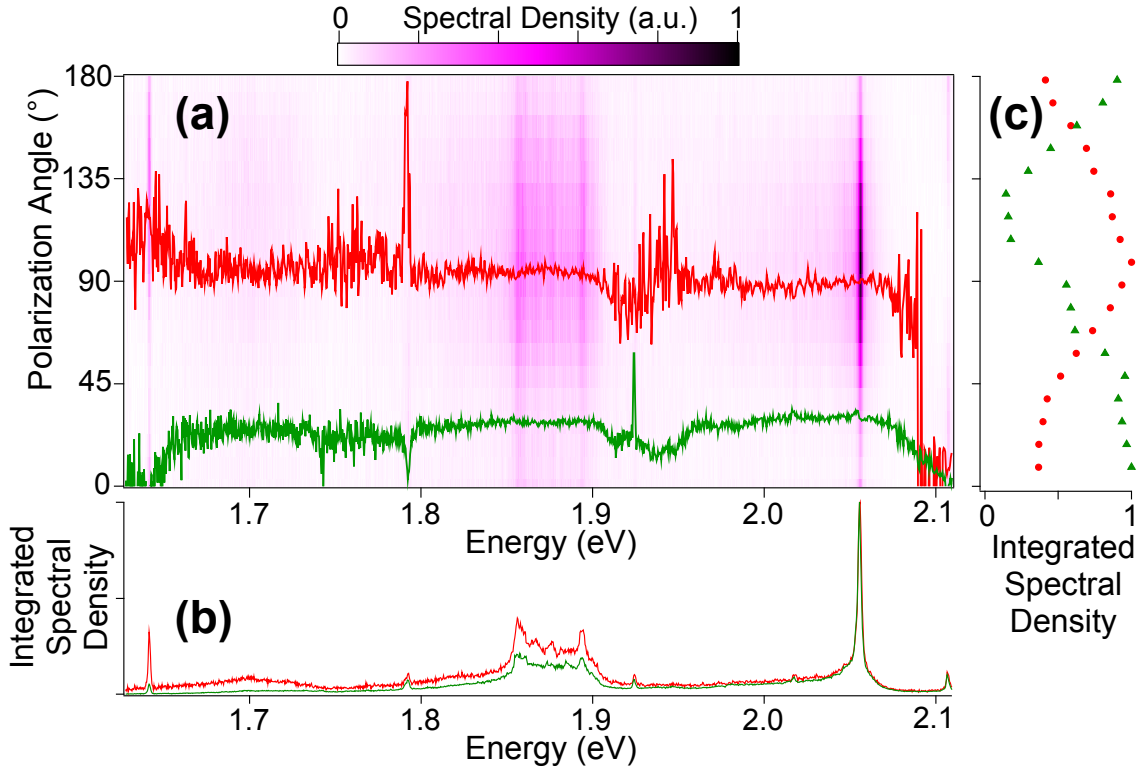

Figure 7.2: (a) 2D Image plot of $I_{emit}(\theta, E)$ with a ZPL at ~2.06 eV. The average polarization of photons emitted with energy E, $\theta_{emit}(E)$, is shown as the red trace. The unpolarized emission spectrum $I_{emit}(E)$ and the spectrally average polarization profile $I_{emit}(\theta)$, obtained by integrating the columns and rows of (a), are included as the red data in (b) and (c), respectively. The green data in (a-c) are the analogous measurements for absorption, obtained from $I_{abs}(\theta, E)$ (not shown). In contrast to Figure 7.1c, $\theta_{emit}(E_{ZPL}) \neq \theta_{abs}(E_{ZPL})$.

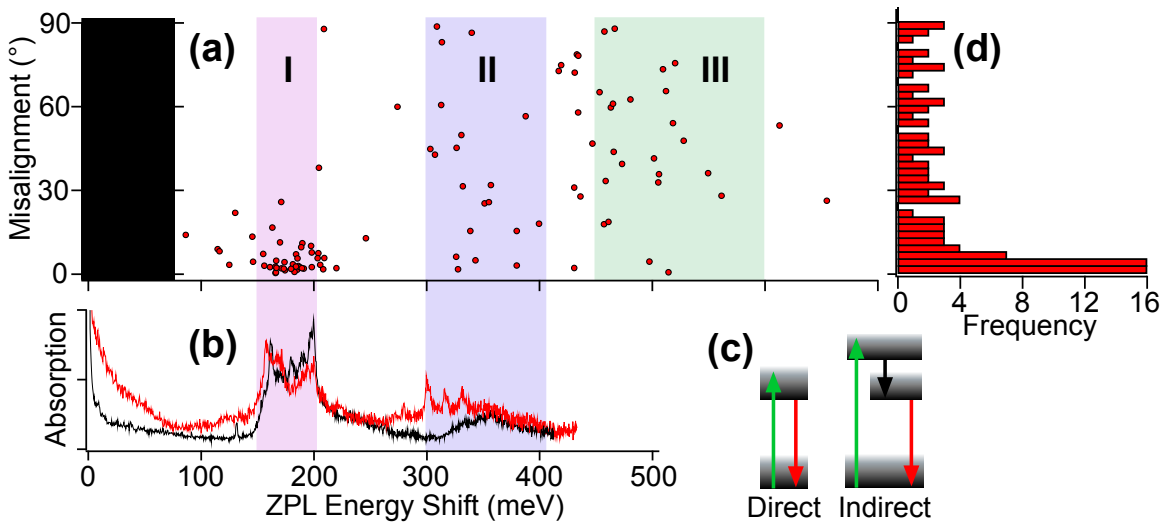

Figure 7.3: (a) Scatter plot relating the misalignment angle between the absorption and emission dipole of a ZPL ($\Delta\theta$) to its energy shift from the exciting light (ΔE) for 103 defects. The black box represents ZPL energies that could not be studied due to our selection of optical filters. The shaded region labeled "I" corresponds to the energies of in-plane optical phonons and points in this region are clustered near $\Delta\theta = 0$. ZPLs in Region II and III may be excited via the creation of two and three in-plane optical phonons, respectively. (b) The theoretical absorption band, $W(\Delta E)$, of two defects reveals peaks in Region I and II, verifying that in-plane optical phonons are relevant for absorption and emission. (c) Two energy-level diagrams illustrating direct (left) and indirect (right) excitation mechanisms. The left diagram is equivalent to Fig. 1a and predicts $\Delta\theta = 0$ whereas the right diagram allows for a broad $\Delta\theta$ distribution. (d) Histogram of all $\Delta\theta$ values shown in (a).

To better understand the failure of the model we measured $\Delta\theta$ for 103 ZPLs distributed across the region 550-740 nm. For each ZPL investigated we verified $g^{(2)}(0) < 0.5$. Figure 7.3a is a scatter plot relating the dipole misalignment $\Delta\theta$ of a ZPL to its energy shift from the exciting light, defined as $\Delta E = E_{exc} - E_{ZPL}$, where E_{exc} is the energy of the exciting light. When ΔE is less than ~200 meV the data points are clustered near small values of $\Delta\theta$, as predicted by the Huang-Rhys model. Conversely, when ΔE exceeds ~200 meV the data points are broadly distributed between $0°$ and $90°$. Therefore

~200 meV corresponds to a critical energy shift above which Equation 7.1 often fails. We will now frame this critical energy in terms of $F_n^{n^*}$ and the h-BN bulk phonon density of stares (DOS).

At cryogenic temperatures the absorption band $W(E)$ resulting from a single phonon mode is related to the Frank-Condon factor by the expression $W(E) \approx W_0 \sum_{n^*} F_0^{n^*} f(E, n^*)$, where W_0 is the oscillator strength and $f(E, n^*)$ is the lineshape of the n^*-phonon sideband. In Figure 7.3b we plot the theoretical $W(\Delta E)$ for two of the defects investigated. To determine $W(\Delta E)$ we first converted the experimentally measured luminescence spectrum $I_{emit}(E)$ to its associated emission band by the conversion factor E^{-3} that accounts for the energy-dependent density of optical states [240]. Assuming linear phonon modes, we obtain $W(E)$ by reflecting the emission band about E_{ZPL}. To enable direct comparison with Figure 7.3a, we finally shift $W(E)$ by $-E_{ZPL}$ to obtain $W(\Delta E)$. This comparison is meaningful because, for defects whose absorption is described by Equation 7.1, $W(\Delta E)$ approximates how strongly a ZPL with a particular energy shift will couple to the exciting light. Evidently, the regions of strongest absorption correspond to energy shifts of ~160-200 meV. Figure 7.3a indicates that defects with a ZPL in this spectral range are well-described by the Huang-Rhys model.

Here we compare the energies just identified to the relevant bulk phonon energies in h-BN [236]. The lowest energy modes are acoustic phonons, and we have shown previously that in-plane acoustic phonons exponentially broaden defect emission in the vicinity of the ZPL as

temperature is increased [3]. Consequently, acoustic phonons are relevant for the optical properties of defects in h-BN. However, acoustic phonons in h-BN range in energy from ~0-107 meV, and are likely not the dominant mode responsible for the absorption band peaks evident in Figure 7.3b. Optical phonon energies, on the other hand, extend from ~72-203 meV and are therefore strong candidates for phonon-mediated absorption and emission. Specifically, out-of-plane optical phonons range in energy from ~72-145 meV whereas in-plane optical phonons range from ~150-203 meV. Only the energies of in-plane optical phonons match the energies identified earlier in Figure 7.3a,b. To aid in visualizing these energies we have highlighted three regions labeled I, II, and III in Figure 7.3a,b that correspond to the absorption band of one, two, and three in-plane optical phonons, respectively. Note that only in region I is the Huang-Rhys model successful, consistent with the low Huang-Rhys factors reported previously [3,48].

Here we propose a mechanism to explain the broad $\Delta\theta$ distribution that incorporates, rather than contradicts, the model presented earlier. In Figure 7.1a direct absorption between two electronic states is mediated by lattice phonons. This scenario of direct absorption is again depicted on the left of Figure 7.3c, where the vibronic states of the lattice are represented as a blurred continuum. Alternatively, the two electronic states that produce a ZPL may be coupled indirectly via an intermediate electronic state (Figure 7.3c, right) that can be intrinsic to the defect or originate from a neighboring defect. Here transitions between any pair of electronic states are still described by the

Huang-Rhys model. However, because the electronic states coupled by the exciting light differ from those that produce the ZPL, we no longer anticipate $\Delta\theta = 0°$.

Although the indirect absorption mechanism correctly predicts a broader $\Delta\theta$ distribution, it does not predict the shape of the distribution, shown in Figure 7.3d. Specifically, if the electronic states are crystallographically related, group theoretic considerations [2,208] predict $\Delta\theta = 0°$ for direct absorption and $\Delta\theta \epsilon \{0°, 30°, 60°, 90°\}$ for indirect absorption. Figure 7.3d does not reveal clustering at these values but rather suggests a flat distribution with clustering at $0°$. We propose two explanations for this disagreement. Firstly, we note that our measurement of $\theta_{abs}(E_{ZPL})$ and $\theta_{emit}(E_{ZPL})$ is only sensitive to the projection of the absorption and emission dipole into the plane of the substrate. Consequently, because the h-BN flakes we investigated are often tilted relative to the substrate (see *Section 7.3*), the $\Delta\theta$ we measure can differ from the true dipole misalignment. Secondly, it is possible that direct and indirect absorption mechanisms may coexist. In this scenario $\theta_{emit}(E_{ZPL})$ is related to the true emission dipole orientation and $\theta_{abs}(E_{ZPL})$ is actually a weighted average over all absorption mechanisms. To test whether a particular ZPL may originate from two distinct mechanisms, we acquired spectrally-resolved polarization measurements using both 532 nm and 473 nm light for excitation. Figure 7.4a is a magnified view of a ZPL at ~577 nm excited using 532 nm (green trace) and 473 nm (blue trace) light, corresponding to energy shifts of ~182 meV and ~472 meV, respectively. The

two spectra overlap well, verifying that each wavelength may excite the same ZPL. In Figure 7.4b we plot $\theta_{emit}(E)$ (red trace), $\theta_{abs}(E)$ for 532 nm excitation (green trace), and $\theta_{abs}(E)$ for 473 nm excitation (blue trace). Incidentally, $\Delta\theta \approx 0°$ for 532 nm excitation and $\Delta\theta \approx 50°$ for 473 nm excitation. For this defect, the 532 nm excitation is well described by direct absorption whereas the 473 nm excitation is explained by indirect absorption. Therefore, a particular ZPL may be excited via multiple mechanisms.

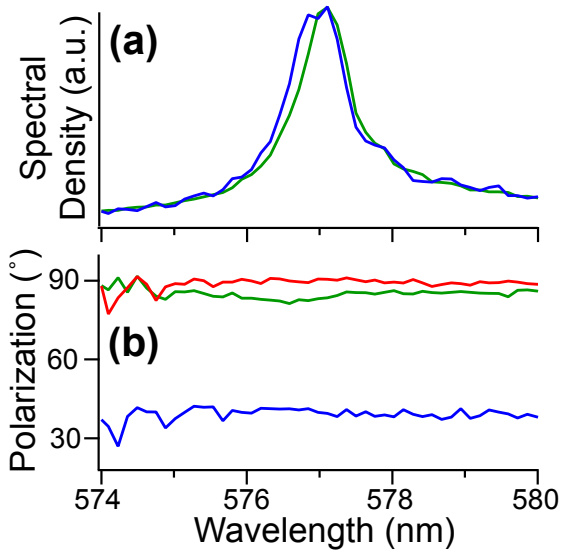

Figure 7.4: (a) Emission spectrum of a ZPL at ~577 nm excited with 473 nm (blue trace) and 532 nm (green trace) light indicating that both energies may excite the transition. (b) Spectrally resolved polarization measurements of $\theta_{abs}(E)$ for excitation with 532 nm light (green trace) and $\theta_{emit}(E)$ (red trace) reveal that $\Delta\theta(E_{ZPL}) \approx 0$. The analogous measurement using 473 nm excitation (blue trace) indicates a large misalignment between the 473 nm absorption dipole and the emission dipole.

In conclusion, we made polarization measurements of absorption and emission for 103 isolated defects in h-BN with ZPLs in the range ~550-740 nm. In contrast to the predictions of a Huang-Rhys model involving two electronic states, our survey reveals that the absorption and emission dipoles

are frequently misaligned. We frame the dipole misalignment $\Delta\theta$ in the context of the energy difference between a ZPL and the exciting light (ΔE), rather than the ZPL energy, and demonstrate that ΔE is a strong indicator of the likelihood that the absorption and emission dipoles will be parallel. In particular, if ΔE coincides with an allowed phonon energy in h-BN then $\Delta\theta \approx 0°$. Therefore, direct absorption mediated by the creation a single phonon is efficient and is well described by the Huang-Rhys model with two electronic states. Alternatively, if ΔE exceeds the maximum phonon energy in h-BN then $0° \leq \Delta\theta \leq 90°$. We propose a mechanism to explain these observations whereby a defect may be excited indirectly through a third intermediate electronic state. This mechanism is supported by polarization measurements acquired using 532 nm and 473 nm excitation, which reveal that multiple mechanisms may excite a particular ZPL. These comprehensive results form a key advance in our understanding of absorption and emission mechanisms in h-BN single defects.

7.3 Supplementary Information

7.3.1 Experimental Apparatus and Spectrally-Averaged Polarization Measurements

Figure 7.5 is a schematic of the house-built confocal microscope used in this work to study point defects in hexagonal boron nitride (h-BN). For steady-state measurements we use either a continuous wave (CW) 532 nm laser or a

CW 473 nm laser for excitation. For lifetime measurements (shown in *Section 7.3.4* below) we use a pulsed 532 nm laser with an 80 kHz repetition rate and a 350 ps pulse width. To create an arbitrary linear polarization state of the exciting light we use a fixed linear polarizer (FP1) followed by a rotatable half wave plate (HWP1). Between HWP1 and the 0.7 NA microscope objective (MO) the exciting light inherits a polarization-dependent retardance from elements in the optical path that both rotates the polarization state and reduces the extinction ratio. We compensate for these effects using a fixed wave plate (FWP1) selected to introduce an appropriate correcting retardance at 532 nm. To calibrate the polarization state of the excitation path we place a polarization analyzer in front of the MO and measure the polarization state of the exciting light for a series of positions of HWP1.

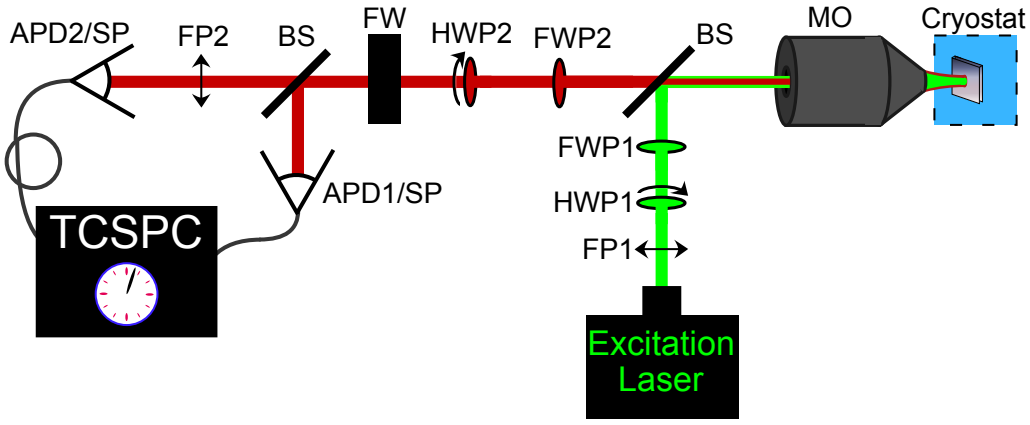

Figure 7.5: Schematic of confocal microscope used in this work.

Optically active defects may absorb the exciting light and emit photons that are collected by the MO. We use a beam splitter (BS), two single photon detectors (APDs), and a time correlated single photon counting module

(TCSPC) to measure the two-photon correlation function, $g^{(2)}(\tau)$, of the collected photons. Photons directed towards APD1 are detected independent of their polarization state. Thus we probe the spectrally averaged absorption dipole, $\langle\theta_{abs}\rangle$, by rotating HWP1 and monitoring the count rate on APD1. To determine the average polarization state of the collected photons we repeat the procedure used for absorption. We first correct for the wavelength- and polarization-dependent retardances of the collection path using FWP2. Next the polarization state of the collected photons is rotated by achromatic HWP2. Finally, the collected photons may pass through FP2 with a probability determined by their polarization state. Thus we probe the spectrally averaged emission dipole, $\langle\theta_{emit}\rangle$, by rotating HWP2 and monitoring the count rate on APD2. To calibrate the average polarization state of the collection path we direct 633 nm light from APD2 towards the MO, place a polarization analyzer in front of the MO, and measure the polarization state of the light for a series of positions of HWP2. For all measurements a particular zero-phonon line (ZPL) may be spectrally isolated by selecting an appropriate combination of long- and short-pass filters from the filter wheel (FW).

7.3.2 Spectrally-Resolved Polarization Measurements

In addition to the conventional, spectrally-averaged polarization measurements discussed in *Section 7.3.1,* we also performed spectrally-resolved polarization measurements for two primary reasons. First, because

the polarization state of the collection path is wavelength dependent, and because the distribution of zero-phonon line energies (E_{ZPL}) is broad, a spectrally-resolved calibration is essential to ensure the polarization state we measure for a particular ZPL energy faithfully represents the true polarization state. Secondly, because multiple distinct ZPLs may be simultaneously excited within the same h-BN flake, spectrally-resolved measurements are essential to properly distinguish the polarization properties of each ZPL. For the absorption measurement we rotate HWP1 and, rather than detect the light at APD1, we direct the light to a spectrometer (SP). For each position of HWP1 we record an emission spectrum to directly obtain $\tilde{I}_{abs}(\phi,\lambda)$, where $\tilde{I}_{abs}(\phi,\lambda)\delta\lambda$ is the number of photons collected in the wavelength range $(\lambda,\lambda+\delta\lambda)$ when HWP1 is oriented at an angle ϕ. We may convert $\tilde{I}_{abs}(\phi,\lambda)$ to $I_{abs}(\theta,E)$, where $I_{abs}(\theta,E)\delta E$ is the number of photons collected in the energy range $(E,E+\delta E)$ when the exciting light is polarized at angle θ, via the conversion $I_{abs}(\theta,E)\propto\lambda^2\tilde{I}_{abs}(\phi,\lambda)$. Note that for excitation measurements the calibration of *Section 7.3.1* may be used to convert ϕ to θ. At each fixed energy E' we fit $I_{abs}(\theta,E')$ to the function

$$A+B\cos^2\left[\frac{\pi}{180}(\theta-\theta_{abs}(E'))\right], \tag{7.4}$$

where $\theta_{abs}(E')$ is the energy-dependent orientation of the absorption dipole.

Figure 7.6 a is an emission spectrum of a h-BN flake revealing the presence of two sharp ZPLs separated by ~20 nm. A spectrally-averaged polarization measurement would produce $\langle\theta_{abs}\rangle$, which represents the

polarization state of the exciting light that maximizes the integrated fluorescence from both ZPLs. In contrast, a spectrally-resolved polarization measurement produces $\theta_{abs}(\lambda)$, which represents the polarization state of the exciting light that maximizes the spectral density at the wavelength λ. This measurement is shown in Figure 7.6b and verifies that the absorption dipole of each ZPL is misaligned.

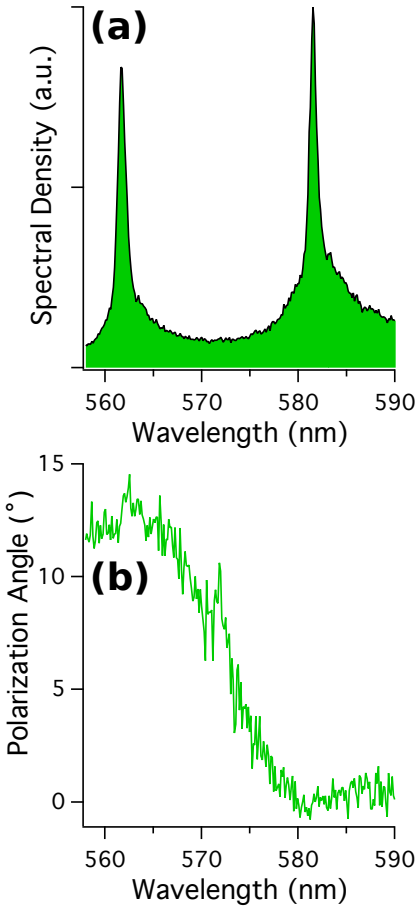

Figure 7.6: (a) Emission spectrum of a h-BN flake revealing the presence of two distinct ZPLs. (b) Measurement of $\theta_{abs}(\lambda)$ for the flake that produced the spectrum in (a). Evidently distinct ZPLs with distinct polarization properties may be simultaneously excited.

After measuring $\theta_{abs}(E)$ for a particular ZPL we may fix the polarization state of the exciting light to $\theta_{abs}(E_{ZPL})$ and measure $\tilde{I}_{emit}(\phi,\lambda)$ by recording an emission spectrum at each orientation of HWP2. Analogous to the absorption case, $\tilde{I}_{emit}(\phi,\lambda)\delta\lambda$ represents the number of photons detected in the energy range $(\lambda,\lambda+\delta\lambda)$ when HWP2 is oriented at angle ϕ. However, in contrast to the absorption case, because the retardances introduced by the collection path depend on both the wavelength and the polarization state of the emitted light, we can no longer use the spectrally-averaged calibration from *Section 7.3.1* to convert ϕ to θ. Consequently, to perform spectrally-resolved polarization measurements of emission we must apply a polarization- and wavelength-dependent calibration to ϕ to obtain $I_{emit}(\theta,E)$. To perform this calibration we place a broadband light source polarized at angle θ_{emit} at the objective and direct the light towards APD2. We then measure $\tilde{I}_{emit}(\phi,\lambda)$. In Figure 7.7a we plot $2\phi_{emit}(\lambda)-\theta_{emit}$ when the light source is polarized at angles $\theta_{emit}\in\{0°,30°,60°,90°,120°,150°\}$. Each trace represents the angular error one would obtain in a polarization measurement of photons with wavelength λ that were emitted with a true polarization angle of θ_{emit} if a wavelength- and polarization-dependent calibration were not implemented. Note that the magnitude of this error is minimized by using a BS, rather than a dichroic mirror, to combine the excitation and collection paths. In Figure 7.7b we plot the spectrally-resolved emission visibility V_{emit} of the microscope at each polarization angle θ_{emit}, where

$$V_{emit} = \frac{B}{B+2A}. \tag{7.5}$$

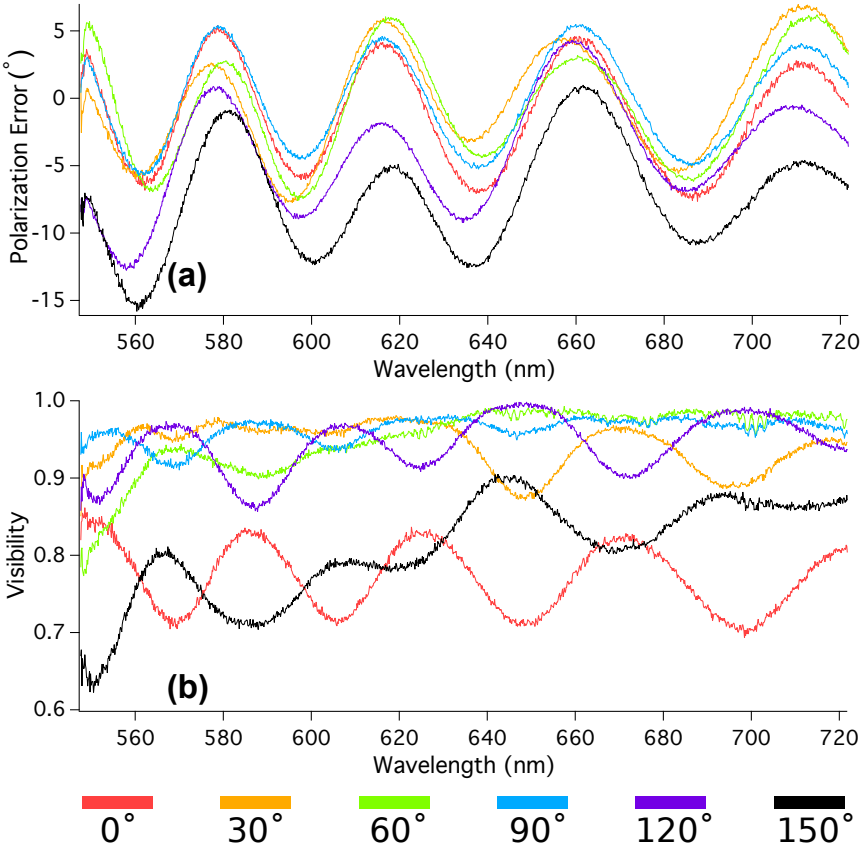

Figure 7.7: (a) Calibration of the polarization state of the collected light that accounts for the wavelength-dependent properties of the collection path when the emitted light is initially polarized at angle θ_{emit}. (b) Theoretical maximum measured visibility for light that is purely polarized at angle θ_{emit} when it exits the microscope objective. In both (a) and (b) traces corresponding to $\theta_{emit} \in \{0°, 30°, 60°, 90°, 120°, 150°\}$ are included.

7.3.3 Sample Details

The h-BN flakes we investigated are commercially available from Graphene Supermarket. The as-received flakes are suspended in a 50/50 water/ethanol solution. We drop cast 25 μL of solution onto a thermally oxidized silicon

substrate and anneal the samples at 850°C for 30 minutes under continuous nitrogen flow. We have previously characterized our samples via Raman spectroscopy and energy dispersive X-ray spectroscopy [3]. Figure 7.8a and b are two scanning electron microscopy (SEM) images of the as-prepared sample. Note that the flakes aggregate together and consequently many of the flakes are tilted with respect to the substrate.

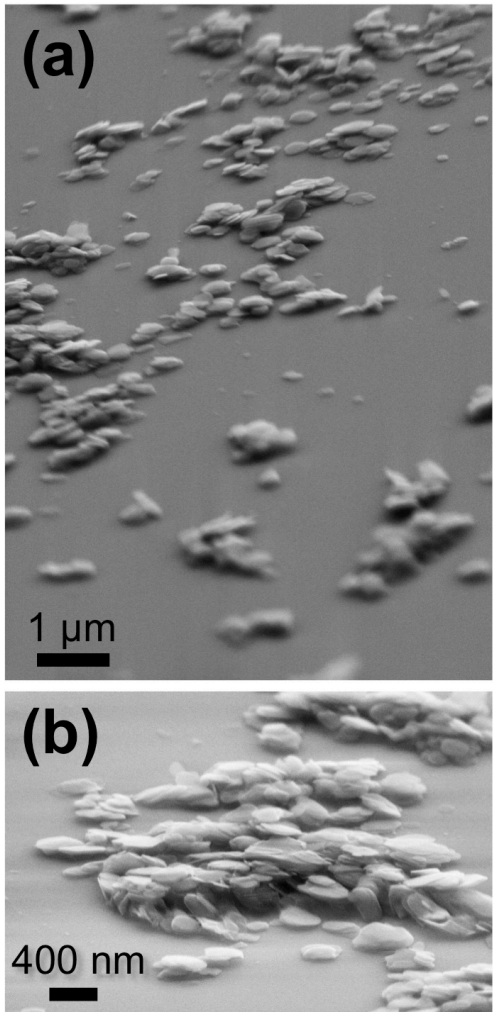

Figure 7.8: (a) SEM image of the prepared sample. (b) Magnified view of a cluster of h-BN flakes revealing multiple flake orientations.

The polarization measurements of θ_{abs} and θ_{emit} discussed in *Section 7.3.2* are only sensitive to the projection of the absorption and emission dipole, respectively, into the plane of the substrate. Consequently, the measured dipole misalignment angle $\Delta\theta = |\theta_{abs} - \theta_{emit}|$ may differ from the true misalignment angle. This effect may be offset by investigating h-BN samples with known orientation.

9.3.4 Lifetime Distribution

For 36 of the investigated emitters we also measured the lifetime of the excited state using pulsed excitation. Figure 7.9 is a scatter plot relating the ZPL wavelength to the excited state lifetime. Evidently most of the emitters investigated have a lifetime near 3 ns, but the excited state lifetime may be as low as 1.5 ns and as high as 8 ns.

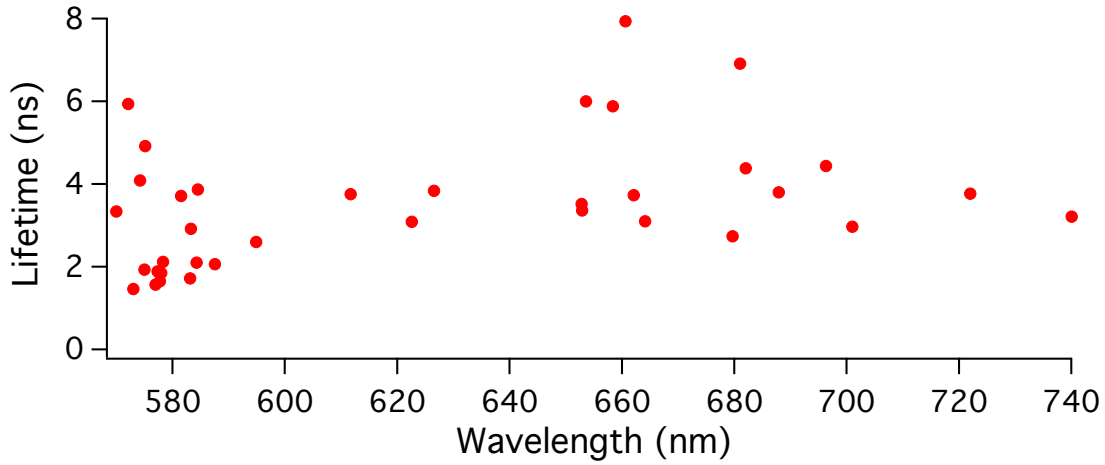

Figure 7.9: Scatter plot relating the ZPL wavelength to the excited state lifetime for 36 of the emitters investigated.

7.3.5 Visibility Distribution

In the main text we provided evidence that a single ZPL may be excited both via direct absorption and indirect absorption with the efficiency of each mechanism being determined by the laser energy being used. We anticipate the visibility of absorption and emission to be similar for a direct transition [2]. For an indirect transition, however, we anticipate the emission visibility to exceed the absorption visibility. Figure 7.10 is a scatter plot relating the absorption visibility and emission visibility for all the emitters investigated. Note that the emission visibilities have been corrected using the calibration shown in Figure 7.7b to more closely approximate their true values. The solid line is a plot of the function $y = x$. Consequently any points above the line have an emission visibility that exceeds the absorption visibility. The majority of data points lie above the solid line, in support of the mechanism proposed in the main text.

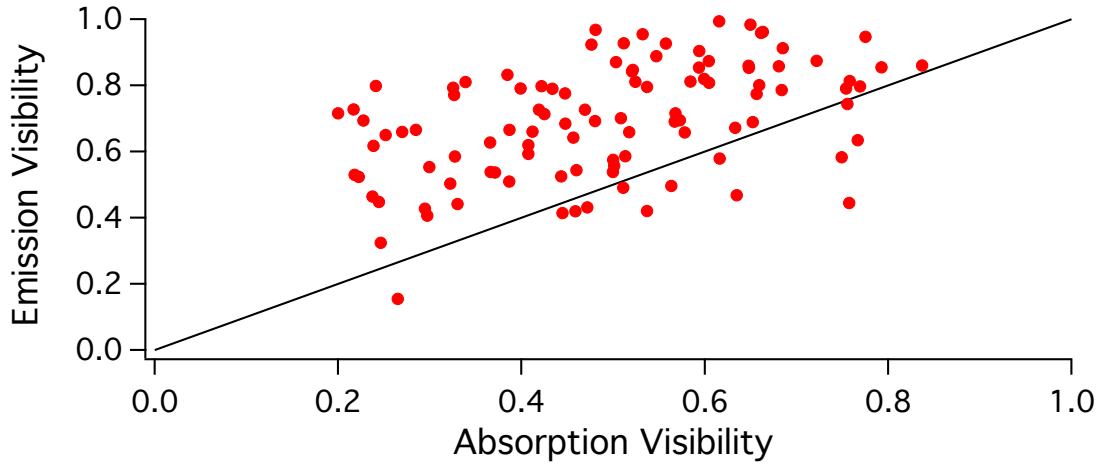

Figure 7.10: Scatter plot relating the absorption and emission visibilities for all defects investigated.

7.4 Acknowledgements

We thank Brian Calderon for acquiring SEM images of annealed h-BN flakes. Research support for *Chapter 7* was provided by the National Science Foundation (DMR-1254530). We acknowledge use of the Cornell NanoScale Facility, a member of the National Nanotechnology Coordinated Infrastructure (NNCI), which is supported by the National Science Foundation (Grant ECCS-15420819). Additionally, we acknowledge the Cornell Center for Materials Research Shared Facilities, which are supported through the NSF MRSEC program (DMR-1120296).

CHAPTER 8

CONCLUSION

Investigations seeking to discover defect-based single photon sources beyond the NV center have proven to be enormously fruitful over the last eight years. One theme of the single defects presented in this thesis is considerable defect-to-defect variation. For example, in contrast to NV centers, the ZPL energy of single defects in ZnO and hBN is highly variable and, in the case of hBN, can extend from the UV to the IR. This feature is suggestive of strong coupling to the local environment, which is promising for metrology or applications requiring defect properties to be tuned. On the other hand, defect-to-defect variation complicates direct comparison of observed defect properties with first-principles calculations, rendering it difficult to identify the structural origin of the defects being studied. As such, at the time of writing (2018) there remains no consensus as to the defect type(s) responsible for the single photon emission in ZnO or hBN.

A second theme of this thesis is identifying defect properties that are more or less immune from defect-to-defect variation and may therefore be directly compared with theoretical predictions. We highlight polarization spectroscopy measurements of absorption and emission. In the case of ZnO, despite the individual single-defect emission spectra being different, we found a single absorption and emission dipole aligned parallel to one another in all single defects observed. This observation is indicative of transitions between

orbital singlets, a property that may be directly compared with theoretical predictions. In the case of hBN, we observe a *misaligned* absorption and emission dipole. By comparing these observations with Huang-Rhys theory, we identified a third electronic energy level and found that optical transitions are strongly mediated by a single in-plane (2D) optical phonon. We also perform temperature-dependent measurements of ZPL linewidth in hBN. In this case a lattice vibration model identified a homogenous broadening mechanism resulting from coupling to in-plane (2D) acoustic phonons. Our results collectively illustrate the promise of single-defect investigations and highlight several techniques for identifying properties that are intrinsic to the defect type(s) being investigated.

REFERENCES

[1] N. R. Jungwirth, Y. Y. Pai, H. S. Chang, E. R. MacQuarrie, K. X. Nguyen, and G. D. Fuchs, J. Appl. Phys. **116**, 043509 (2014).

[2] N. R. Jungwirth, H.-S. Chang, M. Jiang, and G. D. Fuchs, ACS Nano **10**, 1210 (2016).

[3] N. R. Jungwirth, B. Calderon, Y. Ji, M. G. Spencer, M. E. Flatté, and G. D. Fuchs, Nano Lett. **16**, 6052 (2016).

[4] N. R. Jungwirth and G. D. Fuchs, Phys. Rev. Lett. **119**, (2017).

[5] C. A. Coulson and M. J. Kearsley, Proc. R. Soc. Math. Phys. Eng. Sci. **241**, 433 (1957).

[6] J. Walker, Rep Prog Phys **42**, 1605 (1979).

[7] M. E. Thomas and W. J. Tropf, Johns Hopkins APL Tech. Dig. **14**, (1993).

[8] R. J. Elliott, I. G. Matthew, and E. W. J. Mitchell, Philos. Mag. **3**, 360 (1958).

[9] E. Barkai, Y. Jung, and R. Silbey, Annu. Rev. Phys. Chem. **55**, 457 (2004).

[10] T. Basché, *Single-Molecule Optical Detection, Imaging and Spectroscopy* (VCH, Weinheim; Cambridge, 1997).

[11] A. Gruber, A. Dräbenstedt, C. Tietz, L. Fleury, J. Wrachtrup, and C. Von Borczyskowski, Science **276**, 2012 (1997).

[12] C. Kurtsiefer, S. Mayer, P. Zarda, and H. Weinfurter, Phys. Rev. Lett. **85**, 290 (2000).

[13] M. W. Doherty, N. B. Manson, P. Delaney, F. Jelezko, J. Wrachtrup, and L. C. L. Hollenberg, Phys. Rep. **528**, 1 (2013).

[14] V. V. Dobrovitski, G. D. Fuchs, A. L. Falk, C. Santori, and D. D. Awschalom, Annu. Rev. Condens. Matter Phys. **4**, 23 (2013).

[15] J. M. Taylor, P. Cappellaro, L. Childress, L. Jiang, D. Budker, P. R. Hemmer, A. Yacoby, R. Walsworth, and M. D. Lukin, Nat. Phys. **4**, 810 (2008).

[16] P. Maletinsky, S. Hong, M. S. Grinolds, B. Hausmann, M. D. Lukin, R. L. Walsworth, M. Loncar, and A. Yacoby, Nat. Nanotechnol. **7**, 320 (2012).

[17] G. Kucsko, P. C. Maurer, N. Y. Yao, M. Kubo, H. J. Noh, P. K. Lo, H. Park, and M. D. Lukin, Nature **500**, 54 (2013).

[18] D. M. Toyli, C. F. de las Casas, D. J. Christle, V. V. Dobrovitski, and D. D. Awschalom, Proc. Natl. Acad. Sci. **110**, 8417 (2013).

[19] F. Dolde, H. Fedder, M. W. Doherty, T. Nöbauer, F. Rempp, G. Balasubramanian, T. Wolf, F. Reinhard, L. C. L. Hollenberg, F. Jelezko, and J. Wrachtrup, Nat Phys **7**, 459 (2011).

[20] J. R. Weber, W. F. Koehl, J. B. Varley, A. Janotti, B. B. Buckley, C. G. Van de Walle, and D. D. Awschalom, Proc. Natl. Acad. Sci. **107**, 8513 (2010).

[21] D. A. Simpson, E. Ampem-Lassen, B. C. Gibson, S. Trpkovski, F. M. Hossain, S. T. Huntington, A. D. Greentree, L. C. L. Hollenberg, and S. Prawer, Appl. Phys. Lett. **94**, 203107 (2009).

[22] E. Neu, C. Hepp, M. Hauschild, S. Gsell, M. Fischer, H. Sternschulte, D. Steinmüller-Nethl, M. Schreck, and C. Becher, New J. Phys. **15**, 043005 (2013).

[23] E. Neu, M. Fischer, S. Gsell, M. Schreck, and C. Becher, Phys. Rev. B **84**, (2011).

[24] M. Widmann, S.-Y. Lee, T. Rendler, N. T. Son, H. Fedder, S. Paik, L.-P. Yang, N. Zhao, S. Yang, I. Booker, A. Denisenko, M. Jamali, S. A. Momenzadeh, I. Gerhardt, T. Ohshima, A. Gali, E. Janzén, and J. Wrachtrup, Nat. Mater. **14**, 164 (2014).

[25] S. Castelletto, B. C. Johnson, V. Ivády, N. Stavrias, T. Umeda, A. Gali, and T. Ohshima, Nat. Mater. (2013).

[26] D. J. Christle, A. L. Falk, P. Andrich, P. V. Klimov, J. U. Hassan, N. T. Son, E. Janzén, T. Ohshima, and D. D. Awschalom, Nat. Mater. **14**, 160 (2014).

[27] B. Lienhard, T. Schröder, S. Mouradian, F. Dolde, T. T. Tran, I. Aharonovich, and D. Englund, Optica **3**, 768 (2016).

[28] F. Fuchs, B. Stender, M. Trupke, D. Simin, J. Pflaum, V. Dyakonov, and G. V. Astakhov, Nat. Commun. **6**, 7578 (2015).

[29] A. Lohrmann, B. C. Johnson, J. C. McCallum, and S. Castelletto, Rep. Prog. Phys. **80**, 034502 (2017).

[30] A. J. Morfa, B. C. Gibson, M. Karg, T. J. Karle, A. D. Greentree, P. Mulvaney, and S. Tomljenovic-Hanic, Nano Lett. **12**, 949 (2012).

[31] S. Choi, B. C. Johnson, S. Castelletto, C. Ton-That, M. R. Phillips, and I. Aharonovich, Appl. Phys. Lett. **104**, 261101 (2014).

[32] S. Ghosh, M. Ghosh, M. Seibt, and G. Mohan Rao, Nanoscale **8**, 2632 (2016).

[33] O. Neitzke, A. Morfa, J. Wolters, A. W. Schell, G. Kewes, and O. Benson, Nano Lett. **15**, 3024 (2015).

[34] A. M. Berhane, K.-Y. Jeong, Z. Bodrog, S. Fiedler, T. Schröder, N. V. Triviño, T. Palacios, A. Gali, M. Toth, D. Englund, and I. Aharonovich, Adv. Mater. 1605092 (2017).

[35] M. Koperski, K. Nogajewski, A. Arora, V. Cherkez, P. Mallet, J.-Y. Veuillen, J. Marcus, P. Kossacki, and M. Potemski, Nat. Nanotechnol. **10**, 503 (2015).

[36] Y.-M. He, G. Clark, J. R. Schaibley, Y. He, M.-C. Chen, Y.-J. Wei, X. Ding, Q. Zhang, W. Yao, X. Xu, C.-Y. Lu, and J.-W. Pan, Nat. Nanotechnol. **10**, 497 (2015).

[37] C. Chakraborty, L. Kinnischtzke, K. M. Goodfellow, R. Beams, and A. N. Vamivakas, Nat. Nanotechnol. **10**, 507 (2015).

[38] T. T. Tran, S. Choi, J. A. Scott, Z. Xu, C. Zheng, G. Seniutinas, A. Bendavid, M. S. Fuhrer, M. Toth, and I. Aharonovich, ArXiv Prepr. ArXiv170100041 (2016).

[39] T. T. Tran, K. Bray, M. J. Ford, M. Toth, and I. Aharonovich, Nat. Nanotechnol. **11**, 37 (2015).

[40] T. T. Tran, C. Elbadawi, D. Totonjian, C. J. Lobo, G. Grosso, H. Moon, D. R. Englund, M. J. Ford, I. Aharonovich, and M. Toth, ACS Nano (2016).

[41] Z. Shotan, H. Jayakumar, C. R. Considine, M. Mackoit, H. Fedder, J. Wrachtrup, A. Alkauskas, M. W. Doherty, V. M. Menon, and C. A. Meriles, ACS Photonics **3**, 2490 (2016).

[42] L. J. Martínez, T. Pelini, V. Waselowski, J. R. Maze, B. Gil, G. Cassabois, and V. Jacques, Phys. Rev. B **94**, 121405 (2016).

[43] N. Chejanovsky, M. Rezai, F. Paolucci, Y. Kim, T. Rendler, W. Rouabeh, F. Fávaro de Oliveira, P. Herlinger, A. Denisenko, S. Yang, I. Gerhardt, A. Finkler, J. H. Smet, and J. Wrachtrup, Nano Lett. **16**, 7037 (2016).

[44] A. W. Schell, T. T. Tran, H. Takashima, S. Takeuchi, and I. Aharonovich, APL Photonics **1**, 091302 (2016).

[45] G. Grosso, H. Moon, B. Lienhard, S. Ali, D. K. Efetov, M. M. Furchi, P. Jarillo-Herrero, M. J. Ford, I. Aharonovich, and D. Englund, ArXiv Prepr. ArXiv161103515 (2016).

[46] A. W. Schell, H. Takashima, T. T. Tran, I. Aharonovich, and S. Takeuchi, ArXiv Prepr. ArXiv170102696 (2017).

[47] M. Kianinia, B. Regan, S. A. Tawfik, T. T. Tran, M. J. Ford, I. Aharonovich, and M. Toth, ACS Photonics (2017).

[48] A. L. Exarhos, D. A. Hopper, R. R. Grote, A. Alkauskas, and L. C. Bassett, ACS Nano **11**, 3328 (2017).

[49] T. T. Tran, D. Wang, Z.-Q. Xu, A. Yang, M. Toth, T. W. Odom, and I. Aharonovich, Nano Lett. (2017).

[50] R. Bourrellier, S. Meuret, A. Tararan, O. Stéphan, M. Kociak, L. H. G. Tizei, and A. Zobelli, Nano Lett. **16**, 4317 (2016).

[51] M. Abdi, M.-J. Hwang, M. Aghtar, and M. B. Plenio, ArXiv Prepr. ArXiv170400638 (2017).

[52] O. Arı, N. Polat, Ö. Çakır, and S. Ates, ArXiv Prepr. ArXiv180810611 (2018).

[53] A. Dietrich, M. Bürk, E. S. Steiger, L. Antoniuk, T. T. Tran, M. Nguyen, I. Aharonovich, F. Jelezko, and A. Kubanek, Phys. Rev. B **98**, (2018).

[54] A. L. Exarhos, D. A. Hopper, R. N. Patel, M. W. Doherty, and L. C. Bassett, ArXiv Prepr. ArXiv180409061 (2018).

[55] Y. Xue, H. Wang, Q. Tan, J. Zhang, T. Yu, K. Ding, D. Jiang, X. Dou, J. Shi, and B. Sun, ACS Nano **12**, 7127 (2018).

[56] N. V. Proscia, Z. Shotan, H. Jayakumar, P. Reddy, M. Dollar, A. Alkauskas, M. Doherty, C. A. Meriles, and V. M. Menon, ArXiv Prepr. ArXiv171201352 (2017).

[57] Z.-Q. Xu, C. Elbadawi, T. T. Tran, M. Kianinia, X. Li, D. Liu, T. B. Hoffman, M. Nguyen, S. Kim, and J. H. Edgar, ArXiv Prepr. ArXiv171007010 (2017).

[58] M. Feldman, A. Puretzky, L. Lindsay, E. Tucker, D. Briggs, P. Evans, R. Haglund, and B. Lawrie, ArXiv Prepr. ArXiv180807119 (2018).

[59] G. Noh, D. Choi, J.-H. Kim, D.-G. Im, Y.-H. Kim, H. Seo, and J. Lee, Nano Lett. (2018).

[60] R. J. Glauber, Phys. Rev. **130**, 2529 (1963).

[61] D. Stoler, Phys. Rev. Lett. **33**, 1397 (1974).

[62] H. J. Kimble, M. Dagenais, and L. Mandel, Phys. Rev. Lett. **39**, 691 (1977).

[63] I. S. Osad'ko, J. Exp. Theor. Phys. **86**, 875 (1998).

[64] A. Molski, J. Hofkens, T. Gensch, N. Boens, and F. D. Schryver, Chem. Phys. Lett. **318**, 325 (2000).

[65] Y. Jung, E. Barkai, and R. J. Silbey, J. Chem. Phys. **117**, 10980 (2002).

[66] W. E. Moerner and D. P. Fromm, Rev. Sci. Instrum. **74**, 3597 (2003).

[67] T. Basché, W. E. Moerner, M. Orrit, and H. Talon, Phys. Rev. Lett. **69**, 1516 (1992).

[68] U. Özgür, Y. I. Alivov, C. Liu, A. Teke, M. A. Reshchikov, S. Doğan, V. Avrutin, S.-J. Cho, and H. Morkoç, J. Appl. Phys. **98**, 041301 (2005).

[69] J. C. Fan, K. M. Sreekanth, Z. Xie, S. L. Chang, and K. V. Rao, Prog. Mater. Sci. **58**, 874 (2013).

[70] Z. L. Wang, J. Phys. Condens. Matter **16**, R829 (2004).

[71] Y. S. Park, M. Seo, J. Yi, D. Lim, and J. Lee, Thin Solid Films **547**, 47 (2013).

[72] J.-H. Yun, J. Kim, Y. C. Park, S.-J. Moon, and W. A. Anderson, Thin Solid Films **547**, 17 (2013).

[73] W. J. Beek, M. M. Wienk, and R. A. Janssen, Adv. Mater. **16**, 1009 (2004).

[74] M. Thambidurai, J. Y. Kim, C. Kang, N. Muthukumarasamy, H.-J. Song, J. Song, Y. Ko, D. Velauthapillai, and C. Lee, Renew. Energy **66**, 433 (2014).

[75] W. J. E. Beek, M. M. Wienk, and R. A. J. Janssen, Adv. Funct. Mater. **16**, 1112 (2006).

[76] L. Whittaker-Brooks, J. M. Mativetsky, A. Woll, D. Smilgies, and Y.-L. Loo, Org. Electron. **14**, 3477 (2013).

[77] C.-T. Wang, S.-H. Ro, C.-S. Jao, M.-K. Tsai, and S.-Y. Yang, J. Non-Cryst. Solids **356**, 873 (2010).

[78] K. Ramanathan, M. A. Contreras, C. L. Perkins, S. Asher, F. S. Hasoon, J. Keane, D. Young, M. Romero, W. Metzger, and R. Noufi, Prog. Photovolt. Res. Appl. **11**, 225 (2003).

[79] C. G. Van de Walle, Phys. B Condens. Matter **308**, 899 (2001).

[80] F. Oba, S. R. Nishitani, S. Isotani, H. Adachi, and I. Tanaka, J. Appl. Phys. **90**, 824 (2001).

[81] P. Erhart, K. Albe, and A. Klein, Phys. Rev. B **73**, (2006).

[82] A. F. Kohan, G. Ceder, D. Morgan, and C. G. Van de Walle, Phys. Rev. B **61**, 15019 (2000).

[83] C. G. Van de Walle, Phys. Rev. Lett. **85**, 1012 (2000).

[84] S. Zhang, S.-H. Wei, and A. Zunger, Phys. Rev. B **63**, (2001).

[85] A. Janotti and C. G. Van de Walle, Phys. Rev. B **76**, (2007).

[86] C. H. Park, S. B. Zhang, and S.-H. Wei, Phys. Rev. B **66**, (2002).

[87] X. J. Wang, L. S. Vlasenko, S. J. Pearton, W. M. Chen, and I. A. Buyanova, J. Phys. Appl. Phys. **42**, 175411 (2009).

[88] S. Orlinskii, J. Schmidt, P. Baranov, D. Hofmann, C. de Mello Donegá, and A. Meijerink, Phys. Rev. Lett. **92**, (2004).

[89] M. C. Tarun, M. Z. Iqbal, and M. D. McCluskey, AIP Adv. **1**, 022105 (2011).

[90] B. Lin, Z. Fu, and Y. Jia, Appl. Phys. Lett. **79**, 943 (2001).

[91] Y. Chen, D. M. Bagnall, Z. Zhu, T. Sekiuchi, K. Park, K. Hiraga, T. Yao, S. Koyama, M. Y. Shen, and T. Goto, J. Cryst. Growth **181**, 165 (1997).

[92] K. Vanheusden, C. H. Seager, W. L. Warren, D. R. Tallant, and J. A. Voigt, Appl. Phys. Lett. **68**, 403 (1996).

[93] V. A. Nikitenko, J. Appl. Spectrosc. **57**, 783 (1992).

[94] F. Leiter, H. Zhou, F. Henecker, A. Hofstaetter, D. M. Hofmann, and B. K. Meyer, Phys. B Condens. Matter **308**, 908 (2001).

[95] A. B. Djurišić, W. C. H. Choy, V. A. L. Roy, Y. H. Leung, C. Y. Kwong, K. W. Cheah, T. K. Gundu Rao, W. K. Chan, H. Fei Lui, and C. Surya, Adv. Funct. Mater. **14**, 856 (2004).

[96] S. A. M. Lima, F. A. Sigoli, M. Jafelicci Jr, and M. R. Davolos, Int. J. Inorg. Mater. **3**, 749 (2001).

[97] A. B. Djurišić and Y. H. Leung, Small **2**, 944 (2006).

[98] N. T. Son, I. G. Ivanov, A. Kuznetsov, B. G. Svensson, Q. X. Zhao, M. Willander, N. Morishita, T. Ohshima, H. Itoh, J. Isoya, E. Janzén, and R. Yakimova, J. Appl. Phys. **102**, 093504 (2007).

[99] V. A. Nikitenko, K. Tarkpea, A. I. Tereshchenko, and I. P. Kuz'mina, J. Appl. Spectrosc. **51**, 986 (1989).

[100] O. F. Schirmer and D. Zwingel, Solid State Commun. **8**, 1559 (1970).

[101] A. B. Djurišić, Y. H. Leung, K. H. Tam, Y. F. Hsu, L. Ding, W. K. Ge, Y. C. Zhong, K. S. Wong, W. K. Chan, H. L. Tam, K. W. Cheah, W. M. Kwok, and D. L. Phillips, Nanotechnology **18**, 095702 (2007).

[102] K. Vanheusden, W. L. Warren, C. H. Seager, D. R. Tallant, J. A. Voigt, and B. E. Gnade, J. Appl. Phys. **79**, 7983 (1996).

[103] A. L. Taylor, G. Filipovich, and G. K. Lindeberg, Solid State Commun. **8**, 1359 (1970).

[104] D. Hofmann, A. Hofstaetter, F. Leiter, H. Zhou, F. Henecker, B. Meyer, S. Orlinskii, J. Schmidt, and P. Baranov, Phys. Rev. Lett. **88**, 045504 (2002).

[105] W. E. Carlos, E. R. Glaser, and D. C. Look, Phys. B Condens. Matter **308**, 976 (2001).

[106] L. Vlasenko and G. Watkins, Phys. Rev. B **72**, 035203 (2005).

[107] L. Vlasenko and G. Watkins, Phys. Rev. B **71**, 125210 (2005).

[108] S. Nie and R. N. Zare, Annu. Rev. Biophys. Biomol. Struct. **26**, 567 (1997).

[109] X. S. Xie and J. K. Trautman, Annu. Rev. Phys. Chem. **49**, 441 (1998).

[110] Acc. Chem. Res. **29**, (n.d.).

[111] P. Tamarat, A. Maali, B. Lounis, and M. Orrit, J. Phys. Chem. A **104**, 1 (2000).

[112] T. Plakhotnik, E. A. Donley, and U. P. Wild, Annu. Rev. Phys. Chem. **48**, 181 (1997).

[113] S. Weiss, Science **283**, 1676 (1999).

[114] G. D. Fuchs, G. Burkard, P. V. Klimov, and D. D. Awschalom, Nat. Phys. **7**, 789 (2011).

[115] F. Jelezko, T. Gaebel, I. Popa, A. Gruber, and J. Wrachtrup, Phys. Rev. Lett. **92**, 076401 (2004).

[116] L. Childress, M. V. Gurudev Dutt, J. M. Taylor, A. S. Zibrov, F. Jelezko, J. Wrachtrup, P. R. Hemmer, and M. D. Lukin, Science **314**, 281 (2006).

[117] H. Bernien, B. Hensen, W. Pfaff, G. Koolstra, M. S. Blok, L. Robledo, T. H. Taminiau, M. Markham, D. J. Twitchen, L. Childress, and R. Hanson, Nature **497**, 86 (2013).

[118] J. R. Maze, P. L. Stanwix, J. S. Hodges, S. Hong, J. M. Taylor, P. Cappellaro, L. Jiang, M. V. G. Dutt, E. Togan, A. S. Zibrov, A. Yacoby, R. L. Walsworth, and M. D. Lukin, Nature **455**, 644 (2008).

[119] J. R. Maze, A. Gali, E. Togan, Y. Chu, A. Trifonov, E. Kaxiras, and M. D. Lukin, New J. Phys. **13**, 025025 (2011).

[120] S. J. Pearton, D. P. Norton, K. Ip, Y. W. Heo, and T. Steiner, Superlattices Microstruct. **34**, 3 (2003).

[121] S. Pearton, Prog. Mater. Sci. **50**, 293 (2005).

[122] J. R. Weber, W. F. Koehl, J. B. Varley, A. Janotti, B. B. Buckley, C. G. Van de Walle, and D. D. Awschalom, J. Appl. Phys. **109**, 102417 (2011).

[123] W. F. Koehl, B. B. Buckley, F. J. Heremans, G. Calusine, and D. D. Awschalom, Nature **479**, 84 (2011).

[124] S. T. Pantelides, *Deep Centers in Semiconductors: A State-of-the-Art Approach* (CRC Press, 1992).

[125] J. Bourgoin and M. Lannoo, *Point Defects in Semiconductors: Experimental Aspects* (Springer-Verlag, 1983).

[126] M. Lannoo and J. Bourgoin, *Point Defects in Semiconductors: Theoretical Aspects* (Springer-Verlag, 1981).

[127] W. P. Ambrose, T. Basché, and W. E. Moerner, J. Chem. Phys. **95**, 7150 (1991).

[128] W. P. Ambrose and W. E. Moerner, Nature **349**, 225 (n.d.).

[129] W.-T. Yip, D. Hu, J. Yu, D. A. Vanden Bout, and P. F. Barbara, J. Phys. Chem. A **102**, 7564 (1998).

[130] J. Schuster, F. Cichos, and C. Von Borczyskowski, Opt. Spectrosc. **98**, 712 (2005).

[131] F. Cichos, J. Martin, and C. von Borczyskowski, Phys. Rev. B **70**, 115314 (2004).

[132] M. Vogel, A. Gruber, J. Wrachtrup, and C. Borczyskowski, J. Phys. Chem. **99**, 14915 (1995).

[133] T. Basché and S. Kummer, Nature **373**, 132 (1995).

[134] A. C. J. Brouwer, E. J. J. Groenen, and J. Schmidt, Phys. Rev. Lett. **80**, 3944 (1998).

[135] I. S. Osad'ko, J. Exp. Theor. Phys. **89**, 513 (1999).

[136] M. B. Plenio and P. L. Knight, Rev. Mod. Phys. **70**, 101 (1998).

[137] M. Lippitz, F. Kulzer, and M. Orrit, ChemPhysChem **6**, 770 (2005).

[138] C. Bradac, T. Gaebel, N. Naidoo, M. J. Sellars, J. Twamley, L. J. Brown, A. S. Barnard, T. Plakhotnik, A. V. Zvyagin, and J. R. Rabeau, Nat. Nanotechnol. **5**, 345 (2010).

[139] W. E. Moerner, Science **277**, 1059 (1997).

[140] P. Frantsuzov, M. Kuno, B. Jankó, and R. A. Marcus, Nat. Phys. **4**, 519 (2008).

[141] K. Shimizu, R. Neuhauser, C. Leatherdale, S. Empedocles, W. Woo, and M. Bawendi, Phys. Rev. B **63**, 205316 (2001).

[142] B. Bruhn, J. Valenta, F. Sangghaleh, and J. Linnros, Nano Lett. **11**, 5574 (2011).

[143] M. Kuno, D. Fromm, S. Johnson, A. Gallagher, and D. Nesbitt, Phys. Rev. B **67**, 125304 (2003).

[144] M. Kuno, D. P. Fromm, H. F. Hamann, A. Gallagher, and D. J. Nesbitt, J. Chem. Phys. **112**, 3117 (2000).

[145] M. Haase, C. G. Hübner, E. Reuther, A. Herrmann, K. Müllen, and T. Basché, J. Phys. Chem. B **108**, 10445 (2004).

[146] R. M. Dickson, A. B. Cubitt, R. Y. Tsien, and W. E. Moerner, Nature **388**, 355 (1997).

[147] J. P. Hoogenboom, J. Hernando, E. M. H. P. van Dijk, N. F. van Hulst, and M. F. García-Parajó, ChemPhysChem **8**, 823 (2007).

[148] T. Ha, T. Enderle, D. S. Chemla, P. R. Selvin, and S. Weiss, Chem. Phys. Lett. **271**, 1 (1997).

[149] J. A. Veerman, M. F. Garcia-Parajo, L. Kuipers, and N. F. Van Hulst, Phys. Rev. Lett. **83**, 2155 (1999).

[150] R. Verberk, A. van Oijen, and M. Orrit, Phys. Rev. B **66**, (2002).

[151] C. Bradac, T. Gaebel, C. I. Pakes, J. M. Say, A. V. Zvyagin, and J. R. Rabeau, Small **9**, 132 (2013).

[152] N. Aslam, G. Waldherr, P. Neumann, F. Jelezko, and J. Wrachtrup, New J. Phys. **15**, 013064 (2013).

[153] C. Galland, Y. Ghosh, A. Steinbrück, M. Sykora, J. A. Hollingsworth, V. I. Klimov, and H. Htoon, Nature **479**, 203 (2011).

[154] A. L. Efros and M. Rosen, Phys. Rev. Lett. **78**, 1110 (1997).

[155] M. Nirmal, B. O. Dabbousi, M. G. Bawendi, J. J. Macklin, J. K. Trautman, T. D. Harris, and L. E. Brus, Nature **383**, 802 (1996).

[156] W.-T. Chang, Y.-C. Chen, K.-S. Kao, Y.-H. Chu, and C.-C. Cheng, Thin Solid Films **529**, 39 (2013).

[157] R. Ghosh, G. K. Paul, and D. Basak, Mater. Res. Bull. **40**, 1905 (2005).

[158] J.-H. Lee, K.-H. Ko, and B.-O. Park, J. Cryst. Growth **247**, 119 (2003).

[159] A. J. Morfa, G. Beane, B. Mashford, B. Singh, E. Della Gaspera, A. Martucci, and P. Mulvaney, J. Phys. Chem. C **114**, 19815 (2010).

[160] H. Ko, W.-P. Tai, K.-C. Kim, S.-H. Kim, S.-J. Suh, and Y.-S. Kim, J. Cryst. Growth **277**, 352 (2005).

[161] W. J. E. Beek, M. M. Wienk, M. Kemerink, X. Yang, and R. A. J. Janssen, J. Phys. Chem. B **109**, 9505 (2005).

[162] S. J. Kang and Y. H. Joung, Appl. Surf. Sci. **253**, 7330 (2007).

[163] B.-Y. Oh, M.-C. Jeong, and J.-M. Myoung, Appl. Surf. Sci. **253**, 7157 (2007).

[164] W. Beyer, J. Hüpkes, and H. Stiebig, Thin Solid Films **516**, 147 (2007).

[165] L. Znaidi, Mater. Sci. Eng. B **174**, 18 (2010).

[166] D. C. Look, Mater. Sci. Eng. B **80**, 383 (2001).

[167] A. M. Stoneham, *Theory of Defects in Solids: Electronic Structure of Defects in Insulators and Semiconductors* (OUP, Oxford, 2001).

[168] P. R. Bevington and Robinson, *Data Reduction and Error Analysis for the Physical Sciences* (McGraw-Hill, Boston, 2003).

[169] F. A. Inam, A. M. Edmonds, M. J. Steel, and S. Castelletto, Appl. Phys. Lett. **102**, 253109 (2013).

[170] F. A. Inam, M. D. W. Grogan, M. Rollings, T. Gaebel, J. M. Say, C. Bradac, T. A. Birks, W. J. Wadsworth, S. Castelletto, J. R. Rabeau, and M. J. Steel, ACS Nano **7**, 3833 (2013).

[171] A. Mohtashami and A. Femius Koenderink, New J. Phys. **15**, 043017 (2013).

[172] C. H. Crouch, O. Sauter, X. Wu, R. Purcell, C. Querner, M. Drndic, and M. Pelton, Nano Lett. **10**, 1692 (2010).

[173] O. Naaman and J. Aumentado, Phys. Rev. Lett. **96**, (2006).

[174] J. L. Lyons, D. Steiauf, A. Alkauskas, A. Janotti, and C. G. Van de Walle, in *Bull. Am. Phys. Soc.* (American Physical Society, 2013).

[175] A. Alkauskas, J. L. Lyons, D. Steiauf, and C. G. Van de Walle, Phys. Rev. Lett. **109**, 267401 (2012).

[176] C. Santori, M. Pelton, G. Solomon, Y. Dale, and Y. Yamamoto, Phys. Rev. Lett. **86**, 1502 (2001).

[177] F. De Martini, G. Di Giuseppe, and M. Marrocco, Phys. Rev. Lett. **76**, 900 (1996).

[178] A. Kuhn, M. Hennrich, and G. Rempe, Phys. Rev. Lett. **89**, (2002).

[179] B. Darquié, M. P. Jones, J. Dingjan, J. Beugnon, S. Bergamini, Y. Sortais, G. Messin, A. Browaeys, and P. Grangier, Science **309**, 454 (2005).

[180] M. D. Eisaman, J. Fan, A. Migdall, and S. V. Polyakov, Rev. Sci. Instrum. **82**, 071101 (2011).

[181] S. Francoeur, J. F. Klem, and A. Mascarenhas, Phys. Rev. Lett. **93**, (2004).

[182] R. Brouri, A. Beveratos, J.-P. Poizat, and P. Grangier, Opt. Lett. **25**, 1294 (2000).

[183] A. Beveratos, R. Brouri, T. Gacoin, A. Villing, J.-P. Poizat, and P. Grangier, Phys. Rev. Lett. **89**, (2002).

[184] E. Neu, M. Fischer, S. Gsell, M. Schreck, and C. Becher, Phys. Rev. B **84**, (2011).

[185] E. Neu, M. Agio, and C. Becher, Opt. Express **20**, 19956 (2012).

[186] M. Leifgen, T. Schröder, F. Gädeke, R. Riemann, V. Métillon, E. Neu, C. Hepp, C. Arend, C. Becher, K. Lauritsen, and O. Benson, New J. Phys. **16**, 023021 (2014).

[187] C. Hepp, T. Müller, V. Waselowski, J. N. Becker, B. Pingault, H. Sternschulte, D. Steinmüller-Nethl, A. Gali, J. R. Maze, M. Atatüre, and C. Becher, Phys. Rev. Lett. **112**, (2014).

[188] S. Choi, B. C. Johnson, S. Castelletto, C. Ton-That, M. R. Phillips, and I. Aharonovich, Appl. Phys. Lett. **104**, 261101 (2014).

[189] S. Choi, A. M. Berhane, A. Gentle, C. Ton-That, M. R. Phillips, and I. Aharonovich, ACS Appl. Mater. Interfaces **7**, 5619 (2015).

[190] Z. C. Tu and X. Hu, Phys. Rev. B **74**, (2006).

[191] J. G. E. Gardeniers, Z. M. Rittersma, and G. J. Burger, J. Appl. Phys. **83**, 7844 (1998).

[192] H. J. Fan, W. Lee, R. Hauschild, M. Alexe, G. Le Rhun, R. Scholz, A. Dadgar, K. Nielsch, H. Kalt, A. Krost, M. Zacharias, and U. Gösele, Small **2**, 561 (2006).

[193] E. R. MacQuarrie, T. A. Gosavi, A. M. Moehle, N. R. Jungwirth, S. A. Bhave, and G. D. Fuchs, Optica **2**, 233 (2015).

[194] M. Willander, O. Nur, Q. X. Zhao, L. L. Yang, M. Lorenz, B. Q. Cao, J. Zúñiga Pérez, C. Czekalla, G. Zimmermann, M. Grundmann, A. Bakin, A. Behrends, M. Al-Suleiman, A. El-Shaer, A. Che Mofor, B. Postels, A.

Waag, N. Boukos, A. Travlos, H. S. Kwack, J. Guinard, and D. Le Si Dang, Nanotechnology **20**, 332001 (2009).

[195] C. Klingshirn, Phys. Status Solidi B **244**, 3027 (2007).

[196] D. J. Gargas, M. C. Moore, A. Ni, S.-W. Chang, Z. Zhang, S.-L. Chuang, and P. Yang, ACS Nano **4**, 3270 (2010).

[197] C. Xu, J. Dai, G. Zhu, G. Zhu, Y. Lin, J. Li, and Z. Shi, Laser Photonics Rev. **8**, 469 (2014).

[198] A. B. Djurišić, Y. H. Leung, K. H. Tam, L. Ding, W. K. Ge, H. Y. Chen, and S. Gwo, Appl. Phys. Lett. **88**, 103107 (2006).

[199] R. J. Epstein, F. M. Mendoza, Y. K. Kato, and D. D. Awschalom, Nat. Phys. **1**, 94 (2005).

[200] P. R. Dolan, X. Li, J. Storteboom, and M. Gu, Opt. Express **22**, 4379 (2014).

[201] V. M. Acosta, A. Jarmola, E. Bauch, and D. Budker, Phys. Rev. B **82**, (2010).

[202] T. P. M. Alegre, C. Santori, G. Medeiros-Ribeiro, and R. G. Beausoleil, Phys. Rev. B **76**, (2007).

[203] C. Lethiec, J. Laverdant, H. Vallon, C. Javaux, B. Dubertret, J.-M. Frigerio, C. Schwob, L. Coolen, and A. Maître, Phys. Rev. X **4**, (2014).

[204] C. D. Clark, G. W. Maycraft, and E. W. J. Mitchell, J. Appl. Phys. **33**, 378 (1962).

[205] J. T. Fourkas, Opt. Lett. **26**, 211 (2001).

[206] A. A. Bergman, A. M. Zaitsev, and A. A. Gorokhovsky, J. Lumin. **125**, 92 (2007).

[207] T. Ha, T. A. Laurence, D. S. Chemla, and S. Weiss, J. Phys. Chem. B **103**, 6839 (1999).

[208] M. S. Dresselhaus, G. Dresselhaus, and A. Jorio, *Group Theory: Application to the Physics of Condensed Matter* (Springer Berlin Heidelberg, 2007).

[209] P. Jakes and E. Erdem, Phys. Status Solidi RRL - Rapid Res. Lett. **5**, 56 (2011).

[210] H. Kaftelen, K. Ocakoglu, R. Thomann, S. Tu, S. Weber, and E. Erdem, Phys. Rev. B **86**, (2012).

[211] S. W. Brown and S. C. Rand, J. Appl. Phys. **78**, 4069 (1995).

[212] F. Güttler, M. Croci, A. Renn, and U. P. Wild, Chem Phys **211**, 421 (1996).

[213] G.-H. Lee, R. C. Cooper, S. J. An, S. Lee, A. van der Zande, N. Petrone, A. G. Hammerberg, C. Lee, B. Crawford, W. Oliver, and others, Science **340**, 1073 (2013).

[214] A. Shekhawat and R. O. Ritchie, Nat. Commun. **7**, 10546 (2016).

[215] K. I. Bolotin, K. J. Sikes, Z. Jiang, M. Klima, G. Fudenberg, J. Hone, P. Kim, and H. L. Stormer, Solid State Commun. **146**, 351 (2008).

[216] J. Baringhaus, M. Ruan, F. Edler, A. Tejeda, M. Sicot, A. Taleb-Ibrahimi, A.-P. Li, Z. Jiang, E. H. Conrad, C. Berger, C. Tegenkamp, and W. A. de Heer, Nature **506**, 349 (2014).

[217] C.-C. Chen, Z. Li, L. Shi, and S. B. Cronin, Appl. Phys. Lett. **104**, 081908 (2014).

[218] N. Sakhavand and R. Shahsavari, ACS Appl. Mater. Interfaces **7**, 18312 (2015).

[219] W. Lei, D. Portehault, D. Liu, S. Qin, and Y. Chen, Nat. Commun. **4**, 1777 (2013).

[220] G. Lian, X. Zhang, H. Si, J. Wang, D. Cui, and Q. Wang, ACS Appl. Mater. Interfaces **5**, 12773 (2013).

[221] C.-J. Kim, A. Sánchez-Castillo, Z. Ziegler, Y. Ogawa, C. Noguez, and J. Park, Nat. Nanotechnol. (2016).

[222] A. Kumar, A. Nemilentsau, K. H. Fung, G. Hanson, N. X. Fang, and T. Low, Phys. Rev. B **93**, (2016).

[223] A. K. Geim and I. V. Grigorieva, Nature **499**, 419 (2013).

[224] X. Wang and F. Xia, Nat. Mater. **14**, 264 (2015).

[225] X. Cui, G.-H. Lee, Y. D. Kim, G. Arefe, P. Y. Huang, C.-H. Lee, D. A. Chenet, X. Zhang, L. Wang, F. Ye, F. Pizzocchero, B. S. Jessen, K. Watanabe, T. Taniguchi, D. A. Muller, T. Low, P. Kim, and J. Hone, Nat. Nanotechnol. **10**, 534 (2015).

[226] Y. Chu and M. D. Lukin, ArXiv Prepr. ArXiv150405990 (2015).

[227] T. T. Tran, C. Zachreson, A. M. Berhane, K. Bray, R. G. Sandstrom, L. H. Li, T. Taniguchi, K. Watanabe, I. Aharonovich, and M. Toth, Phys. Rev. Appl. **5**, (2016).

[228] K.-M. C. Fu, C. Santori, P. E. Barclay, L. J. Rogers, N. B. Manson, and R. G. Beausoleil, Phys. Rev. Lett. **103**, 256404 (2009).

[229] H.-Q. Zhao, M. Fujiwara, M. Okano, and S. Takeuchi, Opt. Express **21**, 29679 (2013).

[230] E. Neu, C. Hepp, M. Hauschild, S. Gsell, M. Fischer, H. Sternschulte, D. Steinmüller-Nethl, M. Schreck, and C. Becher, New J. Phys. **15**, 043005 (2013).

[231] W. B. Gao, A. Imamoglu, H. Bernien, and R. Hanson, Nat. Photonics **9**, 363 (2015).

[232] B. Hensen, H. Bernien, A. E. Dréau, A. Reiserer, N. Kalb, M. S. Blok, J. Ruitenberg, R. F. L. Vermeulen, R. N. Schouten, C. Abellán, W. Amaya, V. Pruneri, M. W. Mitchell, M. Markham, D. J. Twitchen, D. Elkouss, S. Wehner, T. H. Taminiau, and R. Hanson, Nature **526**, 682 (2015).

[233] B. Lienhard, T. Schröder, S. Mouradian, F. Dolde, T. T. Tran, I. Aharonovich, and D. R. Englund, ArXiv Prepr. ArXiv160305759 (2016).

[234] K. Huang and A. Rhys, P Roy Soc Math Phys **204**, 406 (1950).

[235] A. Alkauskas, B. B. Buckley, D. D. Awschalom, and C. G. Van de Walle, New J. Phys. **16**, 073026 (2014).

[236] T. Tohei, A. Kuwabara, F. Oba, and I. Tanaka, Phys. Rev. B **73**, 064304 (2006).

[237] C. Attaccalite, M. Bockstedte, A. Marini, A. Rubio, and L. Wirtz, Phys. Rev. B **83**, (2011).

[238] A. Sipahigil, M. L. Goldman, E. Togan, Y. Chu, M. Markham, D. J. Twitchen, A. S. Zibrov, A. Kubanek, and M. D. Lukin, Phys. Rev. Lett. **108**, 143601 (2012).

[239] J. T. Ritter and J. J. Markman, Phys. Rev. **185**, 1201 (1969).

[240] M. de Jong, L. Seijo, A. Meijerink, and F. T. Rabouw, Phys Chem Chem Phys **17**, 16959 (2015).